ALMA MATER STUDIORUM - UNIVERSITÀ DI BOLOGNA

DIPARTIMENTO DI ELETTRONICA INFORMATICA E SISTEMISTICA

DOTTORATO DI RICERCA IN INGEGNERIA ELETTRONICA, INFORMATICA E

DELLE TELECOMUNICAZIONI – XIX CICLO

SSD: ING-INF/02 – Campi Elettromagnetici

MULTIDIMENSIONAL CHARACTERIZATION OF

THE MIMO RADIO CHANNEL

(Caratterizzazione Multidimensionale del Canale Radio MIMO)

Tesi di: Relatore:

ING. ENRICO MARIA VITUCCI   CHIAR.MO PROF. ING. GABRIELE FALCIASECCA

Coordinatore:

CHIAR.MO PROF. ING. PAOLO BASSI

Triennio Accademico 2004 – 2005 – 2006

Keywords

Channel

MIMO

Propagation

Scattering

Ray-Tracing

Contents

Introduction

Recently, with the advent of high-speed, multimedia communication systems and services, advanced radio transmission and antenna techniques have been proposed such as diversity, adaptive antenna and Multiple Input - Multiple Output (MIMO) techniques [2,3], which explicitly exploit the multipath nature of the radio link. In order to properly design, plan and optimize systems adopting such techniques, coverage prediction models will no longer be sufficient. A multidimensional characterization of radio propagation is necessary, including time delay, angle of arrival, angle of departure profiles and time variance of the radio channel. Therefore, multidimensional analysis and modelling of multipath propagation must be considered of strategic importance for the design and the implementation of future mobile radio and broadcasting systems, especially in urban environment where multipath propagation naturally takes place.

In particular, a reliable characterization of the spatial and temporal dispersion properties of the radio channel is of crucial importance in order to correctly predict the performance of MIMO systems. MIMO techniques, i.e. radio transmission techniques based on the adoption of multiple antennas (arrays) at both terminals of the radio link, have been proposed and widely studied in recent years from the information theory and signal processing point of view [2-13].

MIMO should in theory allow great advantages with respect to conventional transmission techniques in terms of both diversity gain and multiplexing gain, and therefore capacity gain [2, 4-6, 16]. The capacity gain increases with the number of antennas (inputs and outputs), but also with the so called "multipath richness" which is in short the property of the multipath of being composed of many contributions with similar amplitude and large spreading in both angle of arrival/departure and time delay. Multipath richness can be measured through the Effective Degrees of Freedom (EDOF) of the radio channel, which actually sets an upper bound to system performance, and is inversely dependent on the spatial correlation properties of the multipath channel [7,15].

Since MIMO implementation is expensive in terms of complexity and antenna size, its cost-effectiveness strongly depends on the obtainable capacity gain and therefore on the degree of multipath richness which can be found in practice in typical urban environments. Therefore, both manufacturers and operators are at present very interested in MIMO performance estimates in real environment and consequently in a realistic characterization of multipath propagation in urban environment.

Multipath propagation in urban areas is a complex phenomenon involving several mechanisms of interaction between the radio wave and the environment.

A complete, multidimensional propagation characterization, which takes into account both time- and angle- dispersion, can of course be achieved through experimental channel sounding techniques [23, 24]. However, expensive setups with sophisticated spherical array antennas are required for this purpose, and the measurement campaigns are generally very time consuming, especially if a characterization in different environment classes with a sufficient statistical base is needed.

Multipath propagation prediction through computer programs, if reliable, is therefore very welcome. In theory, Ray Tracing (RT) or in general, ray models represents the most appropriate MIMO channel prediction models since they are the only models to strictly simulate multipath and its multidimensional (space, time, and frequency) de-correlation effects on the radio channel. Such models can also provide statistical channel information by applying Monte Carlo analysis on many random transmit/receive locations and/or model geometries [64].

Unfortunately, limitations in computation speed and in the capability of fully reproducing the actual degree of multipath richness and the actual multipath characteristics in a given environment, which are influenced by such complex phenomena as "diffuse scattering" [36, 45], still limit their effectiveness.

In fact, some comparisons of predictions provided by traditional RT simulators with measurement indicate that the simulations tend to underestimate MIMO channel capacity [65], likely due more to oversimplification of the geometrical scenario representation than failure of the electromagnetic simulation approach. Indeed, most of the commercial ray tracing simulators based on Geometrical Optics (GO) approach assume that building walls and edges are homogeneous and smooth: this hypothesis is not valid in real cases. Surface and volume irregularities, the presence of objects such as windows,

balconies, lampposts, advertising signs, internal beams and cables, etc. contribute to the scattering of the impinging radio power in unpredictable ways, also because the cited objects and their exact position and characteristics are generally a priori unknown, and so they are not included in databases.

Diffuse scattering of the radio wave is especially important when far and tall buildings (high-rise buildings, towers, buildings located on hills etc.) are present [39, 51]. Since far buildings are "viewed" from the transmitter under a narrow solid angle, they produce a very narrow reflection cone; diffraction is also significant only in the vicinity of the border of this reflection cone and around the ISB (Incident Shadow Boundary) [85]. On the contrary, scattering can be present in a much wider solid angle and therefore potentially produces a much greater number of paths [45-50].

Recent studies highlighted that scattered rays, while relatively weak in power, have a strong impact on time and angle dispersion of the radio link [23, 24, 36-39]. Therefore, the multidimensional behaviour of the urban radio channel cannot be fully understood without taking what we call "diffuse scattering" into account.

In summary, while radio coverage can be easily analyzed and predicted with acceptable accuracy with simple empirical formulas, such as Hata-like formulas, multidimensional characterization of the MIMO radio channel requires models that take into account the multipath nature of the radio link, and possibly include reflection, diffraction and diffuse scattering phenomena.

Diffuse scattering has been modeled adopting the *Effective Roughness (ER) approach* described in [36, 37], and the scattering model has been embedded into the advanced three-dimensional vectorial RT tool described in [38]. In the present work, the ER model has been modified by orienting the scattering pattern lobe toward the specular direction, which is more realistic, and re-shaping it in a number of different ways while preserving the physical consistency of the model; the proposed model has been validated through a measurement campaign, and it is shown that by adopting an appropriate scattering pattern the agreement between simulation and measurement is very good [41-42].

Moreover, it is shown that diffuse scattering plays a fundamental role in the achievement of the MIMO capacity gain, and therefore modelling of diffuse scattering allows to get a good MIMO capacity prediction [63], whereas traditional RT methods tends to underestimate it.

On the other hand, a major problem which limits the widespread adoption of deterministic ray models is the high complexity and high computation time of the

corresponding computer programs. The high computation time is strongly dependent on the size of the input database and on the inherent inefficiency of the geometric ray-finding phase of the RT algorithm. Some Authors have worked on speed-up methods for RT models. Among other methods, the decomposition of 3D propagation into 2D planes is proposed in [56], while the discretization of the environment and its geometric pre-processing are proposed in [96]. In the present, two different methods for speeding up RT prediction are proposed. The first one operates on reducing the size of the input database by selecting the "active area" of the environment and discarding the rest of the map. The second one operates on reducing the number of rays to be handled by the RT algorithm, by handling "far objects" in a simplified way and by discarding low-power rays.

The methods are applied on the 3D RT model described in [38], and it is shown that by using this model, and without the need of time-consuming and arbitrary database manipulation, the CPU time is drastically reduced almost without degradation of multidimensional prediction results [59-61].

In chapter 1 an overview of the MIMO channel and of the main space-time processing techniques is given.

In chapter 2 the modified diffuse scattering models based on the ER approach are described. The proposed models, embedded in the advanced RT tool described in [38], are validated through comparisons between measurements and simulations.

In chapter 3, two advanced techniques of database simplification and speed-up for Ray Tracing models are proposed, in order to reduce the computational burden of these methods while preserving the reliability of the narrowband and wideband predictions.

In chapter 4, the capability of Ray Tracing to correctly reproduce the temporal and spatial dispersion properties of the radio channel (delay spread, angle spread, power-delay and power-azimuth profiles) is shown: in particular, an extensive, multidimensional analysis of multipath propagation in urban micro- and macro-cellular environment is carried out. Narrowband and wideband parameters, measured with a sophisticated spherical array antenna receiver and simulated with the RT tool are analyzed and compared.

Finally, in chapter 5 the fundamental role of the diffuse scattering in the prediction of the MIMO capacity gain is shown, through comparisons between ray tracing predictions and measurements.

Chapter 1

The MIMO Wireless Channel

1.1 Wireless Channel Models

A typical communication system consists of a transmitter, a receiver and a channel. The *channel* is defined as the physical medium linking the transmitter output and the receiver input. For instance, telephone wire, optical fiber, and the atmosphere are different examples of communication channels. In fact, communication channel plays a very important role in communication system design because the transmitter an receiver have to be optimized with respect to the target channel. In the text below, we briefly review the deterministic and statistical models of wireless communication channels for single-antenna and multiple-antenna systems.

1.1.1 AWGN Channel Model

We consider the simplest wireless channel, the *Additive White Gaussian Noise* (AWGN) channel. Without loss of generality, we consider single-antenna systems as illustrative in this section. The received signal $y(t)$ is given by the transmitted signal $x(t)$ plus a white Gaussian noise $n(t)$:

$$y(t) = h \cdot x(t) + n(t) \tag{1.1}$$

where h is the free-space power attenuation from the transmitter to the receiver.

The AWGN channel is in fact quite accurate in deep-space communications and the communication links between satellite and Earth stations. However, it is far from accurate in most terrestrial wireless communications, due to multipath

propagation. Yet, AWGN, channel serves as an important reference on the performance evaluation of communication systems.

In terrestrial wireless communications, signals travel to the receiver via multiple paths, and this creates additional distortion to the transmitted signal on top of the channel noise. In general, the effect of multipath and reflections could be modelled as wireless fading channels or *microscopic fading*. Factors affecting the microscopic fading include multipath propagation, speed of the mobile, speed of the surrounding objects, the transmission symbol duration, and the transmission bandwidth of the signal.

1.1.2 Linear Time-Varying Deterministic Spatial Channel

Consider a general linear channel that can be characterized by a *lowpass equivalent* time-domain impulse response denoted by $h(t, \tau, r)$ (where t is the time-varying parameter, τ is the path delay parameter, and r is the spatial position parameter). The general linear channel is therefore characterized by three independent dimensions: the *time dimension* (characterized by the parameter t), the *delay dimension* (characterized by the delay parameter τ), and the *spatial dimension* (characterized by the position parameter r). Given a lowpass equivalent input signal *x(t)*, the lowpass equivalent received signal *y(t,r)* through the general linear deterministic channel at time t and position r is given by

$$y(t,r) = h(t,\tau,r) * x(t) + n(t,r) = \int_{-\infty}^{+\infty} h(t,\tau,r) x(t-\tau) d\tau + n(t,r) \quad (1.2)$$

where the input dignal (in time domain) is mapped into output signal (in time domain and spatial domain) through the impulse response $h(t, \tau, r)$. For simplicity, we shall discuss the channel characterization based on single-antenna systems. Extension to the MIMO systems will be straightforward. For example, to extend the model to MIMO systems, the transmitted signal *x(t)* is replaced by the N_Tx1 vector **x**(t):

$$\mathbf{x}(t) = \begin{bmatrix} x_1(t) \\ \vdots \\ x_{NT}(t) \end{bmatrix}$$

The received signal *y(t,r)* and the noise signal *n(t,r)* are replaced by the N_Rx1 vectors **y**(t) and **n**(t,r), respectively:

$$\mathbf{y}(t,\mathbf{r}) = \begin{bmatrix} y_1(t,r_1) \\ \vdots \\ y_{N_R}(t,r_{N_R}) \end{bmatrix}$$

$$\mathbf{n}(t,\mathbf{r}) = \begin{bmatrix} n_1(t,r_1) \\ \vdots \\ n_{N_R}(t,r_{N_R}) \end{bmatrix}$$

The time-varying channel impulse response is replaced by the N_RxN_T *channel matrix* $\mathbf{H}(t,\tau,r)$, given by:

$$\mathbf{H}(t,\tau,\mathbf{r}) = \begin{bmatrix} h_{11}(t,\tau,r_{11}) & \cdots & h_{1N_T}(t,\tau,r_{1N_T}) \\ \vdots & \ddots & \vdots \\ h_{N_R1}(t,\tau,r_{N_R1}) & \cdots & h_{N_RN_T}(t,\tau,r_{N_RN_T}) \end{bmatrix}$$

where h_{ij} is the channel response corresponding to the j-th transmit antenna and the i-th receive antenna, and r is the corresponding position parameter.

1.1.2.1 *Spectral Domain Representations*

While equation (1.2) gives the fundamental input-output relationship of the linear deterministic channels Fourier transforms are sometimes useful for gaining additional insights in channel analysis. Since the channel impulse responses $h(t,\tau,r)$ are defined over the time, delay and position domains, Fourier transforms may be defined for each of these domains, and they are elaborated as follows:

- *Frequency Domain.* The spectral domain of the delay parameter t is called the *frequency domain f*. They are related by the Fourier transform relationship $h(t,\tau,r) \leftrightarrow H(t,f,r)$. For example, $H(t,f,r)$ is given by

$$H(t,f,r) = \int_{-\infty}^{+\infty} h(t,\tau,r)e^{-j2\pi\tau f}d\tau$$

Since $x(t-\tau) = \int_{-\infty}^{+\infty} X(f)e^{j2\pi f(t-\tau)}df$, substituting into Equation (1.2) we have:

$$y(t,r) = \int_{-\infty}^{+\infty} h(t,\tau,r) \int_{-\infty}^{+\infty} X(f) e^{j2\pi f(t-\tau)} df \, d\tau =$$

$$= \int_{-\infty}^{+\infty} X(f) e^{j2\pi f t} \left(\int_{-\infty}^{+\infty} h(t,\tau,r) e^{-j2\pi f\tau} d\tau \right) df =$$

$$= \int_{-\infty}^{+\infty} H(t,f,r) X(f) e^{j2\pi f t} df$$

(1.4)

Hence, the channel response can also be specified by the *time-varying transfer function H(t,f,r)*. In addition, it can be found from Equation (1.4) that the output signal (in time domain) $y(t,r)$ is mapped from the input signal (in frequency domain) X(f) through the time-varying transfer function H(t,f,r).

- *Doppler Domain.* The spectral domain of the time parameter t is called the *Doppler domain v*. They are related by the Fourier transform relationship $h(t,\tau,r) \leftrightarrow H(v,\tau,r)$. For example, $H(v,\tau, r)$ is given by

$$H(v,\tau,r) = \int_{-\infty}^{+\infty} h(t,\tau,r) e^{-j2\pi t v} dt$$

(1.5)

Similarly, the input signal (in delay domain) $x(\tau)$ can be mapped into the output signal (in Doppler domain) $Y(v,r)$ through the transfer function $H(v,\tau, r)$:

$$Y(v,r) = \int_{-\infty}^{+\infty} H(v,\tau,r) x(t-\tau) d\tau$$

(1.6)

- *Wavenumber Domain.* The spectral domain of the position parameter r is called the *wavenumber domain k*. The wavenumber in three-dimensional space has a physical interpretation of the plane-wave propagation direction. The position and wavenumber domains are related by the Fourier transform relationship $h(t,\tau,r) \leftrightarrow H(t,\tau,k)$. For example, $H(t,\tau,k)$ is given by

$$H(t,\tau,k) = \int_{-\infty}^{+\infty} h(t,\tau,r) e^{-j2\pi r k} dr$$

(1.7)

In general, two important concepts are applied to describe these linear deterministic channels: spreading and coherence. The *spreading* concept deals with the physical spreading of the received signal over the parameter space

4

(v, τ, k) when a narrow pulse is transmitted in the corresponding domain. The *coherence* concept deals with the variation of the channel response with respect to another parameter space (t, f, r). These concept are elaborated in the text below.

1.1.2.2 *Channel Spreading.*

The channel spreading concepts of describing the general linear deterministic channels focus on the spreading of the received signals over the parameter space (v, τ, k) when a narrow pulse in the corresponding parameter is transmitted. We therefore have three types of channel spreading:

- *Delay Spread.* If we transmit a test pulse that is narrow in time, the received signal will have a spread in propagation delay τ due to the sum of different propagation delays of multipaths at the receiver. From Equation (1.2), when the transmit signal is narrow in time, we have $x(\tau) = \delta(\tau)$. Hence, the received signal is given by $y(t, r) = h(t, \tau = t, r)$. The plot of $\left| h(t, t, r) \right|^2$ versus time is called the *power-delay profile* as illustrated in Figure 1.1a. The range of delays where we find significant power is called the *delay spread* σ_τ.

- *Doppler Spread.* If we transmit a test pulse narrow in frequency $X(f) = \delta(f)$, the received signal in general will experience a spread in the received spectrum. The range of spectrum spread in the frequency domain of the received signal $Y(v, r)$ refers to Doppler spread. The Doppler spread is given by $f_d = \dfrac{v}{\lambda}$, where v is the maximum speed between the transmitter and the receiver and λ is the wavelength of the carrier. This is illustrated in Figure 1.2a.

- *Angle Spread.* Finally, the scattering environment introduces variation in the spatial parameter r, which is equivalent to the spreading in the wavenumber domain k, this is called the (unidimensional) *angle spread.* For example, if a test pulse narrow in direction is transmitted, the received signal will experience a spread in the wavenumber domain (angle of arrivals) due to the scattering surroundings; this is called the *angle spread* as illustrated in Figure 1.3a.
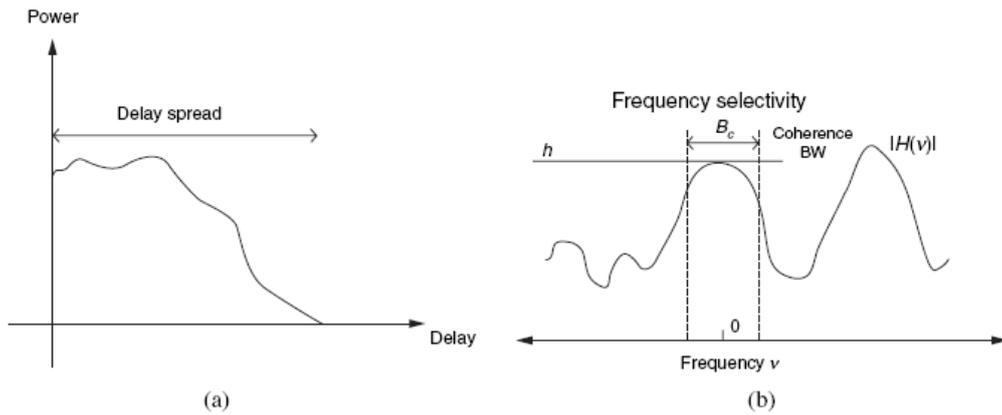
Figure 1.1 – Delay spread (a) and coherence bandwidth (b)
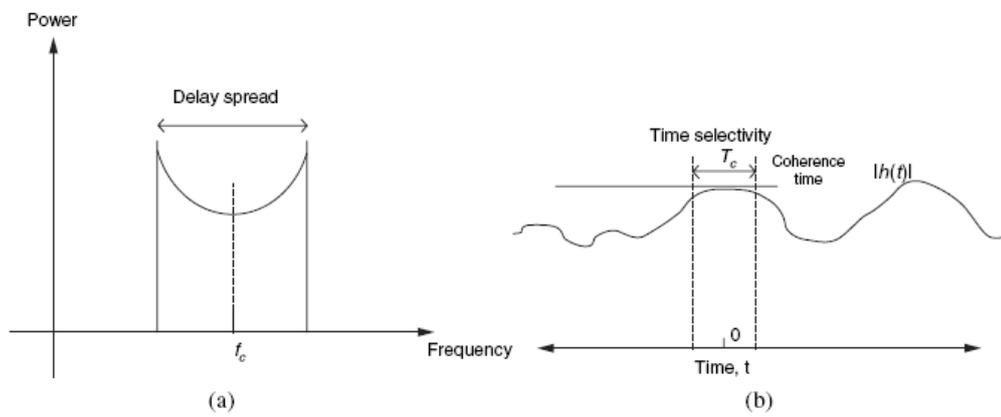
Figure 1.2 – Doppler spread (a) and coherence time (b)
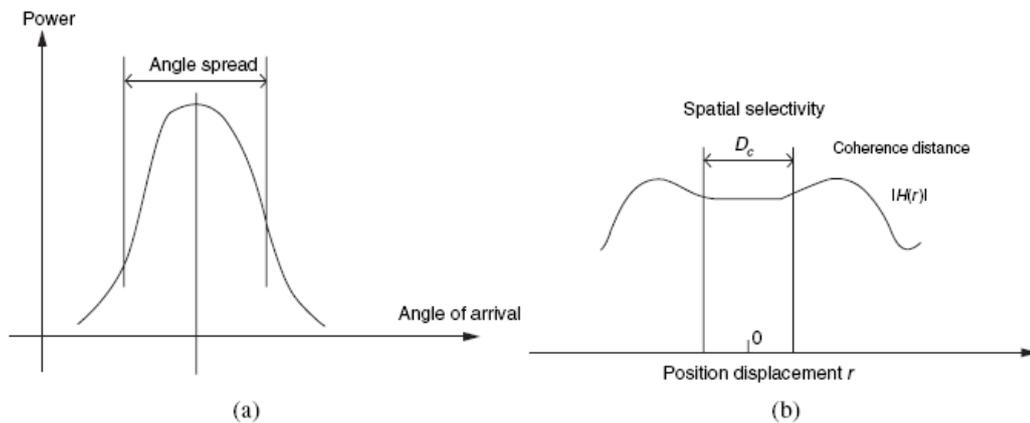
Figure 1.3 – Illustration of angle spread (a) and coherence distance (b)

1.1.2.3 *Channel Coherence.*

On the other hand, we can describe the linear deterministic channels by looking at the channel coherence or channel selectivity properties over the parameter

space (t,f,r). A channel is said to be selective in the corresponding dimension if the channel response varies as a function of that parameter. The opposite of selectivity is *coherence*. A channel has coherence in the corresponding dimension if it does not change significantly as a function of that parameter. The channel coherence properties with respect to the frequency, time and position dimensions are elaborated below.

- *Frequency Coherence or Frequency Selectivity.* A wireless channel has frequency coherence if the magnitude of the carrier wave does not change over a frequency window of interest. This window of interest is usually the bandwidth of the transmitted signal. Hence, mathematically, we can quantify the frequency coherence of the channels by a parameter called the *coherence bandwidth B_C*

$$\left|H(t,f,r)\right| \approx H_0(t,r) \quad \text{for} \quad |f| \leq \frac{B_C}{2} \tag{1.8}$$

  where $H_0(t,r)$ is a constant in the frequency domain f and B_C is the size of the frequency window where we have constant channel response. The largest value of B_C for which Equation (1.8) holds is called the *coherence bandwidth* and can be interpreted as the range of frequencies over which the channel appears static. Figure 1.1b illustrates the concept of coherence bandwidth. In fact, if the bandwidth of the transmitted signal is larger than the coherence bandwidth of the channel, the signal will experience frequency distortion according to Equation (1.4). Such a channel is classified as a *frequency-selective fading channel*. On the other hand, if the transmitted signal has bandwidth smaller than the coherence bandwidth of the channel, frequency distortion will be no introduced to the signal and therefore, the channel will be classified as a *frequency-flat fading channel*. Frequency selectivity introduces *intersymbol interference*, and this results in irreducible error floor in the BER (Bit Error Rate) curve. Hence, this is highly undesirable. Whether a signal will experience frequency-selective fading or flat fading depends on both the environment (coherence bandwidth) and the transmitted signal (transmitted bandwidth).

- *Time Coherence or Time Selectivity.* A wireless channel has temporal coherence if the envelope of the unmodulated carrier does not change over a time window of interest. The time coherence of channels can be specified by a parameter called the *coherence time T_C*

7

$$|H(t,f,r)| \approx H_0(f,r) \quad \text{for} \quad |t| \leq \frac{T_C}{2} \tag{1.9}$$

where $|H(t,f,r)|$ is the envelope of the response at the receiver (at a fixed position r) when a single-tone signal (at a fixed frequency f) is transmitted, $H_0(f,r)$ is a constant in the time domain t and T_C is the size of the time window where we have constant channel response. The largest value of T_C for which Equation (1.9) holds is called the *coherence time* and can be interpreted as the range of time over which the channel appears static as illustrated in Figure 1.2b. In wireless fading channels, temporal incoherence (or time selectivity) is caused by the motion of the transmitter, the receiver or the scattering objects in the environment. Time selectivity can degrade the performance of wireless communication systems. If the transmit data rate is comparable to the coherence time, it becomes extremely difficult for the receiver to demodulate the transmitted signal reliably because the time selectivity within a symbol duration causes catastrophic distortion on the received pulse shape. Hence, when the transmit duration T_S is longer than the coherence time T_C, we have *fast fading channels*. In the extreme case of slow fading the channel remains static for the entire transmit frame.

- *Spatial Coherence or Spatial Selectivity.* A wireless channel has spatial coherence if the magnitude of the carrier wave does not change over a spatial displacement of the receiver. Mathematically, the spatial coherence can be parameterized by the *coherence distance* D_C

$$|H(t,f,r)| \approx H_0(t,f) \quad \text{for} \quad |r| \leq \frac{D_C}{2} \tag{1.10}$$

where $|H(t,f,r)|$ is the envelope of the response at the receiver when a single-tone signal (at a fixed frequency f) is transmitted (at a fixed time t), $H_0(t,f)$ is a constant with respect to the spatial domain r, and D_C is the size of the spatial displacement where we have constant channel response. The largest value of D_C for which Equation (1.10) holds is called the *coherence distance* and can be interpreted as the range of displacement over which the channel appears static as illustrated in Figure 1.3b. Note that for a wireless receiver moving in three-dimensional space, the coherence distance is a function of the direction that the receiver travels; that is, the position displacement **r** is a vector instead of a scalar. Hence,

the study of spatial coherence is much more difficult than the study of the scalar quantities of temporal or frequency coherence. While frequency selectivity is a result of multipath propagation arriving with many different time delays τ, spatial selectivity is caused by the multipath propagation arriving from different directions in space. These multipath waves are superimposed on each other, creating pockets of constructive and destructive interference in the three-dimensional spatial domain so that the received signal power does not appear to be constant over small displacement of receiver position. Hence, if the distance traversed by a receiver is greater than the coherence distance, the channel is said to be *spatially selective* or *small-scale fading*. On the other hand, if the distance traversed by a receiver is smaller than the coherence distance, the channel is said to be *spatially flat*. Spatially selective or spatial flat fading is important when we have to apply spatial diversity (or spatial multiplexing) and beamforming. For instance, in order to produce a beam of energy along the designated direction through antenna array, the dimension of the antenna array must be within the coherence distance of the channels. On the other hand, to effectively exploit the spatial multiplexing or spatial diversity of MIMO systems, the spacing of the antenna array must be larger than coherence distance of the channels.

Figures 1.4 and 1.5 summarize the various behaviours of microscopic fading channels.
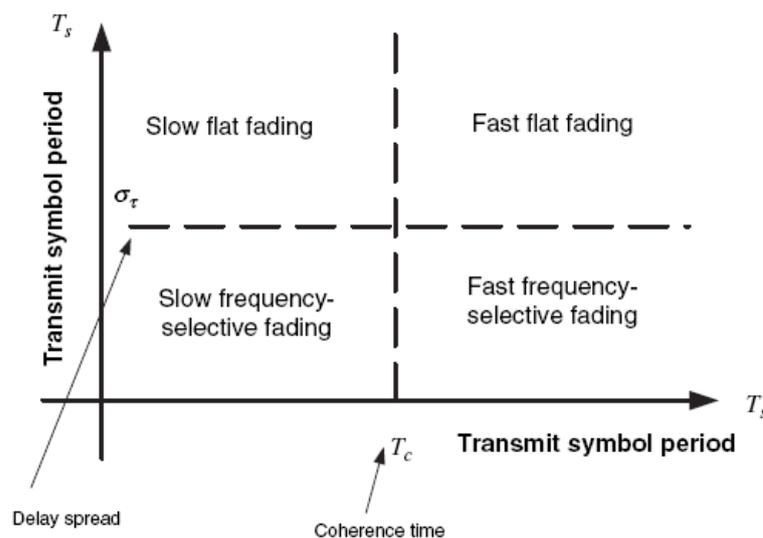
Figure 1.4 – Summary of fading channels (time domain)
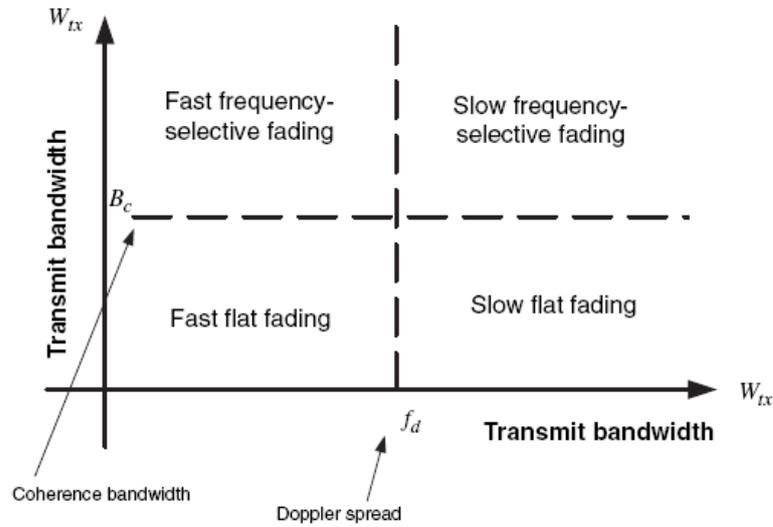
Figure 1.5 – Summary of fading channels (frequency domain)

1.1.3 The Random Channels

In section 1.2.2, we have introduced the general linear deterministic channel where the relationship of output given an input signal is modelled as a general time-varying system. However, in practice, the wireless fading channels we experience are random instead of deterministic; that is, $h(t, \tau, r)$ is a random process instead of a deterministic quantity. Hence, in this section, we shall extend the model of linear deterministic channels to cover the random channels.

The behaviour of $h(t, \tau, r)$ in general is very complicated. However, practical situations lend themselves to certain simplifying assumptions such as stationarity which we shall describe next. In the following, we assume the *expectation* operator, ε, to be in the ensemble sense. Great care is normally needed in treating the existence and convergence of such statistics, but it is beyond the scope of this brief overview.

1.1.3.1 *Wide sense stationariety (WSS)*
WSS implies that the second-order time statistics of the channel are stationary. This assumption is justified in mobile channels over short periods, T_u. We drop the space dimension (r) dependence temporarily for clarity. WSS implies that

$$R_h\left(\tau,t_1,t_2\right)=\varepsilon\left\{h\left(\tau,t_1\right)h^*\left(\tau,t_2\right)\right\}=R_h\left(\tau,\Delta t\right)\ (1.11)$$

i.e., the random process $h(t,\tau)$ is called *wide-sense stationary* (WSS) if the autocorrelation in time depends only on the lag $\Delta t=|t_2\text{-}t_1|$ and not on t_1 and t_2. $R_h\left(\tau,\Delta t\right)$ is called the *lagged-time correlation function.*

On the other hand, we can also consider the correlation in the spectral domain of t. Specifically, after Fourier transform on $h(t,\tau)$ with respect to t, we have a random frequency-varying process $H(\nu,\tau)$. The autocorrelation of the random process $H(\nu,\tau)$ is given by

$$R_H\left(\tau,\nu_1,\nu_2\right)=\varepsilon\left[H\left(\tau,\nu_1\right)H^*\left(\tau,\nu_2\right)\right]\ (1.12)$$

As $T_u\to\infty$, we get

$$\varepsilon\left[H\left(\tau,\nu_1\right)H^*\left(\tau,\nu_2\right)\right]=0\quad\text{if}\quad\nu_1\neq\nu_2\quad(1.13)$$

which implies that *a channel is wide-sense stationary if and only if its spectral components (Doppler frequencies) are uncorrelated* [1].

1.1.3.2 *Uncorrelated scattering (US)*

The US model assumes that the scatterers contributing to the delay spread in the channel have independent fading, i.e.,

$$R_h\left(t,\tau_1,\tau_2\right)=\varepsilon\left[h\left(t,\tau_1\right)h^*\left(t,\tau_2\right)\right]=0\quad\text{if}\quad\tau_1\neq\tau_2\ (1.14)$$

The US assumption implies stationarity in the in the transmission frequency domain, which is the frequency in the passband of the channel. Let consider the Fourier transform on $h(t,\tau)$ with respect to τ ; we obtain a random frequency-varying process $H(t,f)$ which describes the channel in the transmission frequency (f)-time(t) domain. From the US assumption we have

$$R_H\left(t,f_1,f_2\right)=\varepsilon\left\{H\left(t,f_1\right)H^*\left(t,f_2\right)\right\}=R_H\left(t,\Delta f\right)\ (1.15)$$

i.e., the *uncorrelated scattering* (US) assumption is satisfied if the autocorrelation in frequency depends only on the lag $\Delta f=|f_2\text{-}f_1|$ and not on f_1 and f_2. $R_H\left(t,\Delta f\right)$ is called the *lagged-transmission frequency correlation function.* The combination of the WSS and US assumptions leads to what is called the *wide sense stationary uncorrelated scattering* (WSSUS) *channel*, which is stationary in time and transmission frequency domains and conversely has independent components in the Doppler frequency (ν) and delay (τ) dimensions.

1.1.3.3 *Homogeneous channels (HO)*

We now reintroduce the space dimension *r*. A reasonable assumption in practice for spatial models is that the statistical behaviour of *h(t, τ,r)* is locally stationary in space over several tens of the coherence distance D_C. This implies

$$R_h\left(t,\tau,r_1,r_2\right) = \varepsilon\left\{h\left(t,\tau,r_1\right)h^*\left(t,\tau,r_2\right)\right\} = R_h\left(t,\tau,\Delta r\right) \quad (1.16)$$

i.e., the autocorrelation of the channel response across space depends only on $\Delta r = |r_2 - r_1|$ and not on r_1 and r_2. $R_h\left(t,\tau,\Delta r\right)$ is called the *lagged-space correlation function*.

Let consider the Fourier transform on *h(t, τ,r)* with respect to *r* ; we obtain a random process *H(t, τ,k)* which describes the channel in the time (*t*) - delay(*τ*) – wavenumber (k) domain. From the HO assumption we have

$$R_H\left(t,\tau,k_1,k_2\right) = \varepsilon\left[H\left(t,\tau,k_1\right)H^*\left(t,\tau,k_2\right)\right] = 0 \quad \text{if} \quad k_1 \neq k_2 \quad (1.17)$$

This implies that *a channel is homogeneous if and only if the spectral components of the position parameter r are uncorrelated*. The combination of the WSSUS channel with the HO assumption is termed the WSSUS-HO channel.

1.1.3.4 *Joint Correlation and Spectrum*

Now, let's consider the general random channel response *H(t,f,r)* w.r.t. the time *t*, frequency *f*, and position *r*. To accommodate all the random dependencies of such a channel, it is possible to define a *joint correlation* of *H(t,f,r)* with respect to *(t,f,r)*. The joint correlation of the channel response is given by

$$R_H\left(t_1,f_1,r_1;t_2,f_2,r_2\right) = \varepsilon\left[H\left(t_1,f_1,r_1\right)H^*\left(t_2,f_2,r_2\right)\right] \quad (1.18)$$

For simplicity, we assume the random channel is a *wide-sense stationary, uncorrelated scattering homogenous* (WSSUS-HO) random process. Hence, the joint correlation $R_H\left(t_1,f_1,r_1;t_2,f_2,r_2\right)$ is a function of (Δt, Δf, Δr) only, where $\Delta t = |t_2 - t_1|$, $\Delta f = |f_2 - f_1|$ and $\Delta r = |r_2 - r_1|$. On the spectral domain *(v, τ,k)* we have:

$$S_H\left(v_1,\tau_1,k_1;v_2,\tau_2,k_2\right) = \varepsilon\left[H\left(v_1,\tau_1,k_1\right)H^*\left(v_2,\tau_2,k_2\right)\right] =$$
$$= S_H\left(v_1,\tau_1,k_1\right)\delta\left(v_1 - v_2\right)\delta\left(\tau_1 - \tau_2\right)\delta\left(k_1 - k_2\right) \quad (1.19)$$

where $S_H\left(v_1,\tau_1,k_1\right)$ is the *power spectral density* of the random process *H(t,f,r)*. The Wiener-Khintchine theorem leads to the following Fourier transform

relationship between the autocorrelation function $R_H(\Delta t,\ \Delta f,\ \Delta r)$ and the power spectral density $S_H(\nu, \tau, k)$:

$$R_H(\Delta t, \Delta f, \Delta r) \leftrightarrow S_H(\nu, \tau, k)$$

1.1.3.5 *Time-Frequency Transform Mapping*

Since the joint correlation function $R_H(\Delta t, \Delta f, \Delta r)$ is a function of three independent parameters, it is easier to fix one dimension and focus on the interrelationship between the other two dimensions. For instance, consider single-antenna systems with the receiver at a fixed position *r*. Thus, this random channel has no dependence on *r*. Hence, the statistical properties of the random channel can be specified by either the *time-frequency autocorrelation* $R_H(\Delta t, \Delta f)$ or the *delay-Doppler spectrum* $S_H(\nu, \tau)$ as illustrated in Figure 1.6. In a WSSUS channel, knowledge of only one is sufficient as they are two-dimensional Fourier transform pairs.

In Section 1.2.2 we have introduced the concepts of *coherence time* and *coherence bandwidth* or, equivalently, *Doppler spread* and *Delay spread* for deterministic channels. We will try to extend the definition of these parameters for WSSUS random channels. From the time-frequency autocorrelation function, the correlation in time dimension is given by

$$R_H(\Delta t) = R_H(\Delta t, \Delta f)\big|_{\Delta f = 0} \quad (1.20)$$

The coherence time T_C for the random channel is defined to be the value of Δt such that $R_H(\Delta t) < 0.5$.
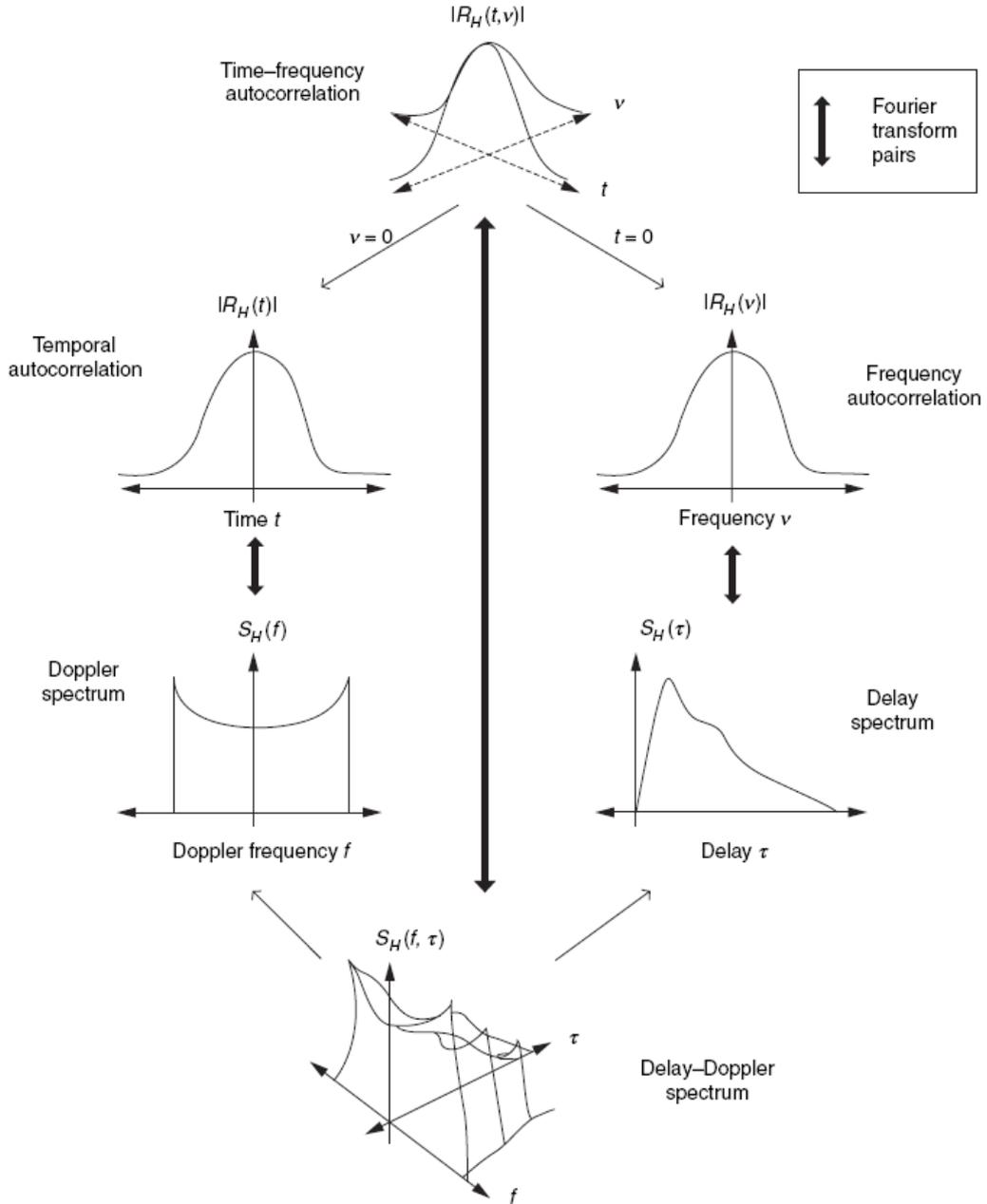
Figure 1.6 – Time-frequency autocorrelation and delay-Doppler spectrum

Similarly, the correlation in the frequency dimension is given by

$$R_H(\Delta f) = R_H(\Delta t, \Delta f)\big|_{\Delta t=0} \quad (1.21)$$

The coherence time B_C for the random channel is defined to be the value of Δf such that $R_H(\Delta f) < 0.5$.

On the other hand, we can characterize the random channel on the basis of the *delay-Doppler spectrum*. For instance, the *Doppler spectrum,* or *power-Doppler profile*, is given by

$$S_H(\nu) = \int_{-\infty}^{+\infty} S_H(\nu,\tau)\, d\tau \quad (1.22)$$

The *Doppler spread* σ_ν is defined as the square root of the second centred moment of the Doppler spectrum:

$$\sigma_\nu = \sqrt{\frac{\int_{-\infty}^{\infty} \nu^2 S_H(\nu)d\nu}{\int_{-\infty}^{\infty} S_H(\nu)d\nu} - \left(\frac{\int_{-\infty}^{\infty} \nu S_H(\nu)d\nu}{\int_{-\infty}^{\infty} S_H(\nu)d\nu}\right)^2} \quad (1.23)$$

Similarly, the *power-delay profile* is given by

$$S_H(\tau) = \int_{-\infty}^{+\infty} S_H(\nu,\tau)\, d\nu$$

The *Delay spread* σ_τ is defined as the square root of the second centred moment of the power-delay profile:

$$\sigma_\tau = \sqrt{\frac{\int_{-\infty}^{\infty} \tau^2 S_H(\tau)d\tau}{\int_{-\infty}^{\infty} S_H(\tau)d\tau} - \left(\frac{\int_{-\infty}^{\infty} \tau S_H(\tau)d\tau}{\int_{-\infty}^{\infty} S_H(\tau)d\tau}\right)^2} \quad (1.24)$$

Since the Doppler spectrum and the time autocorrelation function are Fourier transform pairs, a large Doppler spread σ_ν will result in small coherence time T_C and therefore faster temporal fading and vice versa. Similarly, the power-delay profile and the frequency autocorrelation function are Fourier transform pairs. Hence, a large delay spread σ_τ will result in a small coherence bandwidth B_C and vice versa. In practice, the four parameters are related by

$$B_C \approx 1\!\!\Big/\!\!{2\sigma_\tau} \quad (1.25)$$

and

$$T_C \approx 1\!\!\Big/\!\!{2\sigma_\nu} \quad (1.26)$$

1.1.3.6 Frequency-Space Transform Mapping

For a static channel, we may extend the time-frequency ma p described in the previous paragraph for the *frequency-space* relationship as illustrated in Figure 1.6.

In this diagram, the joint space-frequency autocorrelation $R_H(\Delta f, \Delta r)$ and the joint delay-wavenumber spectrum $S_H(\tau, k)$ are related by Fourier transform pairs. In section 1.2.2, we have introduced the concepts of *coherence distance* and *angle spread* for deterministic channels. We shall try to extend the definition of these parameters for WSSUS random channels. From the frequency-space autocorrelation function, the single dimension spatial autocorrelation of the random channels is given by

$$R_H(\Delta r) = R_H(\Delta f, \Delta r)\big|_{\Delta f = 0} \quad (1.27)$$

The coherence distance D_C is therefore defined as the maximum Δr such that $R_H(\Delta r) < 0.5$.

Similarly, we can characterize the statistical behaviour of the random channels by the *delay-wavenumber spectrum* $S_H(\tau, k)$. Consider the single-dimension wavenumber spectrum $S_H(k)$:

$$S_H(k) = \int_{-\infty}^{+\infty} S_H(\tau, k)\, d\tau \quad (1.28)$$

The *angle spread* σ_k is defined as the square root of the second centred moment of the Doppler spectrum:

$$\sigma_k = \sqrt{\frac{\int_{-\infty}^{\infty} k^2 S_H(k)dk}{\int_{-\infty}^{\infty} S_H(k)dk} - \left(\frac{\int_{-\infty}^{\infty} k S_H(k)dk}{\int_{-\infty}^{\infty} S_H(k)dk}\right)^2} \quad (1.29)$$

An important indication of the nature of the channel is called the *spread factor*, given by $B_C T_C$. If $B_C T_C < 1$, the channel is said to be *underspread*; otherwise, it is called *overspread*. In general, if $B_C T_C << 1$, the channel impulse response could be easily measured and the measurement could be utilized at the receiver for demodulation and detection or at the transmitter for adaptation. On the other hand, if $B_C T_C >> 1$, channel measurement would be extremely difficult and unreliable.
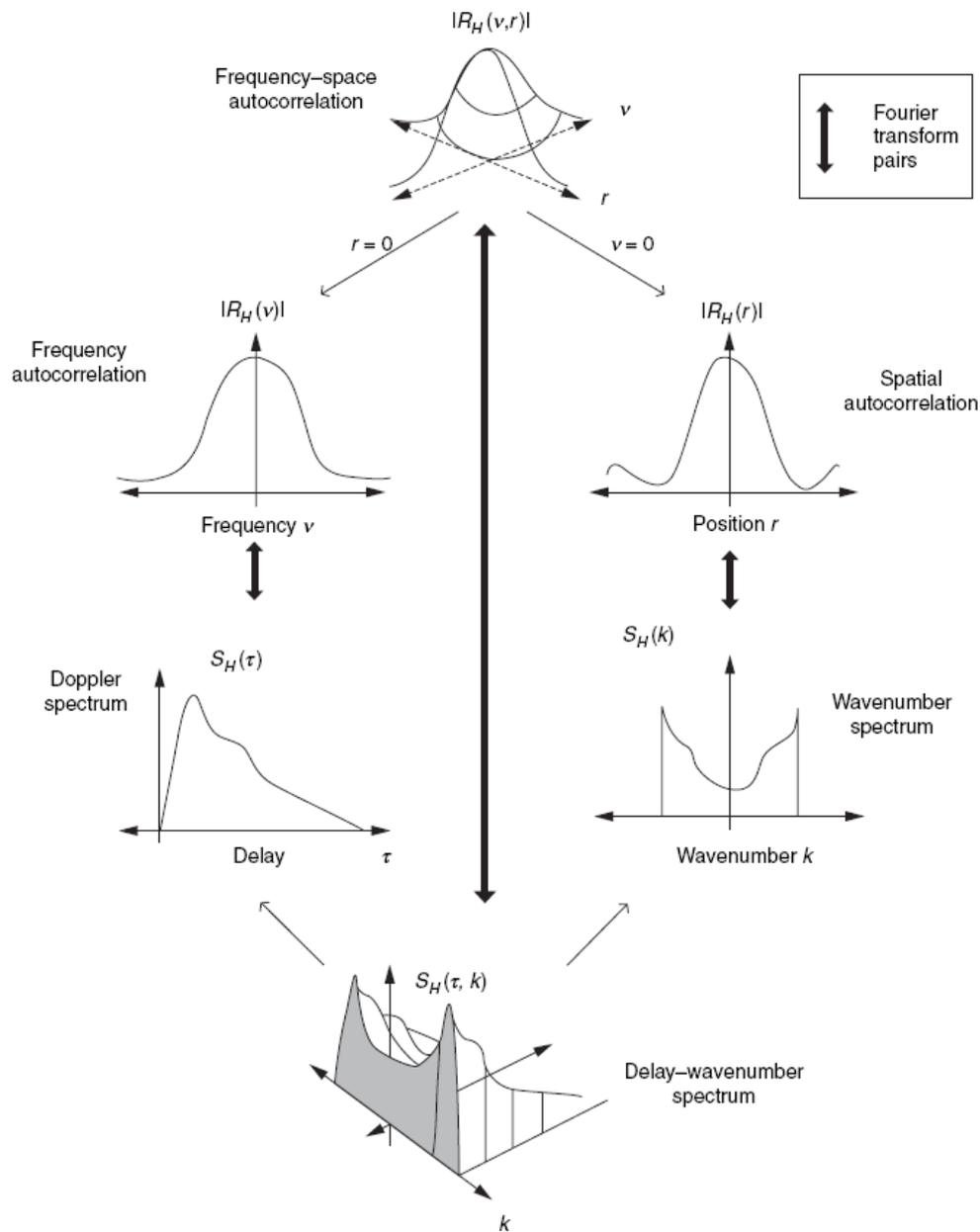
Figure 1.7 – Illustration of frequency-space autocorrelation and delay-wavenumber spectrum

1.2 Multiantenna (MIMO) Systems

Figure 1.8 illustrates different antenna configurations used in defining space-time systems. Single-input single-output (SISO) is the well-known wireless configuration, single-input multiple-output (SIMO) uses a single transmitting antenna and multiple (N_R) receive antennas, multiple-input single-output (MISO) has multiple (N_T) transmitting antennas and one receive antenna, MIMO has multiple (N_T) transmitting antennas and multiple (N_R) receive antennas and,

finally, MIMO-multiuser (MIMO-MU), which refers to a configuration that comprises a base station with multiple transmit/receive antennas interacting with multiple users, each with one or more antennas. We now examine the meaning of certain terms.
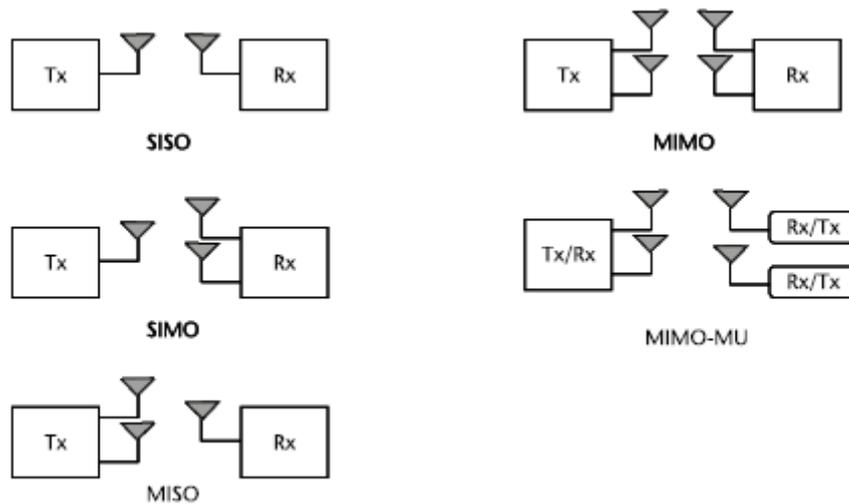
Figure 1.8 – Different antenna configurations in space-time systems

In general MIMO systems make use of a combination of different transmission techniques (called space-time processing techniques) in order to exploit the multipath propagation (Figure 1.9)
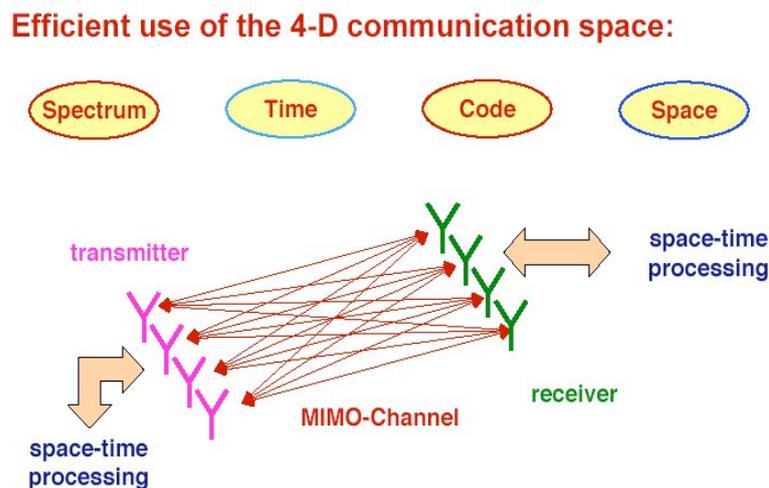
Figure 1.9 – Illustration of capabilities of space-time systems

Such techniques are used to get some advantages w.r.t. traditional wireless systems, and these advantages are usually termed *Array Gain, Diversity Gain and Multiplexing Gain* (Figure 1.10).
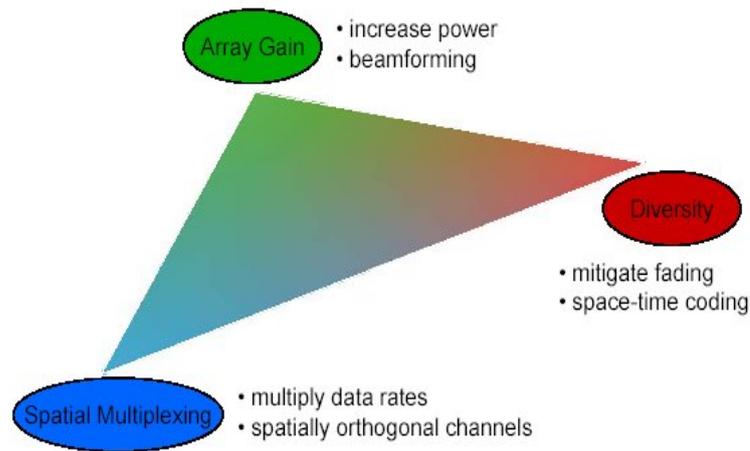
Figure 1.10 – Illustration of the performance increase of MIMO systems w.r.t SISO systems

1.2.1 Array Gain

Array gain (or beamforming gain) is the average increase in the signal-to-noise ratio (SNR) at the receiver that arises from the coherent combining effect of multiple antennas at the receiver or transmitter or both. If the channel is known to the multiple antenna transmitter, the transmitter will weight the transmission with weights, depending on the channel coefficients, so that there is coherent combining at the single antenna receiver (MISO case). The array gain in this case is called transmitter array gain. Alternately, if we have only one antenna at the transmitter and no knowledge of the channel and a multiple antenna receiver, which has perfect knowledge of the channel, then the receiver can suitably weight the incoming signals so that they coherently add up at the output (combining), thereby enhancing the signal. That is the SIMO case. This is called receiver array gain. Basically, multiple antenna systems require perfect channel knowledge either at the transmitter or receiver or both to achieve this array gain.

1.2.2 Diversity Gain

Multipath fading is a significant problem in communications. In a fading channel, signal experiences fades (i.e., they fluctuate in their strength). When the signal power drops significantly, the channel is said to be in a fade. This gives rise to high bit error rates (BER). We resort to diversity to combat fading. This involves providing replicas of the transmitted signal over time, frequency, or space. There are three types of diversity schemes in wireless communications.

- *Temporal diversity*: In this case replicas of the transmitted signal are provided across time by a combination of channel coding and time interleaving strategies. The key requirement here for this form of diversity to be effective is that the channel must provide sufficient variations in time. It is applicable in cases where the coherence time of the channel is small compared with the desired interleaving symbol duration. In such an event, we are assured that the interleaved symbol is independent of the previous symbol. This makes it a completely new replica of the original symbol.

- *Frequency diversity*: This type of diversity provides replicas of the original signal in the frequency domain. This is applicable in cases where the coherence bandwidth of the channel is small compared with the bandwidth of the signal. Thos assures us that different parts of the relevant spectrum will suffer independent fades.

- *Spatial diversity*: This is also called antenna diversity and is an effective method for combating multipath fading. In this case, replicas of the same transmitted signal are provided across different antennas of the receiver. This is applicable in cases where the antenna spacing is larger than the coherence distance to ensure independent fades across different antennas. The traditional types of diversity schemes are *selection diversity, maximal ratio diversity,* and *equal gain diversity*. *Space-time codes* exploit diversity across space and time.

Basically the effectiveness of any diversity scheme lies in the fact that at the receiver we must provide *independent* samples of the basic signal that was transmitted. In such an event we are assured that the probability of two or more relevant parts of the signal undergoing deep fades will be very small. The constraints on coherence time, coherence bandwidth, and coherence distance ensure this. The diversity scheme must then optimally combine the received diversified waveforms so as to maximize the resulting signal quality. We can also categorize diversity under the subheading of spatial diversity, based on whether diversity is applied to the transmitter or to the receiver.

- *Receive diversity*: Maximum ratio combining is a frequently applied diversity scheme in receivers to improve signal quality. In cell phones it becomes costly and cumbersome to deploy. This is one of the main reasons transmit diversity is easier to implement at the base station.

- *Transmit diversity*: In this case we introduce controlled redundancies at the transmitter, which can be then exploited by appropriate signal processing techniques at the receiver. Generally this technique requires complete channel information at the transmitter to make this possible. But with the advent of space-time coding schemes like Alamouti's scheme, it became possible to implement transmit diversity *without* knowledge of the channel. This was one of the fundamental reasons why the MIMO industry began to rise. Space-time codes for MIMO exploit both transmit as well as receive diversity schemes, yielding a high quality of reception.

Therefore, in MIMO we talk a lot about receive antenna diversity or transmit antenna diversity. In receive antenna diversity, the receiver that has multiple antennas receives multiple replicas of the same transmitted signal, assuming that the transmission came from the same source. This hold true for SIMO channels. If the signal path between each antenna pair fades independently, the when one path is in a fade, it is extremely unlikely that all the other paths are also in deep fade. Therefore, the loss of signal power due to fade in one path is countered by the same signal but received through a different path (route). This is like a line of soldiers. When one soldier falls in battle, another is ready to take his place. Hence, extending this analogy further, the more the soldiers, the stronger the line. The same in the argument in diversity. The more the diversity, the easier we can combat fades in a channel. Diversity is characterized by the number of independent fading branches, or paths. These paths are also known as *diversity order* and are equal to the number of receive antennas in SIMO channels. Logically, the higher the diversity order (independent fading paths, ore receive antennas), the better we combat fading. If the number of receive antennas tends to infinity, the diversity order tends to infinity and the channel tends to additive white Gaussian noise (AWGN).

In the category of spatial diversity there are two more types of diversity that we need to consider. These are:

- *Angle diversity*: If the radiation patterns of the antennas are different, then each multipath will be weighted differently by them. When the antennas share the same polarization but have different magnitude and phase responses in different directions, this is the traditional *angle*

diversity. In many cases, this diversity technique can be extremely hard to exploit. In practice, angle diversity applies only at carrier frequencies in excess of 10 GHz. At such frequencies, the transmitted signals are highly scattered in space. In such an event the receiver can have two highly directional antennas facing in totally different directions. This enables the receiver to collect two samples of the same signal, which are totally independent of each other.

- *Polarization diversity*: In this type of diversity signals having orthogonal polarizations (i.e. vertical and horizontal) are transmitted by two or more different polarized antennas and received correspondingly by two or more different polarized antennas at the receiver. Different polarizations ensure that there is no correlation between the data streams, without having to worry about coherent distance of separation between the antennas.

It is noteworthy that both angle and polarization diversity are subsets of the more inclusive *pattern diversity,* which simply implies that the antenna radiation patterns (magnitude, phase and polarization) differ to create the unique multipath weighting.

1.2.3 Spatial Multiplexing (Multiplexing Gain)

Spatial multiplexing offers a linear (in the number of transmit-receive antenna pairs or $\min\{N_R, N_T\}$) increase in the transmission rate (or capacity) for the same bandwidth and with no additional power expenditure. It is only possible in MIMO channels. Consider the case of two transmit and two receive antennas. This can be extended to more general MIMO channels.

The bit stream is split into two half-rate bit streams, modulated and transmitted simultaneously from both the antennas. The receiver, having complete knowledge of the channel, recovers these individual bit streams and combines them so as to recover the original bit stream. Since the receiver has knowledge of the channel it provides receive diversity, but the system has no transmit diversity since the bit streams are completely different from each other in that they carry totally different data. Thus spatial multiplexing increases the transmission rates proportionally with the number of transmit-receive antenna pairs.

This concept can be extended to MIMO-MU. In such a case, two users transmit their respective information simultaneously to the base station equipped with two antennas. The base station can separate the two signals and can likewise transmit two signals with spatial filtering so that each user can decode his or her own signal correctly. This allows capacity to increase proportionally to the number of antennas at the base station and the number of users.

1.3 MIMO parameters definition

The input-output relation for a time-invariant and flat-fading MIMO system with N_T Tx antennas and N_R Rx antennas (Figure) is [2, 3]:

$$\mathbf{y=Hx+n} \quad (1.31)$$

where $\mathbf{H}$ is the channel matrix, $\mathbf{x}$ and $\mathbf{y}$ are the vectors of the transmitted and received signals, and $\mathbf{n}$ is the additive noise.
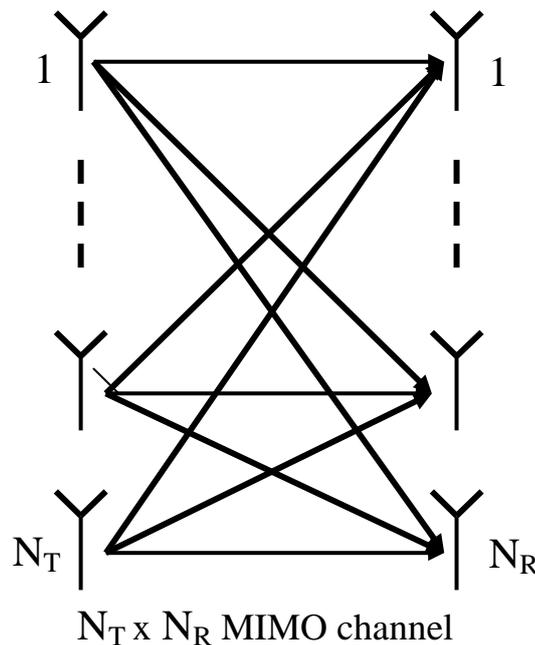
N_T x N_R MIMO channel

Figure 1.10 – Illustration of a N_T x N_R MIMO channel

The mutual information per unit bandwidth of a MIMO flat-fading channel with no Channel State Information (CSI) at the Tx is [1, 2, 4]:

$$I = \log_2 \det\left(\mathbf{I}_{N_R} + \frac{\rho}{N_T} \mathbf{H}\,\mathbf{H}^H \right) \ \text{bit/s/Hz} \qquad (1.32)$$

In a fading channel, I is in general a random variable, due to the statistical nature of $\mathbf{H}$ (for example, for a Rayleigh fading channel, the generic element h_{ij} can be assumed as a complex Gaussian zero-mean random variable). ρ is the mean signal-to-noise ratio at each receiver branch, as long as the elements of $\mathbf{H}$ are properly normalized so that the following relation is satisfied:

$$E\left\{\mathrm{tr}\left[\mathbf{H}\,\mathbf{H}^{H}\right]\right\}= E\left\{\|\mathbf{H}\|_{F}^{2}\right\}= N_{T}N_{R}$$

where $\|\mathbf{H}\|_{F}^{2}$ is the squared Frobenius norm of $\mathbf{H}$. Some synthetic performance parameters follow from I, such as the ergodic capacity [2], which is the expectation of I over all the possible realizations of $\mathbf{H}$:

$$C = E_{H}\{I\}= E_{H}\left\{\log_{2}\det\left(\mathbf{I}_{\mathrm{N_R}}+\frac{\rho}{N_{T}}\mathbf{H}\,\mathbf{H}^{H}\right)\right\} \quad (1.33)$$

and the outage capacity [3], which is the capacity guaranteed in the (1-q) % of the cases:

$$\mathrm{Pr}ob\{C(\mathrm{t}_{0}) < C_{out}\}= q \quad (1.34)$$

Expression (1.33) represents the maximum capacity - in the Shannon sense - only if the $\mathbf{H}$ elements are independent and identically distributed (i.i.d.) (i.e. h_{ij} are uncorrelated), but in correlated channels it can be regarded as a lower bound of the maximum capacity. The performance of the MIMO channel in terms of maximum achievable capacity is strongly influenced by the correlation between the elements of $\mathbf{H}$, which depends on the multipath richness of the considered scenario, and can be directly related to synthetic propagation parameters such as RMS Delay spread (DS) and RMS Angle spread at the Rx (RxAS) or at the Tx (TxAS) [56].

In many situations of common practice, the flat-fading channel assumption is not realistic, so the channel matrix and the mutual information of the frequency-selective MIMO channel must be considered:

$$I_{FS}= \frac{1}{B}\int_{B}\log_{2}\det\left(\mathbf{I}_{N_{R}}+\frac{\rho}{N_{T}}\tilde{\mathbf{H}}(f)\tilde{\mathbf{H}}(f)^{H}\right)df \quad \text{bit/s/Hz} \quad (1.35)$$

Chapter 2

Modelling of Diffuse Scattering From Buildings

2.1 - Introduction

Recently, the adoption of Ray Tracing (RT) tools has greatly improved field prediction capabilities in urban environment and good results have been obtained in a variety of cases [29-32]. However, since conventional RT only accounts for rays that undergo specular reflections or diffractions, it fails to properly describe diffuse scattering phenomena which can have a significant impact on radio propagation in urban areas. As intended here, diffuse scattering refers to the signals scattered in other than the specular direction (Figure 2.1) as a result of deviations (surface or volume irregularities) in a building wall from a uniform flat layer.
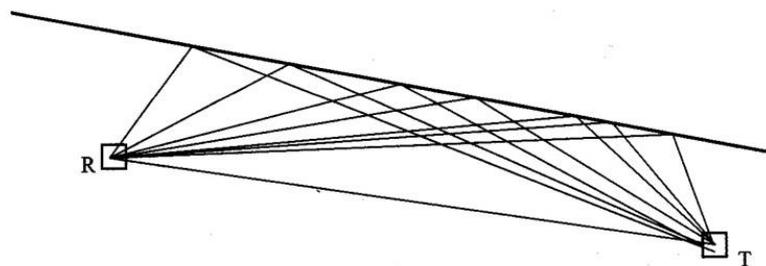
Illustration of diffuse incoherent scattering from a rough surface. Contributions arrive from all parts of the surface, not just from the specular reflection point

Figure 2.1 – Illustration of diffuse scattering from a rough surface (top view)

Recent experimental studies have shown that diffuse scattering contributions due to buildings or even lampposts plays an important role in determining time

and angle dispersion of radio signals in real environments [36,37,39]. The modeling of diffuse scattering from buildings is quite a difficult problem, since building wall irregularities cannot be modeled as Gaussian surface roughness (see Figure 2.2), as assumed in most theoretical models.
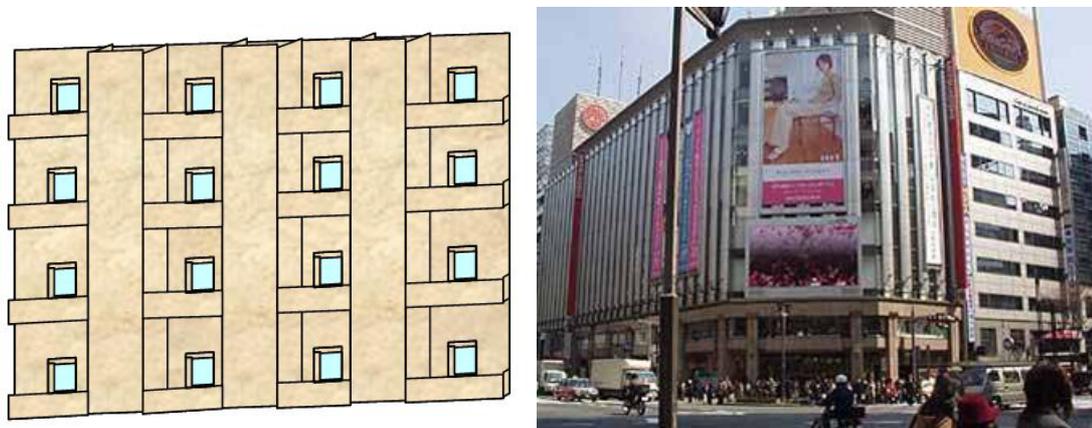
Figure 2.2 – Examples of real building walls with irregularities and protruding elements

Few publications explicitly deal with modeling of diffuse scattering from buildings [36,37,45-47]. In particular, in [36] and [37] a simple "Effective Roughness" (ER) model for diffuse scattering from building walls has been proposed, and in [38] the same model has been inserted into a 3D ray tracing program, showing a sensible improvement in the accuracy of wideband predictions vs. measurements with respect to conventional RT. The ER model described in [36,37], however, assumes that the wave impinging on a wall element (or on an entire wall if the wall is far from the radio terminals) is scattered according to a Lambertian scattering pattern regardless of the direction of incidence.

In the present work the ER model has been modified by orienting the scattering pattern lobe toward the specular direction, which is more realistic, and re-shaping it in a number of different ways while preserving the physical consistency of the model (paragraph 2.2). Then, the scattering pattern of real building walls has been measured using directive antennas and an appropriate measurement set-up (paragraph 2.3).

Finally, the experimental scattering patterns have been compared with simulation obtained through the modified ER model embedded into a 3D RT tool (sections IV-V), thus determining the best scattering pattern shape and the best

values of the scattering coefficient S in the considered cases. Results and conclusions are drawn in sections VI and VII, respectively.

2.2 – The Diffuse Scattering Models

The contribution of diffuse scattering to propagation is evaluated adopting the "Effective Roughness" (ER) approach presented in [36,37]. A sort of effective roughness is associated with each wall, which not only takes into account real surface roughness but also the wall irregularity effect in a mean, statistical way. In the ER model the field scattered by the generic wall element dS (Figure 2.3) is modeled as a non uniform spherical wave which departs from the element and propagates in the upper half space. Precisely, the power density carried by the scattered wave is proportional to $\left|\overline{E}_s\right|^2 = \left|\overline{E}_s(r_s,\theta_s,\phi_s)\right|^2$, where $\overline{E}_S$ is the intensity of the scattered field, which is evaluated according to a proper scattering coefficient (S) and a "scattering pattern", both depending on the characteristics of wall irregularities (see below).

In order to account for a wide range of possible situations, different choices can be done in defining both the scattering coefficient and the scattering pattern, so different categories of models can be hypothesized.
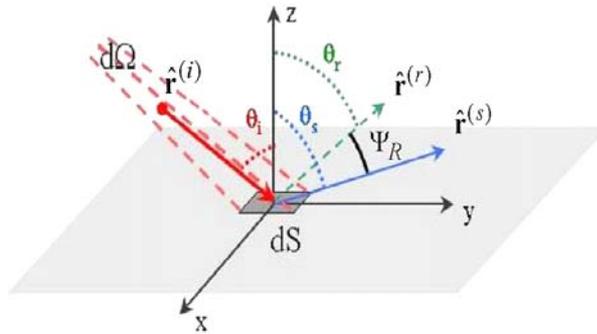
Figure 2.3 – A generic surface element producing reflection and diffuse scattering

We can distinguish between two different approaches.

In the first approach the scattering parameter is defined as:

$$S = \left.\frac{\left|\overline{E}_S\right|}{\left|\overline{E}_i\right|}\right|_{ds} \quad (2.1)$$

where $\left|\overline{E}_i\right|$ and $\left|\overline{E}_S\right|$ are the norms of the incident and scattered fields on the

surface element dS, respectively. Since dS is infinitesimal, the fields are assumed constant on it. In other words, S^2 is the percentage of the power impinging on the wall element which is spread in all directions. Following this approach, the overall power balance on the surface element dS can be written as [36,37]:

$$1 = \Gamma^2 R^2 + S^2 + {P_p}\big/{P_i} \quad (2.2)$$

where $\Gamma = \dfrac{\left|\overline{E}_R\right|}{\left|\overline{E}_i\right|}$, R is the "reflection reduction factor", P_p is the power which penetrates the wall and P_i is the incident one. Γ and the reflected field $\overline{E}_R$ can be determined using the well-known Fresnel reflection coefficients. Assuming that P_p/P_i is weekly dependent on the characteristics of wall irregularities as in [36], we can neglect its dependence with S, that is, the greater S, the lower R. With this assumption the power balance for an ideal, smooth wall becomes (S=0, R=1):

$$1 = \Gamma^2 + {P_p}\big/{P_i} \quad (2.3)$$

Combining equations (2.2) and (2.3), a simple relation between R and S can be obtained:

$$R \cong \sqrt{1 - \frac{S^2}{\Gamma^2}} \quad (2.4)$$

Since S and R are real parameters in the range [0,1] and Γ depends on the incidence direction, if S is assumed to be a constant, equation (2.4) means that S cannot exceed the minimum among the possible values of Γ.

Following the second approach, the scattering coefficient is defined as:

$$S = \frac{\left|\overline{E}_S\right|}{\left|\overline{E}_R\right|}\Bigg|_{ds} \quad (2.5)$$

According to this definition, S^2 is the percentage of the power which is scattered in all directions at the expenses of the reflected power only. Therefore, the power balance can be rewritten as:

$$\frac{\left|\overline{E}_i\right|^2}{2\eta} dS \cos\theta_i = R^2 \frac{\left|\overline{E}_R\right|^2}{2\eta} dS \cos\theta_i + S^2 \frac{\left|\overline{E}_R\right|^2}{2\eta} dS \cos\theta_i + P_P$$

$$= R^2\Gamma^2 \frac{\left|\overline{E}_i\right|^2}{2\eta} dS \cos\theta_i + S^2\Gamma^2 \frac{\left|\overline{E}_i\right|^2}{2\eta} dS \cos\theta_i + P_P$$

where η is the intrinsic impedance of the medium. Therefore:

$$1 = \Gamma^2 (R^2 + S^2) + {P_P}/{P_i} \quad (2.6)$$

Similarly to the previous model, a relation between S and R can be obtained:

$$R \cong \sqrt{1 - S^2} \quad (2.7)$$

Hence, adopting the second approach S and R are both independent from the incidence direction and S can assume any value in the range [0,1].

The main difference between the two categories of ER models mentioned above is the definition of the scattering parameter S, but in both types of models the following synthetic relation (scattering power balance) must be satisfied:

$$S^2 \cdot U^2 \cdot \left|\overline{E}_i\right|^2 \cdot d\Omega_i \cdot r_i^2 =$$

$$= \int_{2\pi} \left|\overline{E}_s\right|^2 d\Omega_s \cdot r_s^2 = \int_0^{\pi/2} \int_0^{2\pi} \left|\overline{E}_s\right|^2 \cdot r_s^2 \cdot \sin\theta_s \, d\theta_s d\phi_s \quad (2.8)$$

where $d\Omega_i$ is the solid angle of the ray tube impinging on the surface element dS, and r_i, r_s are the distances between dS and source and reception points, respectively (Figure 2.4).
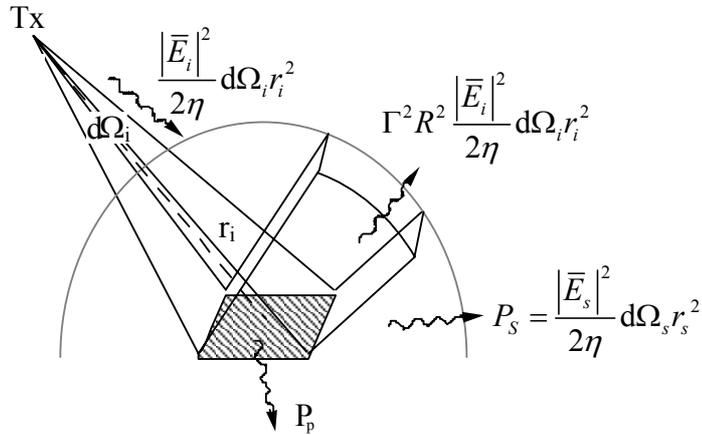
Figure 2.4 – The scattering power balance

U is a function depending on the definition adopted for the S parameter, and its value is:

$$U = \begin{cases} 1 & \text{if} \quad S = \left|\overline{E}_S\right|/\left|\overline{E}_i\right| \\ \Gamma & \text{if} \quad S = \left|\overline{E}_S\right|/\left|\overline{E}_R\right| \end{cases} \quad (2.9)$$

Introducing the actual assumed shape of the scattered wave $\left|\overline{E}_s(r_s,\theta_s,\phi_s)\right|$ (i.e.

the scattering pattern) in (2.8), its maximum amplitude E_{S0} can be derived. The shape of the scattering pattern of the wall strongly depends on the characteristics of wall irregularities (windows, balconies, irregular brick, surface roughness, indentations, etc.), so three different kinds of scattering patterns have been considered, each one representative of a practical situation.

Model 1 (Lambertian model):

$$\left| \overline{E}_s \right|^2 = E_{S0}{}^2 \cdot \cos\theta_s \quad (2.10)$$

The "scattering radiation lobe" is assumed to have its maximum in the direction perpendicular to the wall (Figure 2.5).

Lambertian scattering pattern

Wall element dS
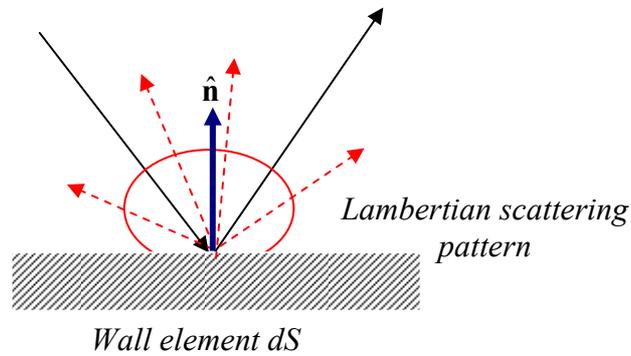
Figure 2.5 – Lambertian model

The exact expression of E_{s0} can be computed from (2.8), therefore getting [36,37]:

$$\left| \overline{E}_s \right|^2 = \left(\frac{K \cdot S}{r_i \cdot r_s} \right)^2 \cdot U^2 \cdot \frac{\cos\theta_i \cdot \cos\theta_s}{\pi} dS$$

where K is a constant depending on the amplitude of the impinging wave [37].

Model 2 (Directive model):
This model is based on the assumption that the scattering lobe is steered towards the direction of the specular reflection (Figure 2.6).
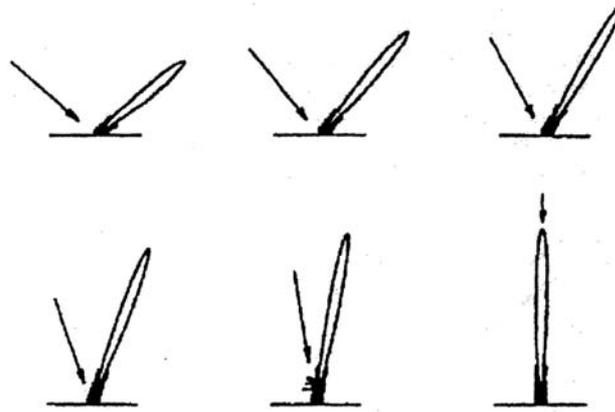
The main scattering lobe is always centered on the specular direction.

Figure 2.6 – Directive model (scattering lobe centred on the specular direction)

In order to comply with this assumption, the following expression is considered:

$$\left|\overline{E}_S\right|^2 = E_{S0}^2 \cdot \left(\frac{1+\cos \; \psi_R}{2}\right)^{\alpha_R} \quad \alpha_R = 1,2,...N \quad (2.11)$$

where ψ_R is the angle between the direction of the reflected wave and the scattering direction $(\theta_s \, , \, \phi_s)$ (Figure 2.3), and the exponent α_R is related to the width of the scattering lobe (i.e. the model directivity). According to (2.11), it is evident that the maximum is for $\Psi_R = 0$ (i.e. in the direction of specular reflection); moreover, the greater α_R, the narrower the scattering lobe. In Figure 2.7, the normalized scattering patterns of the directive scattering model (for $\alpha_R = 1,2,3$) are shown w.r.t. the Lambertian model, for an incidence angle of 30º.
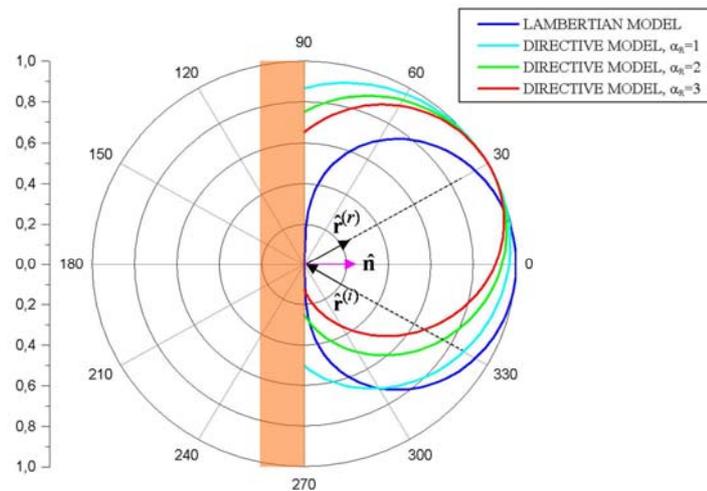
Figure 2.7 – Comparison of lambertian and single-lobe directive scattering patterns

The maximum amplitude E_{s0} can be computed by expressing the ψ_R angle through the incidence and scattering directions, and then solving equation (2.8). Through some algebraic manipulations, the following expression has been obtained (see Appendix A for details):

$$E_{S0}{}^2 = \left(\frac{S\,K}{r_i\,r_s}\right)^2 U^2 \frac{\cos\theta_i}{F_{\alpha_R}} dS$$

where

$$F_{\alpha_R} = \frac{1}{2^{\alpha_R}} \cdot \sum_{j=0}^{\alpha_R} \binom{\alpha_R}{j} \cdot I_j$$

and

$$I_j = \frac{2\pi}{j+1} \cdot \left[\cos\theta_i \cdot \sum_{w=0}^{\frac{j-1}{2}} \binom{2w}{w} \cdot \frac{\sin^{2w}\theta_i}{2^{2w}}\right]^{\left(\frac{1-(-1)^j}{2}\right)}$$

Model 3 (Backscattering lobe model):

This model is similar to the directive single-lobe model, but it includes an additional term accounting for backscattering phenomena. In fact, in several practical situations, for example in presence of very protruding surface irregularities (balconies, columns, etc.) and with grazing incidence angles, the diffuse scattering can originate non negligible contributions even in the proximity of the incidence direction ("billiard effect", see Figure 2.7).
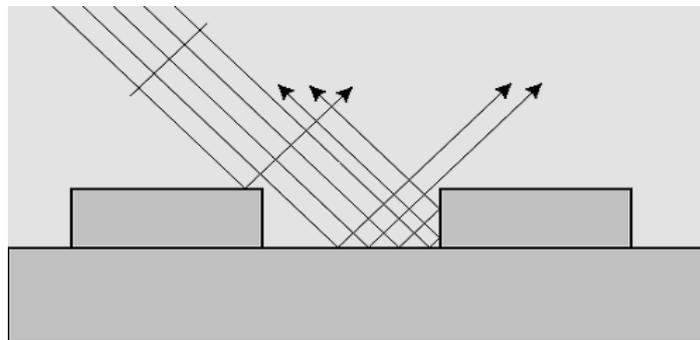
Figure 2.7 – Illustration of the "billiard effect"

A scattering lobe in the incident direction is therefore introduced. The expression of the double-lobe model is:

$$\left| \overline{E}_S \right|^2 = E_{S0}{}^2 \cdot \left[\Lambda \left(\frac{1 + \cos\ \psi_R}{2} \right)^{\alpha_R} + \left(1 - \Lambda\right) \left(\frac{1 + \cos\ \psi_i}{2} \right)^{\alpha_i} \right]$$

$$\alpha_i, \alpha_R = 1, 2, ..., N \ ; \quad \Lambda \in [0,1] \qquad (2.12)$$

where α_i, determine the width of the back-lobe and Λ is the repartition factor between the amplitudes of the two lobes. α_i and α_R have the same meaning as in the previous model (if α_i or α_R increase, the width of the respective lobe decrease). Λ can vary in the range [0,1], and for Λ=1 the model reduces to the single-lobe model seen above. In Figures 2.8 and 2.9 two examples of 3D double-lobe scattering patterns are shown, for an incidence angle of $\pi/4$, Λ=0.5 or 0.9, respectively, and for arbitrary values of the other parameters.
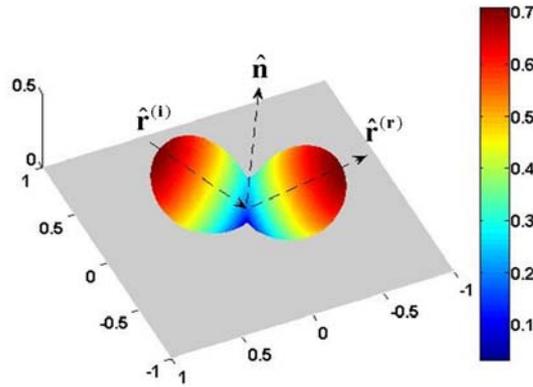
Figure 2.8 – 3D pattern of the double-lobe scattering model, for $\alpha_i = \alpha_R$=10, Λ=0.5 and $\theta_i = \pi/4$
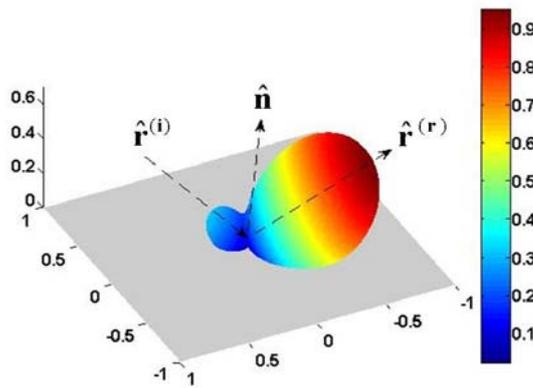
Figure 2.9 – 3D pattern of the double-lobe scattering model, for $\alpha_i = \alpha_R$=10, Λ=0.9 and $\theta_i = \pi/4$

The maximum amplitude E_{s0} of the scattered field for the double-lobe model, can be computed by expressing the angles α_i and α_R through the incidence, reflection and scattering directions, and then solving equation (2.8). Through

some algebraic manipulations, the following expression has been obtained (see Appendix A for details):

$$E_{S0}{}^2 = \left(\frac{S\,K}{r_i r_s}\right)^2 \cdot U^2 \cdot \frac{\cos\theta_i}{F_{\alpha_i,\alpha_R}}\,dS$$

where

$$F_{\alpha_i,\alpha_R} = \frac{\Lambda}{2^{\alpha_R}} \cdot \left[\sum_j^{\alpha_R}\binom{\alpha_R}{j}\cdot I_j\right] + \frac{(1-\Lambda)}{2^{\alpha_i}} \cdot \left[\sum_j^{\alpha_i}\binom{\alpha_i}{j}\cdot I_j\right]$$

and

$$I_j = \frac{2\pi}{j+1}\cdot\left[\cos\theta_i \cdot \sum_{w=0}^{\frac{j-1}{2}}\binom{2w}{w}\cdot\frac{\sin^{2w}\theta_i}{2^{2w}}\right]^{\left(\frac{1-(-1)^j}{2}\right)}$$

All the ER models seen above allow to estimate the amplitude of the scattered field $\overline{E}_s(r_s,\theta_s,\phi_s)$, but a complete model should also take into account its polarization characteristics. In general, due to the nature of diffuse scattering phenomena, which are the macroscopic effect of a large number of micro-interactions originated by wall irregularities, $\overline{E}_s(r_s,\theta_s,\phi_s)$ can be assumed an incoherent, non-polarized wave. Nevertheless, if the observation point $P_s(r_s,\theta_s,\phi_s)$ is fixed, a local polarization of the vector $\overset{\rho}{E}_s$ must still be present. In particular, assuming that the scattered field is polarized on a plane perpendicular to the propagation direction $\overline{r}_s$, as should be in the far-field region, and referring to a spherical reference system centred on the wall element (Figure 2.3), $\overset{\rho}{E}_s$ can be decomposed into two linearly polarized components (along $\hat{\theta}_s$ and $\hat{\phi}_s$). Furthermore, assuming for the time being that scattering is non-selective toward one or another component, i.e. the two components have equal intensities, the scattered field can be written as:

$$\overset{\rho}{E}_s = \left[\frac{1}{\sqrt{2}}\left|\overset{\rho}{E}_s\right|e^{j\chi_{\theta s}}\right]\hat{\theta}_s + \left[\frac{1}{\sqrt{2}}\left|\overset{\rho}{E}_s\right|e^{j\chi_{\phi s}}\right]\hat{\phi}_s \quad (2.13)$$

Where $\left|\overset{\rho}{E}_s\right|$ can be computed using the proposed scattering models, while the phases $\chi_{\theta s}$ and $\chi_{\phi s}$ are a-priori unknown, due to the incoherent nature of the

ER model. Since the ER models do not account for the phases of the components, the polarization of $\overset{V}{E}_s$ is also unknown. However, it is still possible to evaluate the scattered power Ps captured by an Rx antenna (see paragraph 2.4). For example, a linearly polarized, dipole antenna would capture half of the power coming from a scattered ray, etc.

2.3 - The Measurement Campaign

The measurement campaign consists in a set of CW measurements of the power scattered by 3 different building walls, with the Tx and the Rx equipped with directive antennas oriented toward the centre of the wall. Frequency was 1296 MHz, Tx power about 9 dBm, and the total cable losses were of about 5 dB. Three different types of building wall have been considered, each one representative of a different class: a metal, relatively smooth wall of an airport hangar (Figure 2.10), an uniform brick wall of a warehouse (Figure 2.11), and a typical brick wall with windows, doors and other elements of a rural building (Figure 2.12). All walls were nearly the same size of about 10 by 6 (height) meters.

Figure 2.10 – The metal wall

Figure 2.11 – The brick wall

Figure 2.12 – Brick wall of a typical rural building

A parabolic antenna with 1.5 m diameter was used in the Rx, while two different types of antenna were used to illuminate the wall: a circular horn antenna and a parabolic antenna with 1 m diameter. The wall was illuminated in 2 different modes: *normal* incidence (Tx2 in Figure 2.13) and *slant* incidence (Tx1 and Tx3). It is worth noticing that Tx1 and Tx3 are not equivalent, because the radiation pattern of the antennas is not perfectly symmetric (see Figures 6,7,8 in section VI).
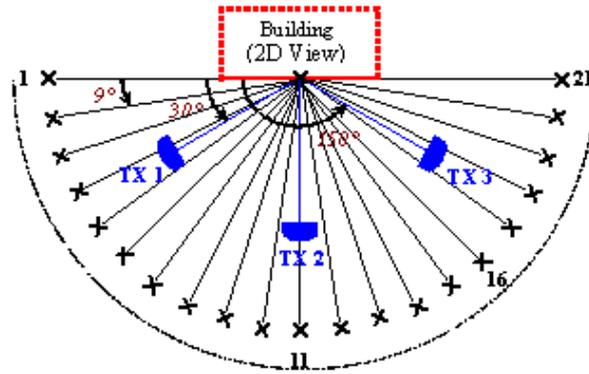
Figure 2.13 – Tx and Rx positions (top view)

The Rx antenna was moved on equispaced points (angular separation of 9°) on a semicircle centred in the centre of the wall. Rx antenna and annexed equipment (cables, receiver and a spectrum analyzer) were placed on a trolley equipped with an electromechanical pointing system with a video camera (see Figures 2.14 and 2.15).

Finally, in each case, the distance of the antennas from the wall centre was determined so that the –6 dB main lobe footprint on the wall would be all contained into the wall frame, in order to minimize the effect of the horizontal top edge and of surrounding objects (which were in all cases quite far). Since the size of the footprint is small with respect to the Rx antenna distance, the wall can be considered "far" as concerns its scattering behaviour [38]. The chosen distance was 3.8 m for the horn antenna, 9 m for the 1 m parabolic antenna, and 13 m for the 1.5 m parabolic antenna. Tx and Rx antennas were always at a height of 3 m from the ground. Given the relatively small distances, the Rx antenna wasn't in far field w.r.t. the Tx antenna for every Tx/Rx position. However, comparing measurements with RT simulations in reference, free space cases, we observed that deviations due to near-field effect were of the order of only a few dB's.
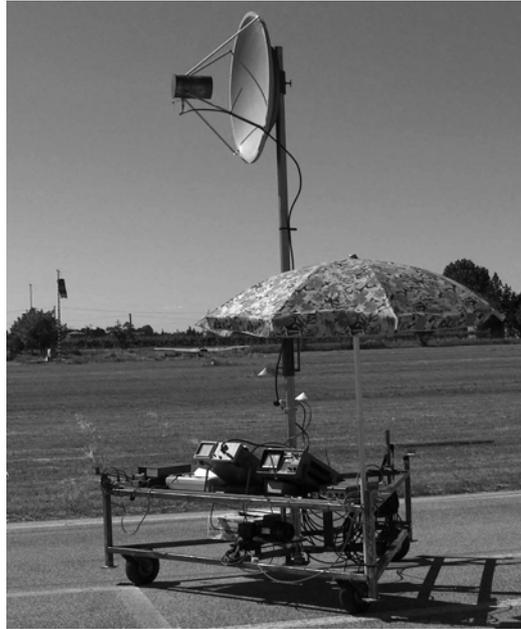
Figure 2.14 – The Rx antenna and the trolley

Figure 2.15 – The measurement instrumentation

2.4 – The Validation Method

All results reported in the following text are obtained using the 3D Ray Tracing simulator described in [38]. The performance of this software is improved w.r.t. traditional RT simulators through the introduction of the ER diffuse scattering model. Rays which experienced at least one diffuse scattering interaction along their path are treated incoherently by the program (see below).

The field carried by the i-th ray at the Rx point can be summarized with the following synthetic formula [38]:

$$\overset{\rho}{E}_i(Rx) = \left\{ \prod_{j=o}^{N_{EV}^i} \left[\overset{\mu}{D}^{o(i,j)}(P_{i,j}) \right] \overset{\rho}{E}_{i0}(Tx) \right\} \cdot$$

$$A\left(o(i,j), s_j, j = 0,..., N_{EV}^i\right) \quad i = 1,..., N_r \qquad (2.14)$$

where N_r is the number of rays, N_{EV}^i is the number of the interactions experienced by the i-th ray, $\overset{\mu}{E}_{i0}(Tx)$ is the field at a reference distance of 1 m from the Tx (in the direction of the i-th ray), *o(i,j)* represents the kind of interaction (reflection, diffraction, scattering), $P_{i,j}$ represents the spatial point where the j-th interaction is assumed to take place, $\overset{\mu}{D}$ is an appropriate dyadic to decompose the field into orthogonal components at the point $P_{i,j}$ and includes the proper attenuation coefficients (reflection coefficients, diffraction coefficients, etc.). Finally, A represents the overall divergence factor which depends on the lengths s_j (j=0,…, N_{EV}^i) of the segments composing the i-th path and on the interactions experienced by the ray. For each ray, the contribution to the received power is computed combining the field expressed in (2.14) with the gain and the polarization of the Rx antenna in the direction of the incoming ray, then all coherent contributions are summed taking into account modules and phases, getting the total coherent power P_c at the Rx.

Each ray undergoing at least one diffuse scattering interaction is assumed "incoherent". The field at the Rx is still computed through an "incoherent version" of formula (2.14) since formulas (2.10) to (2.12) can all be easily expressed as products of the transmitted field module $\overset{1}{E}_{i\,0}(Tx)$ multiplied by a "scattering coefficient". The power, however, is repartitioned in equal parts along the two components on the wavefront each time a scattering occurs according to eq. (2.13), and in addition any phase information is disregarded from there forth. The overall incoherent power P_{scat} is computed summing incoherently all the power contributions of incoherent rays.

Finally, the incoherent rays power P_{scat} is summed to the coherent rays power P_c obtaining therefore the total received power:

$$P_{tot}(Rx) = P_c + P_{scat} \qquad (2.15)$$

The models proposed above are checked with measurements according to the following procedure. Since it is impossible to single out only the diffuse scattering contribution from measurements, due to the limited directivity of the available antennas, measurements have been compared with accurate 3D RT simulations for all the considered wall topologies. Such RT simulations include specular reflection and UTD edge diffraction and consider the detailed radiation patterns of the antennas (see Figures 2.17, 2.18, 2.19). Standard electromagnetic characteristics were used for brick walls (ε_r=5, σ=1.e-2 (conductivity)) and of course perfect conductor characteristics for the metal hangar wall. The adopted 3D RT program [38] was equipped with all of the scattering models described in paragraph 2.2.

For simplicity, and due to the relatively small dimension of the illuminated footprint on the wall with respect to the Rx distance, a single scattered ray is computed for each Rx which is assumed to spring from the center of the wall, similarly to what is assumed in [38] for "far walls". The tuning of the scattering model is quite accurate because the scattering contribution is almost always dominant, except in the specular reflection and in back-to front peaks (see Figures 2.20 to 2.26 in the next paragraph).

2.5 - Results

Comparisons between measurements and RT predictions are shown in this paragraph. All Figures show the received power (measured and simulated) vs. the Rx angular position. All the antennas used in the measurement campaign have been preliminarily characterized on both the horizontal and the vertical plane. In Figures 2.16 and 2.17 the 2D radiation patterns of the Tx antennas (1 m parabolic and horn), are reported.
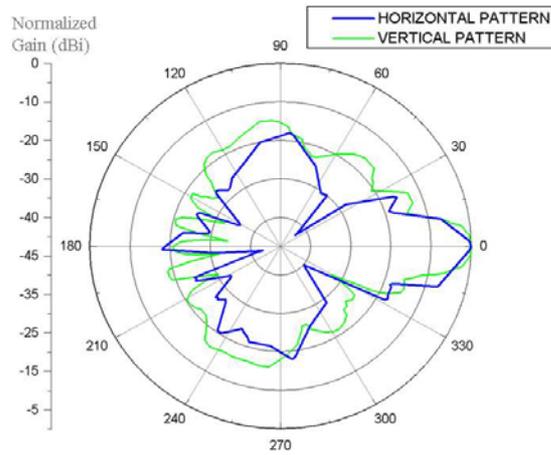
Fig 2.16 – 1 m parabolic TX antenna: 2D radiation patterns
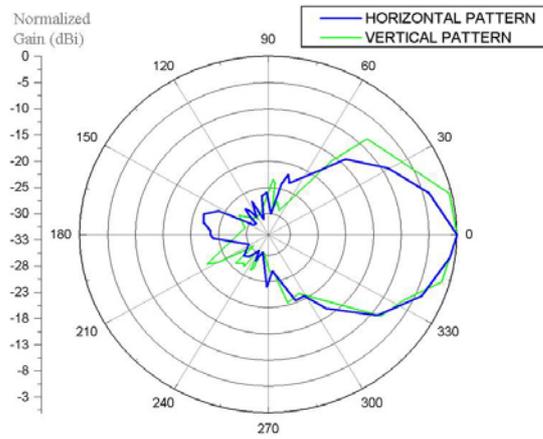
Fig 2.17 – Horn TX antenna: 2D radiation patterns

In Figure 2.18 the 2D radiation patterns of the Rx antenna (1,5 m parabolic) are reported.
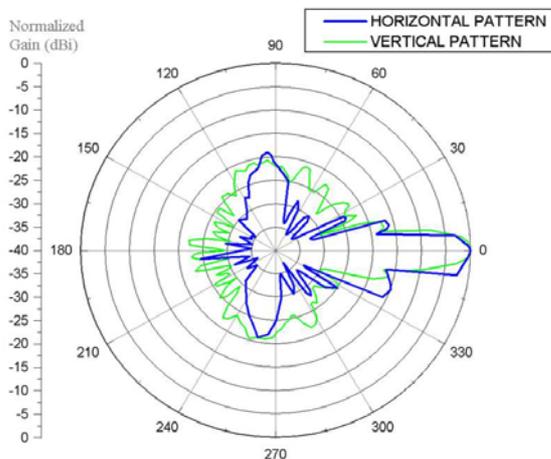
Fig 2.18 – 1,5 m parabolic TX antenna: 2D radiation patterns

In all cases, except where otherwise stated, the 1 m parabolic antenna is used at the Tx and the 1.5 m parabolic antenna is used at the Rx. Regarding polarization, results with both antennas having vertical excitations are shown, but further considerations on results with antennas in cross-polarized configurations are reported at the end of the section. Preliminarily, comparisons between measurements and RT simulations have been carried out in order to determine which definition of the scattering coefficient, between the (2.1) and the (2.5), better fits measurements. It has been found that adopting the first definition, it is difficult to find a single value of S valid for both slant and normal illumination of the wall. On the contrary, adopting definition (2.5), it is possible to obtain good results for both normal and slant illumination, keeping S constant.
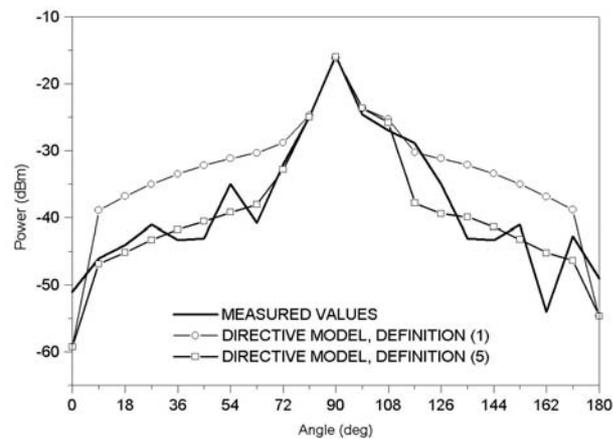
Fig 2.19 - Comparison of models using different definitions of the scattering coefficient - Brick wall; Tx antenna at 90°

In Figure 2.19 it is shown that assuming the optimum S value for slant illumination (S=0.2, for the brick wall), a good agreement with measurements can be obtained also for normal illumination if definition (2.5) is adopted, whereas received power is overestimated adopting definition (2.1). Therefore, all results shown in the following are related to definition (2.5).

Regarding the shape of the scattering pattern, further investigations have been performed in order to find the best ER model at minimum squares (minimum RMS distance). The single-lobe model demonstrated to be the best for all types of considered wall. Therefore the backscattering phenomena are not very important in the considered scenarios, probably due to the absence of very protruding irregularities.

In Figure 2.20 and Figure 2.21 a comparison obtained with the single-lobe

model (model 2) for different values of the parameter α_R is shown, in the case of the wall illuminated by a Tx antenna (1 m parabolic) pointed at 150° with respect to the wall plane (position 3 in Figure 2.13). The former shows the results obtained for the brick wall, the latter shows the same result for the rural building wall. The scattering coefficient S was set to 0.2 for the brick wall, and to 0.4 for the rural building wall. In both Figures also the results obtained using the Lambertian model (model 1) are reported, as a reference case. From the comparison it is evident that using the directive model the agreement is good in the central part of the graph whereas using the Lambertian model in the same zone the scattered power appears overestimated.
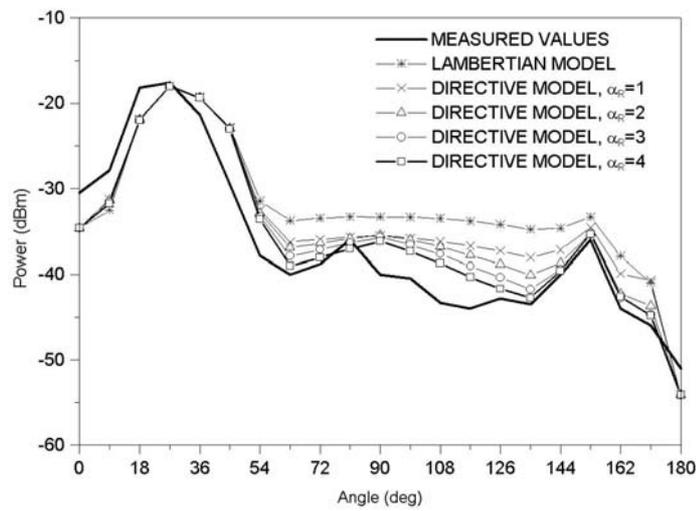
Fig 2.20 - Comparison of models - Brick wall; Tx antenna at 150°
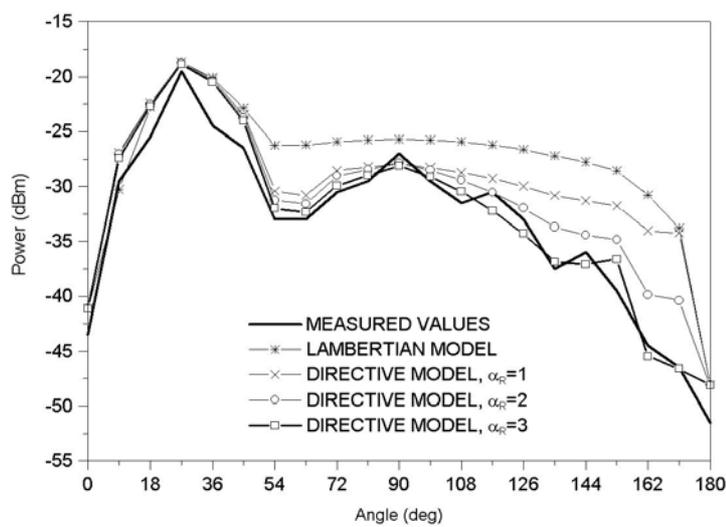
Fig 2.21 - Comparison of models – Rural building; Tx antenna at 150°

43

For the brick wall, α_R=4 has been found to be the value that guarantees the best RMS agreement with the measurements (Figure 2.20), while α_R=3 gives the best fit for the rural building wall (Figure 2.21). This is not evident from Figure 2.21 since the different curves are partially overlapped. However the respective RMS distances are reported in Table 2.1, and α_R=3 is proofed to give the best fit.

Scattering Model	RMS distance from measured values (dBm)
Lambertian Model	6.67
Model 2, α_R=1	4.81
Model 2, α_R=2	2.85
Model 2, α_R=3	1.85

Table 2.1 - RMS distance between simulated and measured curves reported in Figure 2.21

α_R=4 has been found to be the best-fit value also for the hangar wall. The lower value of the α_R parameter found for the rural building is probably due to the large number of irregularities typical of this wall, which reduce the directivity of the scattering pattern.

In Figures 2.22 to 2.26 comparisons between measurements and predictions for different values of the S parameter are shown: in all cases the single lobe ER model is adopted, which demonstrated to be the best in all topologies. All predictions are obtained using the directive model as a function of different α_R and S values, adopting the best RMS value for the fixed parameter (α_R), determined according to the procedure explained above, and varying S. In all the graphs, the dashed line represents prediction without scattering (S=0).
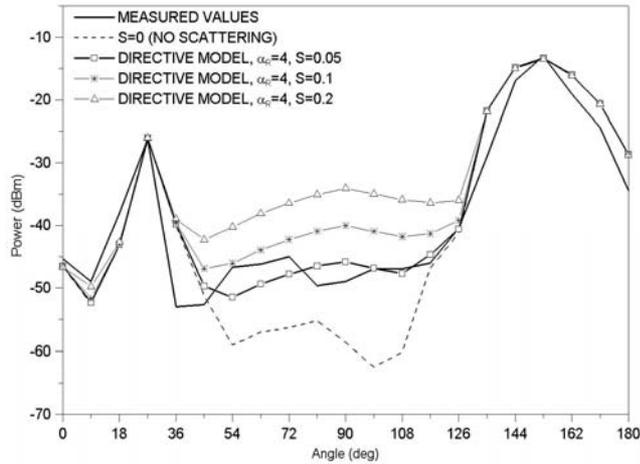
Fig 2.22 – Hangar wall illuminated with 1 m parabolic antenna at 30°

Figure 2.22 shows the received power vs Rx position as a function of S for the hangar wall case. The predicted power without scattering is slightly underestimated at some points, whereas using S=0.05 a good agreement with measurements is achieved everywhere. Therefore, in this case the scattering is useful for getting a good prediction in all receiving positions, but results obtained using traditional RT simulators (which do not take into account diffuse scattering) are still acceptable.

Similar results are shown in Figure 2.23 for the brick wall. In this case the best value of S is of about 0.2. Moreover, the Figure shows that neglecting the contribution of scattering (i.e. assuming S=0), the received power is underestimated in some central positions by as much as 20 dB.
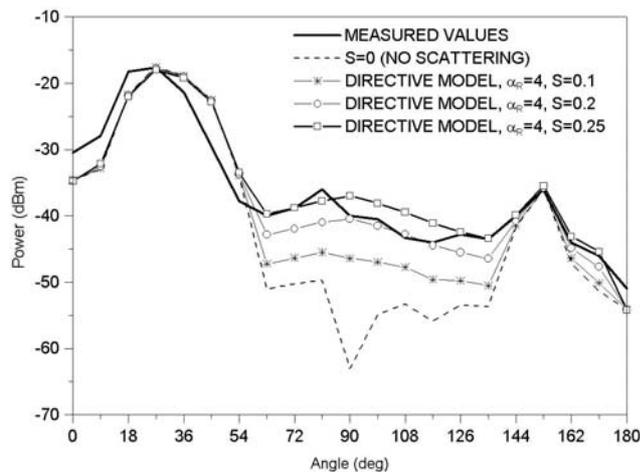
Fig 2.23 – Brick wall; Tx antenna at 150°

Finally, Figure 2.24 shows that predictions with S=0 are totally incorrect for a rural building wall, which is quite representative of many classes of real building walls: therefore in such cases the introduction of diffuse scattering is definitely necessary to get good results. The best value for S is 0.4 in this case, in agreement with previous studies [11-13].
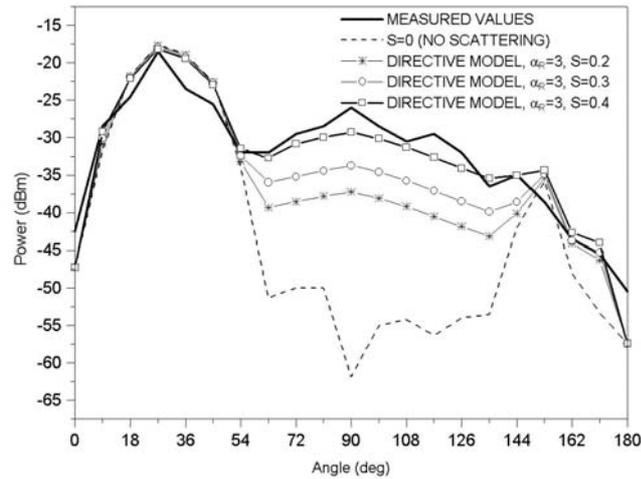
Fig 2.24 – Rural building; Tx antenna at 150°

In Figure 2.25 and Figure 2.26 the results for the brick wall and the rural building wall are shown in the case of normal illumination. Again, the results show the importance of diffuse scattering on propagation, and the optimum S values are the same as for slant illumination.
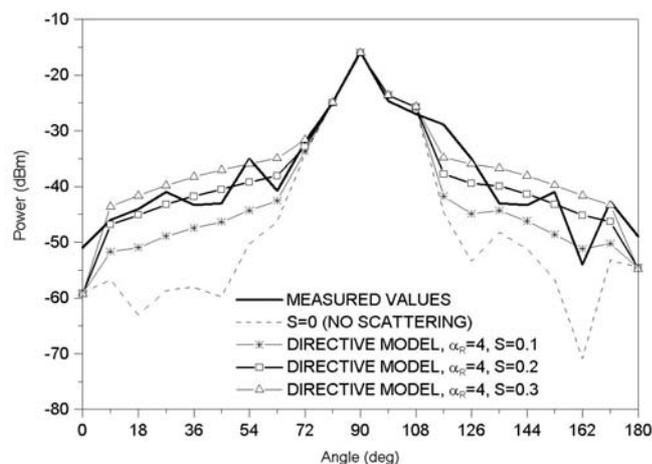
Fig 2.25 – Brick wall; Tx antenna at 90°
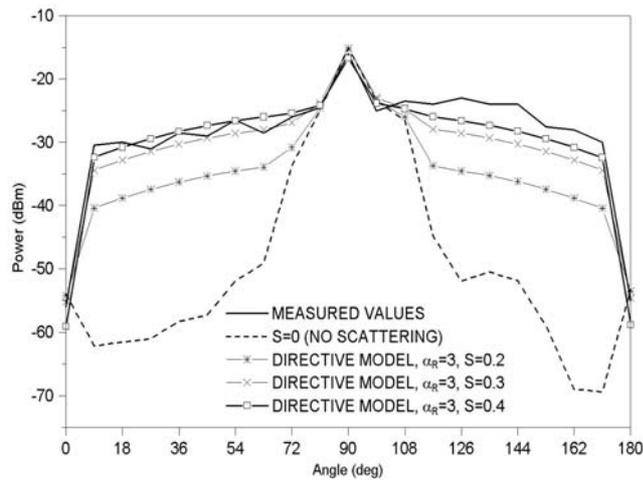
Fig 2.26 – Rural building; Tx antenna at 90°

In Figure 2.27 the results for the brick wall with normal incidence and with antennas in cross-polarized configuration are shown. In particular, results are obtained using the horn antenna with vertical excitation at the Tx, and the 1.5 m parabolic antenna with horizontal excitation at the Rx. Comparing measurement and simulation it can be noticed that, again, proper modeling of scattering is necessary to get correct received power values. A good agreement is obtained using the single-lobe model with the same parameter values which have been found to be optimum for the brick wall with antennas in co-polar configurations (α_R=3, S=0.2). The non-idealities of antennas (which can perturb the polarization of the field, increasing the coupling between antennas) have not been modeled so far. On the other hand, these non-idealities probably affect measured values (due, for example, to diffraction on the border of parabolic plate). For this reason, through simulations it is not possible to reproduce all received power fluctuations, however adding scattering the average behaviour is fairly predicted.
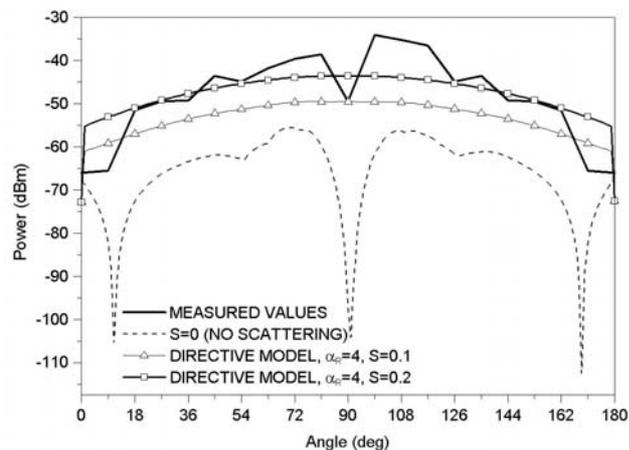
Fig 2.27 – Brick wall illuminated with the horn antenna at 90°: Tx and Rx antennas in cross-polarized configuration

2.6 The relationship between diffuse scattering and clustering

Several Authors have observed that urban and indoor multipath propagation is often associated to some kind of *clustering* effect, i.e. the property of different paths of being clustered together in sets with similar arrival/departure angles and propagation delays. This effect may allow simpler and more effective analysis and modeling of urban radio propagation [1,2]. Nevertheless, a convincing physical explanation of multipath-clustering in urban radio propagation is still lacking.

Since man-made objects are spatially clustered into walls, buildings, city-blocks, high-rise city cores etc. (see Figure), an impact of this *environment-clustering* on *multipath-clustering* can naturally be hypothesized.
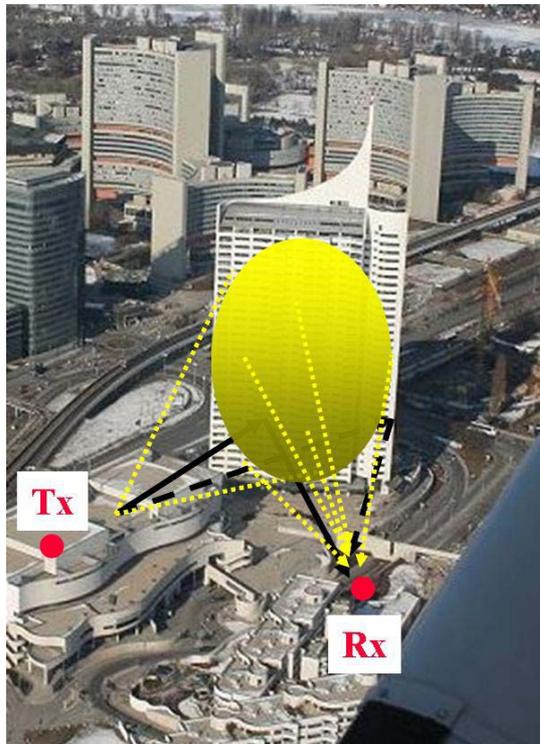
Figure 2.28 – Illustration of a building cluster

In the present work such a correlation is studied, and the important role played by diffuse scattering in this case is revealed.

In particular, the simple case of a single rectangular building wall is considered (see Figure 2.29). If only reflection and edge-diffraction were present, the total number of paths would be very low. But since the whole wall surface can backscatter energy due to surface roughness and irregularities, i.e. due to *diffuse scattering*, then a multitude of back-scattered rays take place, which show similar angles of arrival/departure and propagation delay. There is therefore a *cluster* of paths, which can be represented for example as a power-density function in the angle of arrival (theta, phi) domain (see Figure 2.30). Figure 2.30 has been obtained adopting the Effective Roughness diffuse scattering model [36,37,42], provided that the overall power balance be satisfied and assuming a slightly rough, perfectly conducting wall with S=0.1 and Lambertian scattering. In short, diffuse scattering produces a *scattering-cluster* "around" the specular reflection path (dashed line in Fig 2.30).

In the present work a novel method to compute the scattering-cluster in closed form in the mentioned case is derived. Therefore a novel kind of ray tracing is envisioned, which can a-posteriori add a sort of angle/time dispersion around the major paths (e.g. reflected path) on the base of the geometric and electromagnetic characteristics of the environment cluster (building wall, city block etc.) thus achieving a realistic prediction with a relatively low computation time.
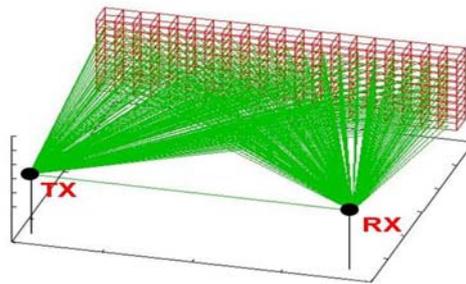
Figure 2.29 – Illustration of a rectangular, perfectly conducting wall and of rays scattered by each wall element
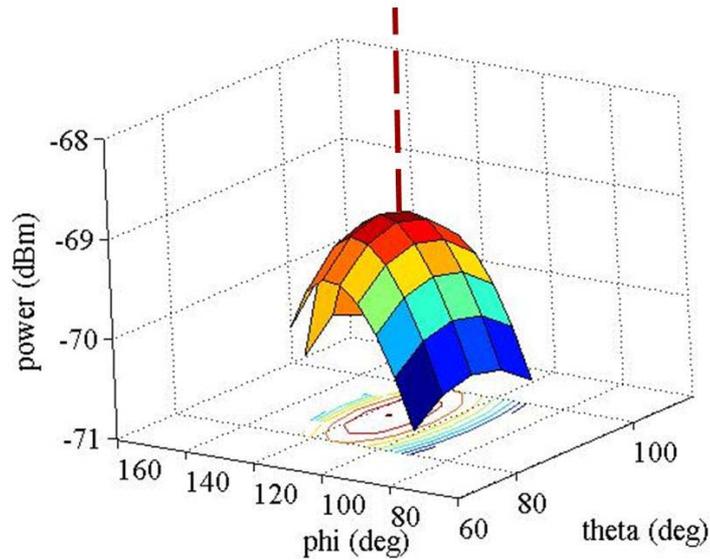
Figure 2.30 – Illustration of the scattering cluster produced by the rectangular wall of Fig. 2.29 in the multidimensional space (θ,ϕ,P). The dashed line represents the specular reflection contribution (not to scale).
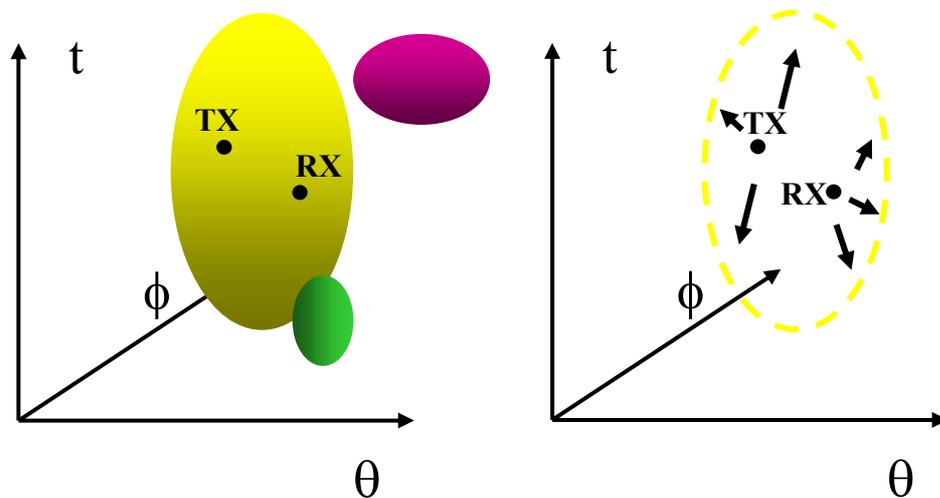
Figure 2.31 – Idealized representation of a cluster in the multidimensional domain (θ,ϕ,t) and expansion of the scattered micro-rays

If so, is it possible to *a-posteriori* expand major rays into clusters without computing the entire set of scattered micro-rays **?**

This should be done as a function of shape and orientation of *macro objects* (walls) with a modified ER approach.

Dispersive ray tracing ?

(great CPU time saving)

In the Lambertian case, for example, the total diffused power from a surface of area A can be therefore obtained through the following surface integral:

$$\left. \left| \bar{E}_s \right|^2_{TOT} = \int_A K_0^2 S^2 \frac{\cos\theta_i \cos\theta_S}{\pi} \frac{1}{r_i^2 r_S^2} dS = \frac{K_0^2 S^2}{\pi} \iint_A \frac{\cos\theta_i \cos\theta_S}{r_i^2 r_S^2} dx\, dy \right.$$
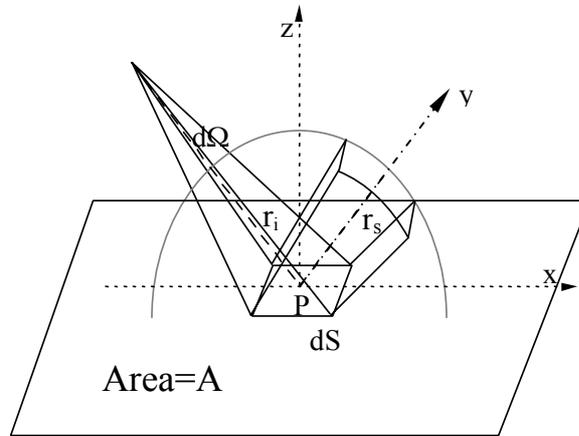
Figure 2.32 – Rectangular wall

If the surface is "far" from the terminals, thus distances do not change much over A, then we have a simpler expression:

$$\left. \left| \bar{E}_s \right|^2_{TOT} = K_0^2 S^2 \frac{\cos\theta_i \cos\theta_S}{\pi} \frac{1}{r_i^2 r_S^2} A \right.$$

If only the Tx is far from the wall, but not the Rx, we have:

$$\left. \left| \bar{E}_s \right|^2_{TOT} = \int_A K_0^2 S^2 \frac{\cos\theta_i \cos\theta_S}{\pi} \frac{1}{r_i^2 r_S^2} dS = \frac{K_0^2 S^2}{\pi} \frac{\cos\theta_i}{r_i^2} \iint_A \frac{\cos\theta_S}{r_S^2} dS \right.$$

$$\iint_A \frac{\cos\theta_S}{r_S^2}\,dS = \int_{x_m}^{x_M}\int_{y_m}^{y_M}\frac{\cos\theta_S}{r_S^2}\,dx\,dy = z_D\int_{x_m}^{x_M}\int_{y_m}^{y_M}\frac{1}{r_S^3}\,dx\,dy =$$

$$= z_D\int_{y_m}^{y_M}dy\int_{x_m}^{x_M}\frac{1}{\left[\sqrt{(x-x_D)^2+(y-y_D)^2+z_D^2}\right]^3}\,dx = I(x_D,y_D,z_D)$$

$$r_S = \sqrt{(x-x_D)^2+(y-y_D)^2+z_D^2} \quad \cos\theta_S = \frac{z_D}{r_S}$$

$$\begin{cases}x' = x - x_D\\ dx' = dx\end{cases}$$

$$\int\frac{1}{\sqrt{(x^2+a^2)^3}}\,dx = \frac{x}{a^2\sqrt{(x^2+a^2)}} + k$$

$$I(x_D,y_D,z_D) = z_D\int_{y_m}^{y_M}dy\int_{x_m-x_D}^{x_M-x_D}\frac{1}{\left[\sqrt{x'^2+(y-y_D)^2+z_D^2}\right]^3}\,dx' =$$

$$= z_D\int_{y_m}^{y_M}dy\left[\frac{x'}{\left[(y-y_D)^2+z_D^2\right]\sqrt{x'^2+(y-y_D)^2+z_D^2}}\right]_{x_m-x_D}^{x_M-x_D} =$$

$$= z_D\int_{y_m}^{y_M}\frac{x_M-x_D}{\left[(y-y_D)^2+z_D^2\right]\sqrt{(x_M-x_D)^2+(y-y_D)^2+z_D^2}}\,dy +$$

$$- z_D\int_{y_m}^{y_M}\frac{x_m-x_D}{\left[(y-y_D)^2+z_D^2\right]\sqrt{(x_m-x_D)^2+(y-y_D)^2+z_D^2}}\,dy$$

$$\begin{cases}y' = y - y_D\\ dy' = dy\end{cases}$$

$$\int\frac{1}{(y^2+a^2)\sqrt{y^2+a^2+b^2}}\,dy = \frac{1}{ab}\,arctg\left\{\frac{by}{a\sqrt{y^2+a^2+b^2}}\right\} + k$$

$$I(x_D, y_D, z_D) = z_D \int_{y_m - y_D}^{y_M - y_D} \frac{x_M - x_D}{\left[y'^2 + z_D^2 \right] \sqrt{y'^2 + z_D^2 + \left(x_M - x_D \right)^2}} dy' +$$

$$-z_D \int_{y_m - y_D}^{y_M - y_D} \frac{x_m - x_D}{\left[y'^2 + z_D^2 \right] \sqrt{y'^2 + z_D^2 + \left(x_M - x_D \right)^2}} dy' =$$

$$= z_D \left(x_M - x_D \right) \left[\frac{1}{z_D \left(x_M - x_D \right)} arctg \left\{ \frac{\left(x_M - x_D \right) y'}{z_D \sqrt{y'^2 + z_D^2 + \left(x_M - x_D \right)^2}} \right\} \right]_{y_m - y_D}^{y_M - y_D} +$$

$$-z_D \left(x_m - x_D \right) \left[\frac{1}{z_D \left(x_m - x_D \right)} arctg \left\{ \frac{\left(x_m - x_D \right) y'}{z_D \sqrt{y'^2 + z_D^2 + \left(x_m - x_D \right)^2}} \right\} \right]_{y_m - y_D}^{y_M - y_D} =$$

$$I(x_D, y_D, z_D) = arctg \left\{ \frac{\left(x_M - x_D \right)\left(y_M - y_D \right)}{z_D \sqrt{\left(x_M - x_D \right)^2 + \left(y_M - y_D \right)^2 + z_D^2}} \right\} - arctg \left\{ \frac{\left(x_M - x_D \right)\left(y_m - y_D \right)}{z_D \sqrt{\left(x_M - x_D \right)^2 + \left(y_m - y_D \right)^2 + z_D^2}} \right\} +$$

$$- arctg \left\{ \frac{\left(x_m - x_D \right)\left(y_M - y_D \right)}{z_D \sqrt{\left(x_m - x_D \right)^2 + \left(y_M - y_D \right)^2 + z_D^2}} \right\} + arctg \left\{ \frac{\left(x_m - x_D \right)\left(y_m - y_D \right)}{z_D \sqrt{\left(x_m - x_D \right)^2 + \left(y_m - y_D \right)^2 + z_D^2}} \right\}$$

$$\left| \overline{E}_s \left(x_D, y_D, z_D \right) \right|_{TOT}^2 = \frac{K_0^2 S^2}{\pi} \frac{\cos \theta_i}{r_i^2} \left[arctg \left\{ \frac{\left(x_M - x_D \right)\left(y_M - y_D \right)}{z_D \sqrt{\left(x_M - x_D \right)^2 + \left(y_M - y_D \right)^2 + z_D^2}} \right\} + \right.$$

$$- arctg \left\{ \frac{\left(x_M - x_D \right)\left(y_m - y_D \right)}{z_D \sqrt{\left(x_M - x_D \right)^2 + \left(y_m - y_D \right)^2 + z_D^2}} \right\} - arctg \left\{ \frac{\left(x_m - x_D \right)\left(y_M - y_D \right)}{z_D \sqrt{\left(x_m - x_D \right)^2 + \left(y_M - y_D \right)^2 + z_D^2}} \right\} +$$

$$\left. + arctg \left\{ \frac{\left(x_m - x_D \right)\left(y_m - y_D \right)}{z_D \sqrt{\left(x_m - x_D \right)^2 + \left(y_m - y_D \right)^2 + z_D^2}} \right\} \right]$$

$$P_S\left(x_D, y_D, z_D\right)\Big|_{TOT} = \frac{K_0^2 S^2}{\pi} \frac{\cos\theta_i}{2\eta r_i^2} \iint_A \frac{\cos\left[\theta_S\left(x, y\right)\right]}{\left[r_S\left(x, y\right)\right]^2} A_{eff}\left(\theta\left(x, y\right), \phi\left(x, y\right)\right) dx dy =$$

$$= \frac{K_0^2 S^2}{\pi} \frac{\cos\theta_i}{2\eta r_i^2} \frac{\lambda^2}{4\pi} G \iint_A \frac{\cos\left[\theta_S\left(x, y\right)\right]}{\left[r_S\left(x, y\right)\right]^2} f^2\left(\theta\left(x, y\right), \phi\left(x, y\right)\right) dx dy$$

$$f^2\left(\theta\left(x, y\right), \phi\left(x, y\right)\right) \equiv 1$$

$$P_S\left(x_D, y_D, z_D\right)\Big|_{TOT} = \frac{K_0^2 S^2}{\pi} \frac{\cos\theta_i}{2\eta r_i^2} \frac{\lambda^2}{4\pi} G \cdot I\left(x_D, y_D, z_D\right)$$

2.7 Conclusions

A measurement campaign aimed at determining the scattering pattern of typical building walls has been described in this chapter. In addition, the ER diffuse scattering model [36, 37] has been modified and tuned to get the best agreement with measurements. Different shapes of the scattering pattern have been hypothesized, and for each of them a simple, parametric expression has been provided, which can be easily implemented and embedded into RT simulators. It has been shown that the "single-lobe directive model" (with the lobe steered toward the specular direction) is the best in all cases, assuming $\alpha_R = 4$ for the hangar and the brick wall, and $\alpha_R = 3$ for the rural building wall. Besides, the optimum scattering coefficient S values are of 0.05, 0.2 and 0.4 in the three considered topologies, respectively. Being the latter topology quite representative of simple, brick-wall suburban buildings, we can infer that S=0.4 is a realistic value for field prediction in suburban areas, in agreement with previous work [36-38]. In the future, further investigations must be done in order to evaluate the best scattering model for urban buildings with protruding masonry (columns, indentations, etc.) which probably originate a more significant backscattering effect even far from the specular direction. Besides, simulations in dense urban environment would probably require even greater values of S, i.e. a greater diffuse scattering contribution.

Chapter 3

Speed-up and Advanced Ray Tracing Techniques

3.1 Introduction

RT models potentially represent the most accurate methods for urban propagation characterization. Generally, such models are used in the planning phase of mobile radio systems, where they may in principle lead to great advantages in terms of deployment cost reduction and service quality increase. Nevertheless the widespread adoption of deterministic models is still quite limited due to the high complexity and high computation time of the corresponding computer programs. The high computation time is strongly dependent on the size of the input database and on the inherent inefficiency of the geometric ray-finding phase of the RT algorithm.

Some Authors have worked on speed-up methods for RT models. Among other methods, the decomposition of 3D propagation into 2D planes is proposed in [31], while the discretization of the environment and its geometric pre-processing are proposed in [96].

In this chapter, two different methods for speeding up RT prediction are proposed. The first one operates on reducing the size of the input database by selecting the "active area" of the environment and discarding the rest of the map. The second one operates on reducing the number of rays to be handled by the RT algorithm by discarding minor or low-power rays. The methods are applied on the 3D RT model described in [38], and performance in terms of CPU time reduction and accuracy of the results are shown.

3.2 Environment representation

Deterministic propagation models such as ray tracing require a proper description of the urban environment in input. Both a geometrical and an electromagnetic description of each object (building, wall, terrain) must be provided and stored in the database. A vectorial geometric representation is usually adopted, where buildings are represented as polygonal prisms with flat tops. Unfortunately the attainable accuracy of commercially available databases is necessarily limited. The standard deviation of the error in urban databases is of the order of 0.5 m for horizontal coordinates and much higher for vertical coordinates. Vertical dimensions are often unavailable or particularly subject to errors, due to deviations in rooftops from flat polygons, with an evident impact on the reliability of over-roof-top propagation prediction. Moreover, environment cluttering data (vegetation, vehicles, street signs etc.) are often unavailable or impractical to model. While reliability must be considered a very advisable quality, the "level of detail" is not necessarily so. A great level of detail (sometimes confused with "accuracy") means the presence of a great deal of building elements (internal yards, indentations, edges, roof structures, etc.) which can greatly increase the size of the database, with a more than proportional increase in the computation time of the prediction. Therefore, geometric databases must often be properly "purged" or *simplified* before they can be input to deterministic propagation models, in order to remove irrelevant details (building partitions, courtyards, chimneys, etc) and database redundancies.

In case, the effect of the details (and of other irregularities such as surface roughness, etc.) can be treated in mean, statistical way resorting to ER diffuse scattering models [36,37], with relevant saving of computing time. A very common simplification technique is the *joining* of adjacent walls or building to reduce the database size (Figure 3.1). There are also computer tools that do it automatically in a parameterized and thus controllable way. Nevertheless, *it is a very critical task, especially when buildings have different heights*.
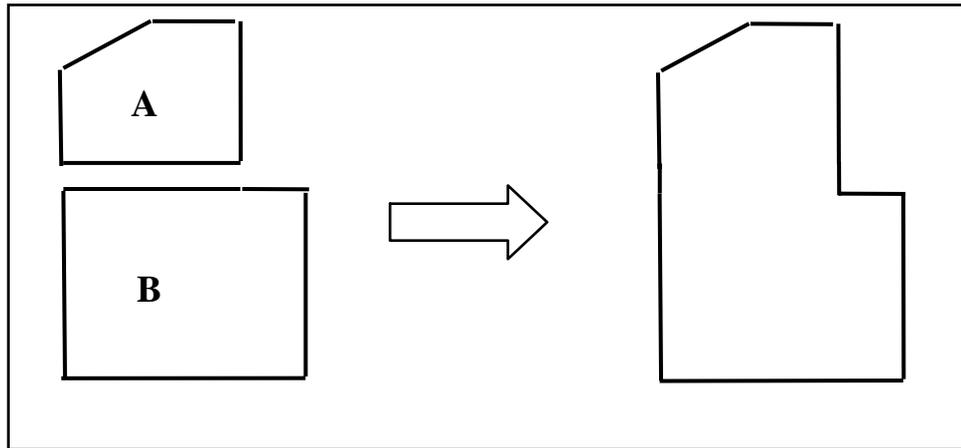
Figure 3.1 - Joining of buildings A e B (top view)

In fact, in many cases the simplified database obtained through the building method yields wrong results (see below).

For example, Figure 3.2 (a and b) show a typical simplification procedure applied to the urban layout to be fed to RT simulator: buildings B_1, B_2, B_3 and buildings B_4, B_5, B_6 in Figure 3.2.a are merged into buildings B_1 and B_2 of Figure 3.2.b, respectively.

(a)   (b)
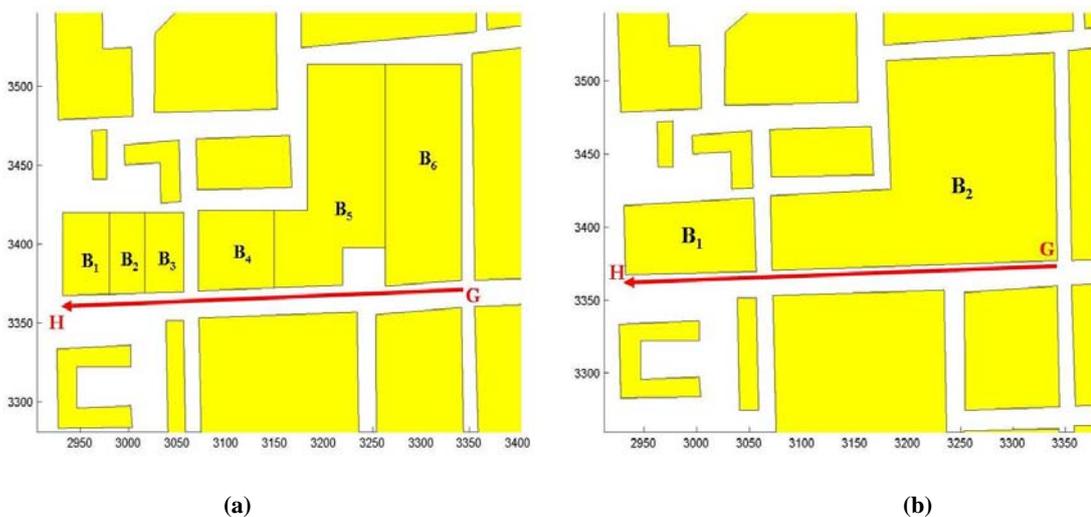
Figure 3.2 - Usual urban map simplification

In order to show the impact of this simplification method, a comparison between measurements in a macrocellular NLOS scenario located in the city center of Helsinki (route GH, see next chapter for further details) and RT simulations with detailed and simplified map is shown in Figure 3.3.

As a matter of fact, the simplified map of Figure 3.2b doesn't seem to be accurate enough to get a satisfactory prediction, and the detailed, "non merged" urban

map of Figure 3.2a has to be considered in order to achieve a fair agreement between measurements and simulation.

Hence, the merging of adjacent walls of neighbouring buildings can have an harmful impact on the accuracy of the prediction. In these cases therefore, either the map should be left "un-simplified" or walls around the receiver should be automatically divided into smaller tiles, in order to have a large number of low-power scattered rays.

By adopting the detailed map for RT simulation, Path Gain can be predicted with a greater accuracy, as shown in Figure 3.3.
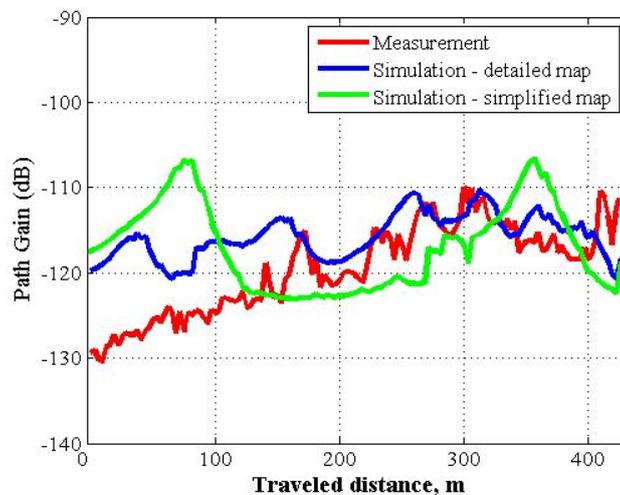
Figure 3.3 - Route GH, PG comparison

In conclusion, building joining should be done (if necessary) very carefully and in a controlled way, otherwise it can lead to wrong results.

3.3 Description of the proposed database simplification method

RT tools are usually run over a limited portion the urban area. Since computation time strongly depends on the size of the input database, it is necessary to minimize its size by selecting only the *active area* of the topology, i.e. only the buildings or obstacles that are involved in the propagation process. The proposed technique is based on the idea of running a rough, heuristic field prediction model aimed at identifying the environment elements which probably have a major impact on the propagation process. Of course this preliminary prediction must be much faster, and therefore simpler than the real prediction

model, otherwise there would be no advantage. The basic idea is that rays experiencing a single (or two) interaction(s) with building walls (often referred to as 'first (second) order rays') are likely to be more relevant than rays experiencing multiple interactions, since more interactions correspond to both a higher number of concentrated losses and a higher distributed path loss.

This property can be exploited in order to select objects which are more important in multipath propagation. Buildings *around* and *between* the radio terminals always belong to the active area, but even far, 'prominent' obstacles can have a significant impact on prediction results, especially when wideband predictions are needed [39]. In particular, recent studies [23,24,36-39] have shown that 'far' objects, including far building tops, tall buildings, hills etc., may have a significant impact on the 'tail' of the power delay profile of the radio channel, and thus on parameters such as delay spread and angle spread. Therefore, if we consider a single Tx-Rx link, an area of some square kilometers around the radio terminals, depending on link distance and Base Station (BS) height, should be considered. Such areas typically include several hundred buildings, each one composed of many perimetral walls. Therefore, a great amount of computing time can be requested from RT simulations. Even with the adoption of the speed-up techniques proposed in [94-96] computation time remains unacceptable. The problem is even more serious in large cells, with the BS at or above rooftop height, where propagation is not limited to a few streets around the BS (as in microcells), and complex 3D propagation models must be used.

Since not only buildings located 'around' the radio terminals, but also far, exposed buildings are involved in the propagation mechanism, database simplification cannot be done roughly: a scientific criterion for accurate database simplification is needed. The database simplification method presented in this chapter is based on the idea of "borrowing", anticipating "some" field prediction capabilities from a proper ray tracing approach, in order to determine the buildings involved in the multipath, instead of the multipath pattern itself (Figure 3.1). In short, building located *around* and *between* the radio terminals, or buildings easily reachable by the radio wave *from* the radio terminals ("*exposed*" buildings, buildings standing out from the urban structure) are selected by the model and stored in the simplified database. By using this model, and without the need of time-consuming and arbitrary database manipulation, the CPU time is

drastically reduced almost without degradation of both narrowband and wideband prediction results.
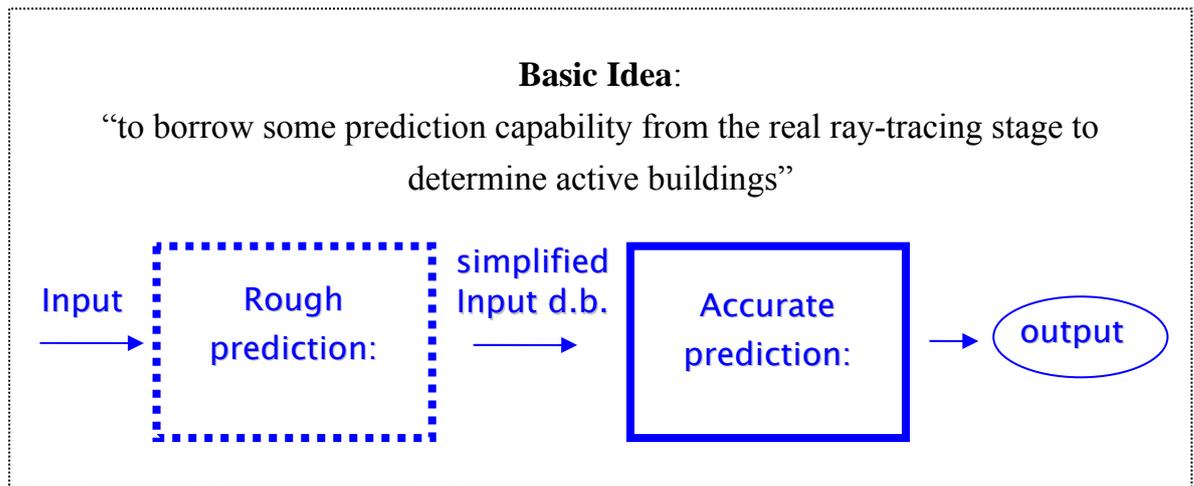
Figure 3.4 – Illustration of the simplification method (borrowing some capabilities from RT to produce a simplified database)

The proposed simplification method [] is based on the selection of the buildings belonging to three categories:

A) buildings located *around* and *between* the radio terminals (Figure 3.5)

Idea 1) To select buildings 'around' the terminals (inside ellipse)
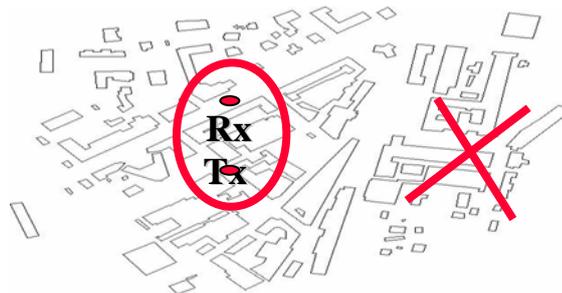
Figure 3.5 – Selection of buildings around the terminals

B) buildings which can be directly 'seen' from either the Tx, the Rx or both terminals, therefore generating first- or second- order rays (Figure 3.6)

Idea 2) To select buildings directly "visible" from Tx and/or Rx
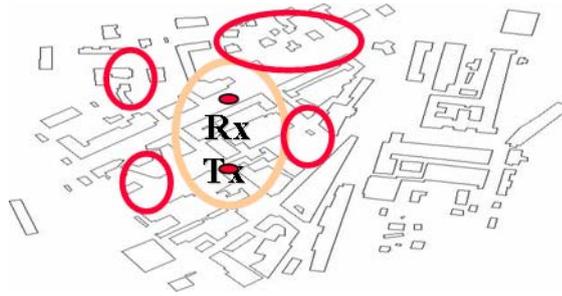
Figure 3.6 – Selection of buildings directly visibile from Tx and Rx

C) buildings not belonging to category A and B, but which are likely to have an impact on propagation because of their considerable height (greater than average) or propitious orientation, i.e. generating low-order rays ("prominent" buildings, see Figures 3.7-3.8).

Idea 3) To select other "*prominent*" buildings (…)
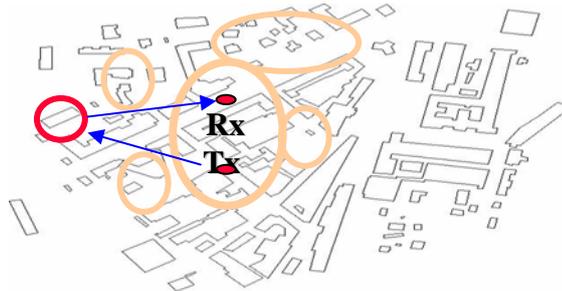
Figure 3.7 – Selection of "prominent" buildings

"*Prominent buildings*"

1) High-rise buildings (even if far)
2) Buildings above average height with the "right" orientation

Figure 3.8 – Example of prominent (far) building

Determination of class A)

All buildings located within an ellipse of focuses Tx and Rx, and of given eccentricity are selected. Of course, all buildings between the radio terminals are selected.

In addition, the lower the eccentricity, the greater the number of buildings *around* the terminals, and thus the greater the overall number of members of class A). Usually and eccentricity value is chosen so that the terminals are completely surrounded by buildings. The minimum distance δ between a focus (terminal) and the ellipse, i.e. the minimum 'thickness' of the surrounding building-band can be expressed as follows:

$$\delta = \frac{c(1-e)}{e}$$

where *e* is the eccentricity of the ellipse and *2c* is Tx-Rx distance (Figure 3.9). Notice that a building is selected if at least one vertex of the corresponding polygonal footprint falls within the ellipse area. Besides, δ must be large enough so that the terminals are fully immersed into the selected buildings.
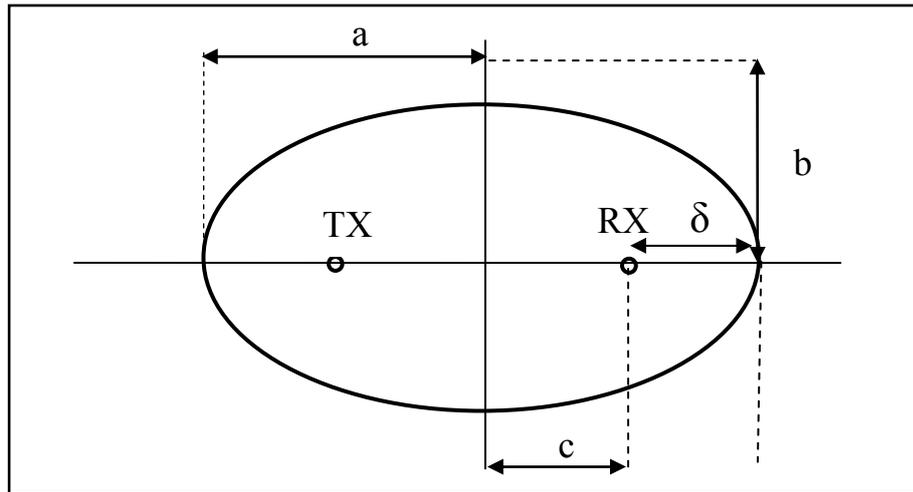
Figure 3.9 – Ellipse construction and related geometrical parameters

Determination of class B)

To identify class B), simply, first order visibility <u>from both terminals</u> is carried out. Only level 1 of the view tree is computed, therefore the procedure is very fast (Figure 3.10). The same visibility algorithm adopted in [38] is used. The algorithm is here de-embedded from the RT tool and the maximum number of interactions (N_{ev}) is set to 1. The visibility procedure is then applied to both terminals and the buildings which are visible from either the Tx, the Rx or both are recorded.
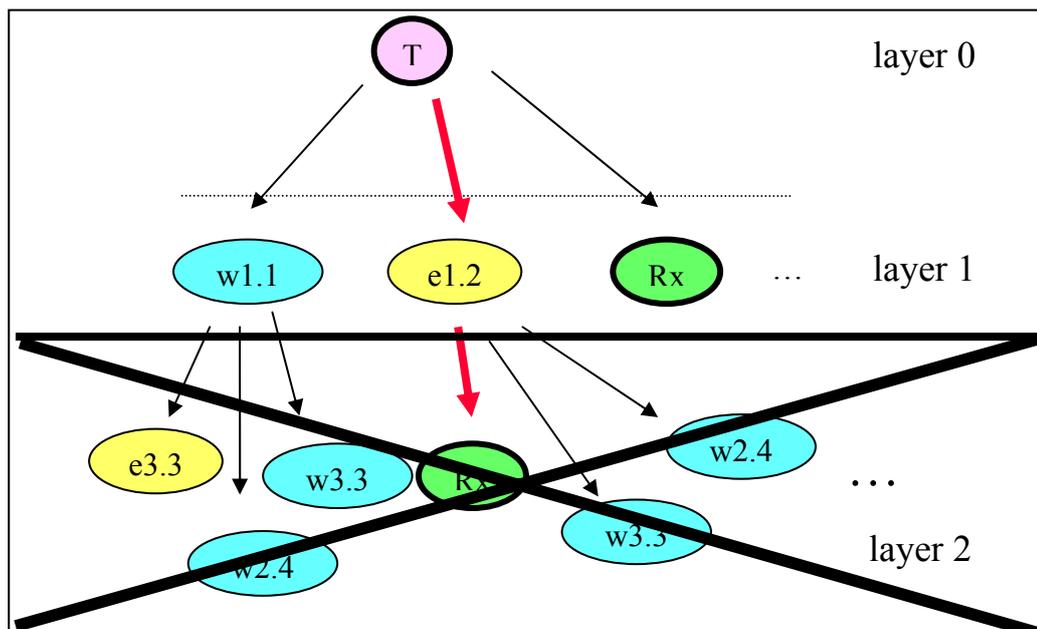
Figure 3.10 – Illustration of first order visibility

Determination of class C)

Referring to the above mentioned ellipse, its center is chosen as the origin O of a cylindrical reference system and the map is divided into angular sectors of given amplitude $\Delta\Psi$ (Figure 3.11). In this way, a *polar grid* of radial step ΔR and angular step $\Delta\Psi$ is defined (Figure 3.12).
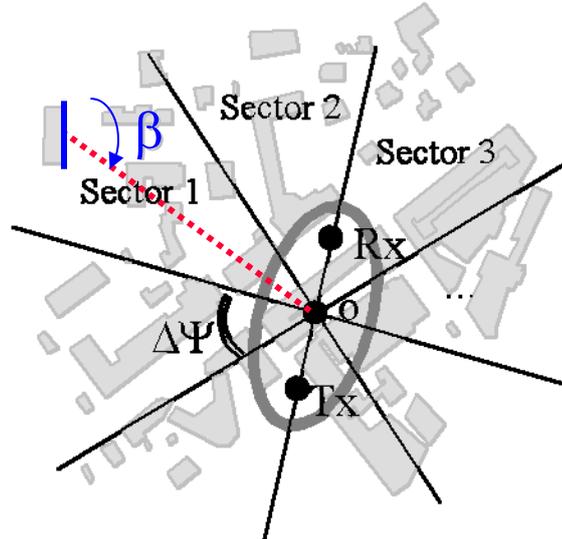
Figure 3.11 - Sectorization of the urban map for the determination of class C
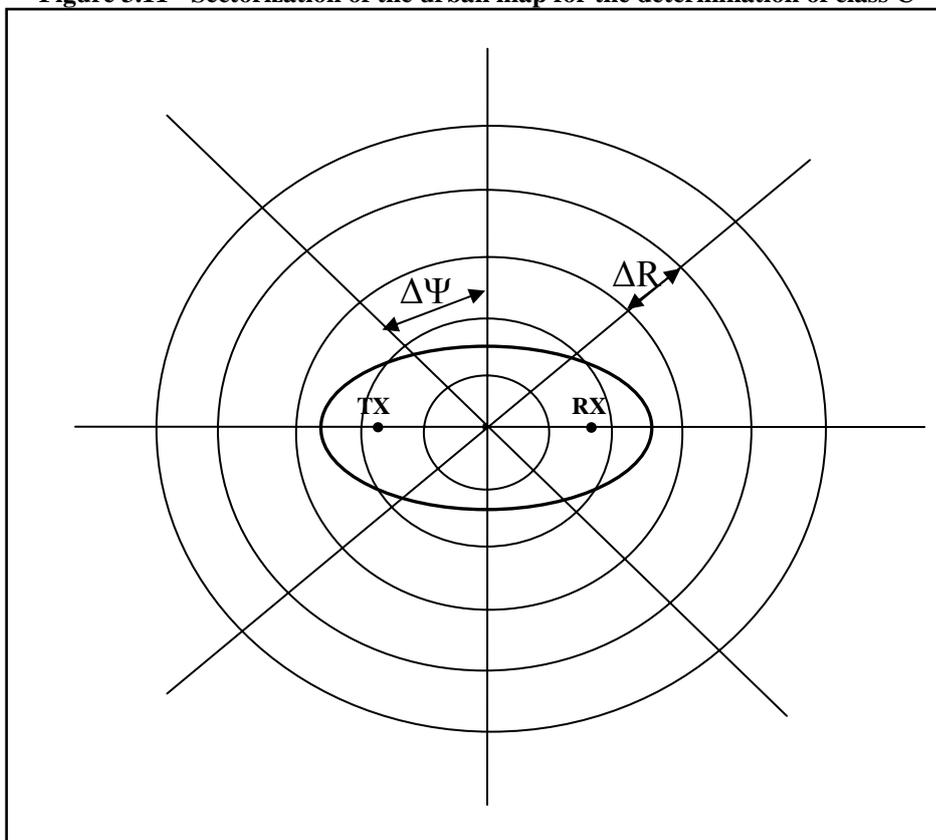
Figure 3.12 – Structure of the polar grid used in the geometrical method

Then, for each sector of the polar grid the mean value (H_b) of the building heights is computed. Describing the obstruction provided by a given sector on further buildings by means of a sort of knife-edge of height H_b placed in the center of the sector (Figure 3.13), the level of obstruction suffered by each building is evaluated by means of a simple *geometrical procedure*.
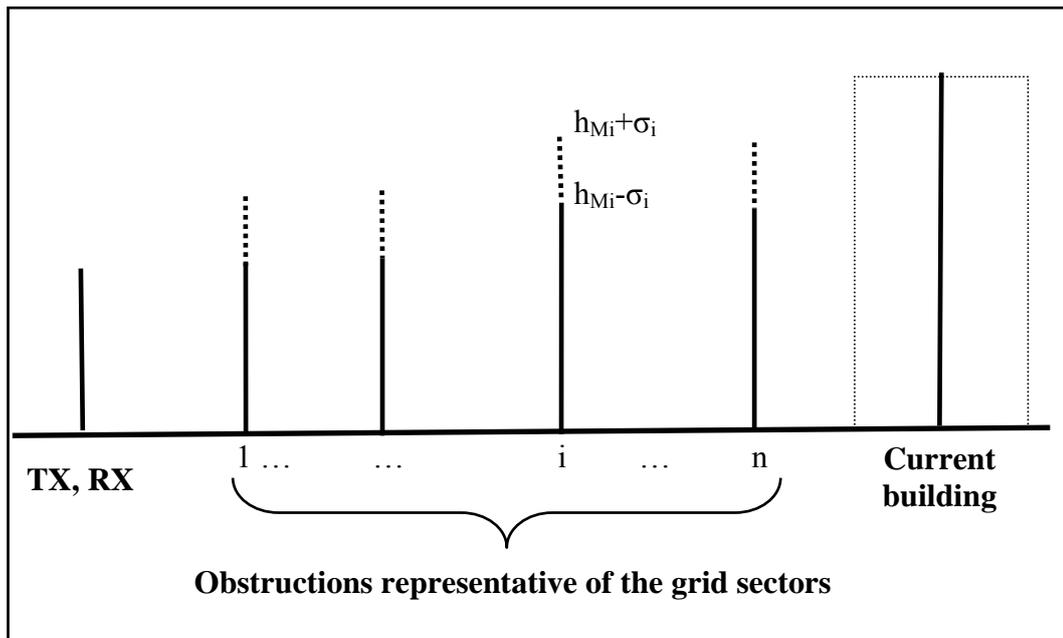
Figure 3.13 – Simplified obstruction profile used in the geometrical method

The geometrical method is based on the idea that a *prominent* building should have the following characteristics:

- it should have low attenuation ORT paths to both terminals.
- its wall(s) should have a sufficient radar cross section to cause relevant backscattering

Therefore, a **test link** is considered whose terminals are the building under test and the centre of the ellipse. The building can be regarded as important

a) If the Over Roof Top (ORT) attenuation between the two virtual terminals is below a certain threshold

b) If the Radar Cross Section (RCS) of one (or more) building walls is above a certain threshold

If the building under test is eligible in both a) and b) cases, then it's selected. Both tests are very quick compared to RT prediction. Also, they can be performed in an *approximate* way. For example:

- instead of computing the ORT attenuation, a height tolerance Δh could be set. Then, all buildings well above average height (with $H > H_b + \Delta h$) are selected (Figure 3.14), while buildings below average height ($H < H_b - \Delta h$) are discarded (Figure 3.15). Buildings of average height, i.e. with $H_b - \Delta h \leq H \leq H_b + \Delta h$ (Figure 3.16) are selected only if the criterion based on RCS (see below) is also satisfied.

- instead of computing the RCS, the ***solid angle*** Ω corresponding to the building wall as seen from the other virtual terminal and the ***orientation*** β of the wall (Figure 3.11) could be considered. If the former is sufficiently wide and the latter is *close* to zero (the wall faces the virtual terminal) then the building is eligible. In practice, buildings slightly shadowed are selected only if they have at least one wall *almost* perpendicular (within a given angular tolerance $\Delta\beta$) to the radial coordinate.
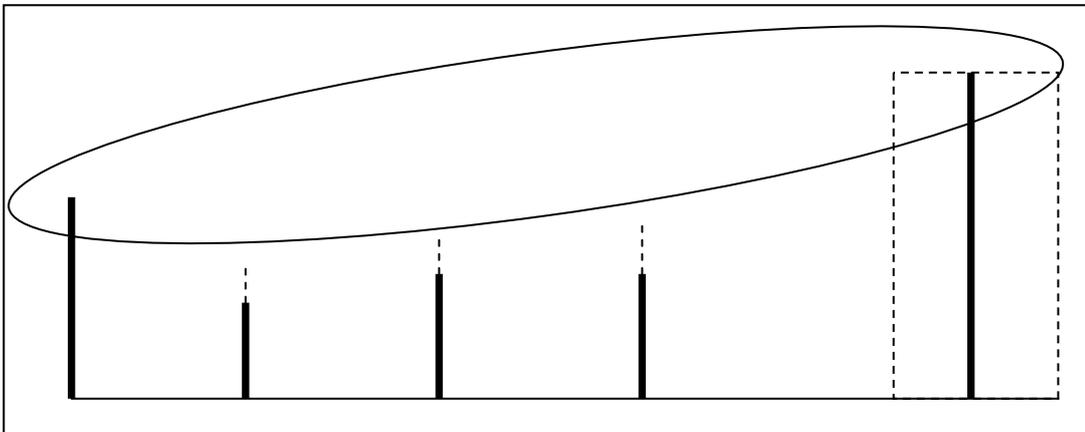
Figure 3.14 – Illustration of a building over average height (selected by geometrical method)
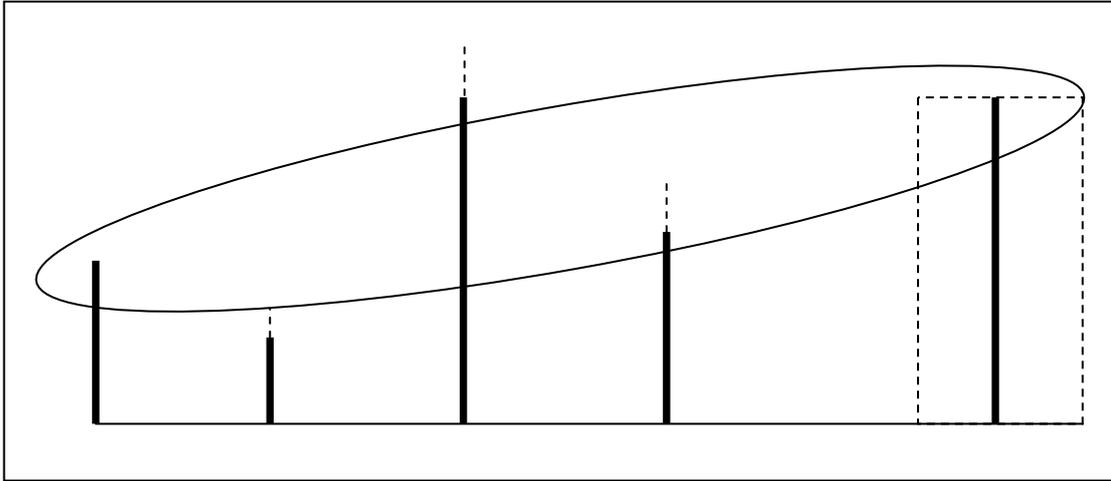
Figure 3.15 - Illustration of a building under average height (discarded by geometrical method)
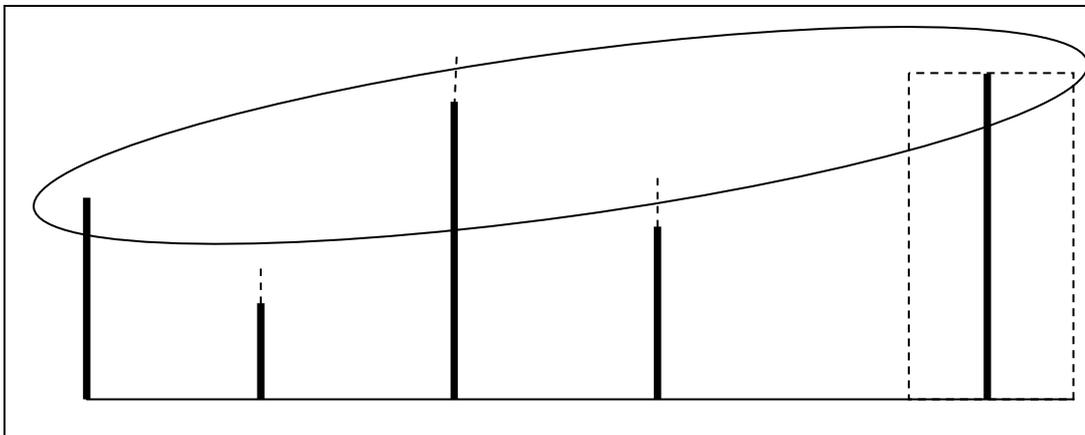
Figure 3.16 - Illustration of a building of average height (selected by geometrical method if it has the "right" orientation)

Once classes A to C are identified, the corresponding building are collected into the simplified map and duplicates discarded. If more then one Rx (Tx) is present (ex. receiver path) the whole algorithm is performed once for every Rx (Tx) and each time the new buildings are added into the simplified map. Of course if a complete prediction all over the entire urban map is to be done, the simplification algorithm will select the whole map and no CPU time gain will be possible.

The computation time of the simplification algorithm is always low, of the order of minutes even for large maps.

One drawback is that the method has many arbitrary parameters, which must be calibrated to get good results.

3.4 Other Speed-Up Techniques

3.4.1 Near/Far Techniques

As already shown, CPU time strongly depends on the number of visible walls at each view-tree computation step. But CPU time also depends on visibility processing time at each step, therefore it would be useful to simplify this task
The number of view tree nodes is approximately [55]:

$$M \approx N_V^{(N_{ev}+1)}$$

The number N_V of actually viewed walls (after accurate visibility check) depends on the number of viewed walls N_W but also on the enabled interaction types for each wall.

If all types of interactions are allowed (reflection, diffraction and diffuse scattering), 5 new Virtual TX can be added in the view tree for each visible wall: 1 reflection VTX, 1 scattering VTX, 3 diffraction VTX (vertical edges + rooftop edge). Therefore

$$N_V \approx 5 \cdot N_W$$

However, "far" walls can be treated in a simplified way: the wall, being "far" can be considered a secondary point-source, therefore only 1 VTX, located in its baricenter, is associated to it, with great reduction in view tree computation (Figure 3.17).
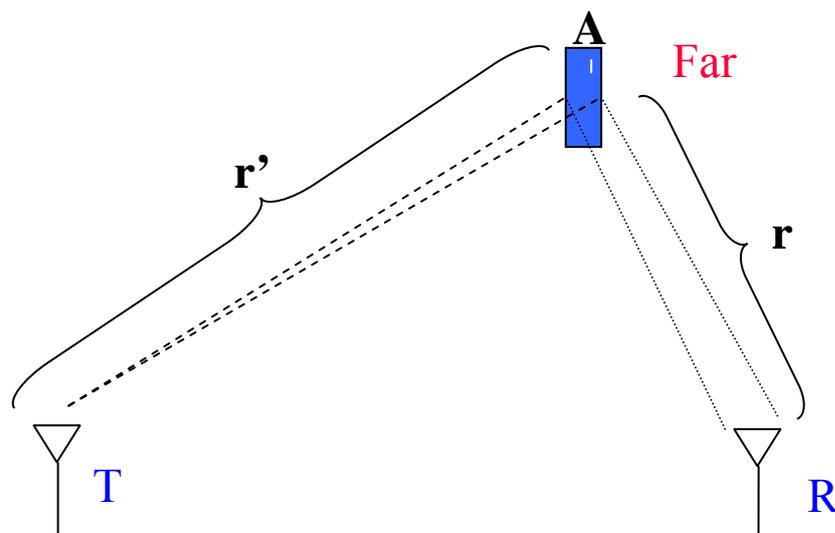
Figure 3.17 – A Far wall treated in a simplified way through RCS

From the electromagnetic point of view, far walls can be treated through the "Radar Cross Section" (RCS) theory [79]. RCS theory is applicable if:

a) The incident wave is approximately (locally) plane

b) The Rx is in the far field of the wall considered as a *secondary source*

It can be shown that conditions a) and b) are satisfied if:

$$\min\{r, r'\} > K_{FAR} \cdot \frac{D}{\lambda} \quad K_{FAR} \geq 2$$

where D is the maximum distance between all the couples of points belonging to the considered wall (Figure 3.18).
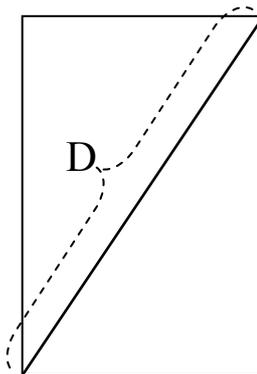
Figure 3.18 – Maximum distance between all the couples of points belonging to the wall

RCS Theory [79] allows to compute the back-scattered field from a conductive polygonal plate from a simple, closed form formulation

It is possible to extend the RCS to dielectric material plates in a heuristic way multiplying it by the Fresnel's reflection coefficient

It is also possible to extend it further to "rough" surfaces by multiplying it by the Rayleigh coefficient R and, in case, to add a diffuse scattering lobe provided that the total power balance is satisfied (see chapter 2):

$$P_i = P_{RCS} + P_{SCAT} + P_P$$

3.4.2 Tree-pruning

This speed-up technique is based on selecting dominant rays and discarding the others before they are traced by the algorithm. In fact, view tree computation is the most time-consuming part of RT: in particular, diffraction and scattering events are very time-expensive. Usually, Image RT algorithms limit the number of rays (and then the view tree computation time) by posing an upper bound to **the number of successive interactions** (N_{ev}). A low number of successive interaction, however, is not necessarily indicative of ray relevance; on the contrary, rays which experiment many interactions (for instance, multiple diffractions near the shadow boundaries) may be relevant.

Thus, the basic idea is: only the rays which carry a significant relative power must be kept, regardless of the number of successive interactions.

Unfortunately, selecting rays according to the carried power is a quite difficult task in image ray tracing algorithms. Carried power is unknown until the whole trajectory of the ray is traced, (after backtracking) i.e. when CPU time has already been spent. In particular, it is very difficult to estimate the power carried by diffracted rays when the trajectory of the ray is not completely known, because UTD coefficients exhibit significant variations depending on whether they are computed near a shadow boundary or not.

Nevertheless, even if the current ray is not completely traced, at the generic node (or Virtual TX) of the view tree some information are known:

> ➢ The "partial" divergence factor (approximately)
> ➢ The direction of departure (DOD) of the ray and then the TX antenna gain corresponding to DOD: if the TX antenna is quite directive, rays which depart far from the maximum direction may be disadvantaged w.r.t. the others.

In general, the interaction coefficients are unknown.

Therefore, we developed an approximate method to estimate an upper bound of the carried power during the compilation of the *visibility tree* [] even when the exact path of the ray is still undefined. When the estimated power of a ray falls below a minimum power threshold, the corresponding branch of the visibility tree (and all his sub-branches) is discarded, thus saving a considerable amount of CPU time.

In short, the "tree pruning" algorithm works as follows:

- First, a minimum power threshold is set, which corresponds for example to the sensitivity of the receiver.
- When a new object is seen, and then a new node of the tree must be created, a ray is traced joining the last node and the nearest Rx, as if it was visible from the last Virtual TX.
- An approximated estimate of the field at the Rx is computed, adopting a conservative (pessimistic) criterion for the interactions coefficients, which are unknown: coefficients of perfectly electric conductor (PEC) are assumed, while UTD coefficients on the shadow boundaries are assumed for diffraction.
- If the power carried by the ray exceeds the threshold, the considered node is inserted in the view tree; otherwise, it is discarded.

Since the number of the branches on the visibility tree grows exponentially with the number of interactions, the advantage of the proposed method w.r.t. a standard selection method increases with the number of maximum allowed interactions. However, as shown in the text below, even in simulations with a limited number of interactions (2,3) the advantage in terms of computation time is considerable.

In figure 3.18 the CPU time of RT simulations with a variable total number of buildings is shown, obtained respectively by a classical RT, by a RT enhanced with the near/far techniques, and by a RT enhanced with both near/far and tree-pruning techniques. In all cases, CPU time grows linearly with the number of buildings. Nevertheless, the slope is drastically reduced with near/far techniques (pink curve), with respect to traditional RT (green curve). Finally, using "tree pruning" in addition to near/far techniques (blue curve), the slope is further reduced. This further savings would be greater with a greater N_{ev}

CPU time (s)
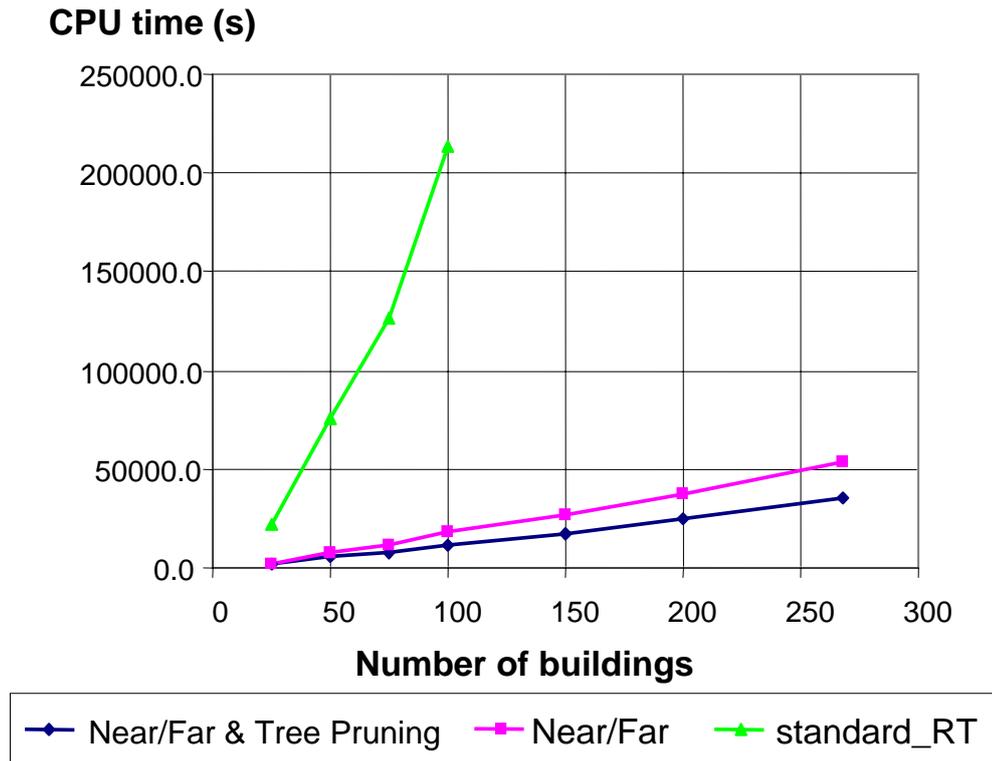
Figure 3.18 – Comparison between classical RT and RT enhanced with the proposed speed-up techniques

3.5 Results

Comparison between 'complete' simulations (i.e. without any speed-up procedure) and 'quick' simulations (i.e. after map simplification and/or applying dominant rays selection) have been carried out in several macrocellular urban scenarios. A satisfactory time reduction with a good agreement both in term of narrowband and wideband results has been achieved in most cases.

An example of map simplification which refers to a simulated route of 175 Rx locations in the central part of the city of Helsinki is shown in Figure 1. It is evident that the simplified map could not be simply "guessed".

Results in term of CPU time and Delay Spread (DS) prediction are summarised in Table 1. Ray tracing has been run with a number of interactions $N_{ev} = 3$. It is evident that despite the critical nature of the macrocellular topology, the resulting DS does not show any sensible change in any case. On the contrary, the CPU time can be reduced by a factor of almost 7 by applying both speed-up techniques.
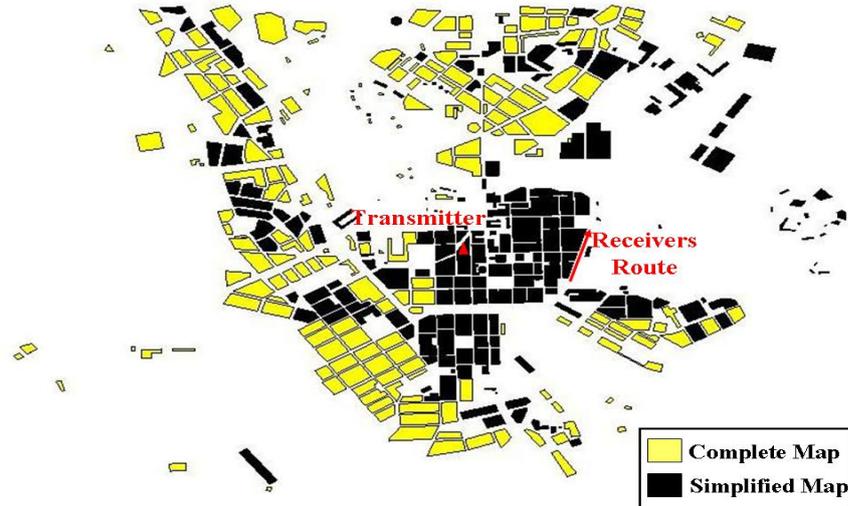
Figure 3.19 – Complete (yellow) and reduced (black) map of central Helsinki

	CPU time	Mean DS (μsec)	Mean Error on DS (w.r.t. CS)
Complete Simulation (CS)	**2299 min**	**1.11**	**---**
Map Simplification (MS)	**732 min**	**1.11**	**0.56 nsec**
Ray Selection (RS)	**1099 min**	**1.11**	**-0.0049 nsec**
MS and RS	**356 min**	**1.11**	**0.53 nsec**

Table 1 – CPU time and wideband results with a complete simulation, and with different speed-up methods combinations

3.6 Conclusions

In this chapter, two different methods for speeding up RT prediction are proposed. The first one operates on reducing the size of the input database by selecting the "active area" of the environment in terms of impact on the multipath propagation process. The second one operates on reducing the number of rays to be handled by the RT algorithm by discarding minor or low-power rays. Results in terms of CPU time reduction and accuracy of the results show that the

proposed speed-up method can reduce CPU time by a factor of almost 7 virtually without any degradation of wideband results. Moreover, CPU time reduction is expected to be much greater in microcellular cases or when the number of events is high (e.g. N_{ev} = 4 or 5).

Chapter 4

Multidimensional Characterization of the Radio Channel

4.1 Introduction

In this chapter, a multidimensional analysis of urban propagation is carried out using both experimental results and ray tracing simulations. Ray tracing (RT) is used here not only to get predictions to be compared with measurements, but also as a mean to interpret and analyse measurement results. In fact, ray tracing does not only represent a computer algorithm, but also the only possible implementation of a theoretical model for multipath propagation in urban areas. Therefore, by simulating the real propagation phenomenon with a ray tracing model, it is possible to deeply understand the multipath pattern, track the main propagation paths, determine how our idealization fits reality, and eventually adjust the parameters or identify new interaction models in order to get a better agreement with measurements, and therefore a better knowledge of propagation in real environments.

The employed measurement setup is described in section 4.4. Since some urban propagation aspects, such as diffuse scattering, must be regarded as "non-deterministic" phenomena, a statistically significant amount of experimental data is required to perform a thorough characterization. Furthermore, information on the 3D angular and temporal distribution of the signals is useful to separate and analyze the different paths, or the different clusters of paths.

Computer simulations have been performed with the advanced 3D RT tool described in [38]. Diffuse scattering has been modeled adopting the *Effective*

Roughness (ER) approach described in [36, 37, 42]. The simulation parameters are briefly discussed is paragraph 4.5.

Comparison results show that by introducing diffuse scattering into the RT model a good agreement between simulation and measurement can be obtained, especially if power-delay profiles or power-directions of arrival (DOA) profiles are considered. Moreover, RT with scattering converges more rapidly than traditional RT even with a low order of events (successive reflections/ diffractions/scatterings), thus sensibly reducing CPU time. Results are then interpreted and discussed in section paragraph 4.6. Conclusions are drawn in paragraph 4.7.

4.2 The meaning of multidimensional characterization

Since all rays at Rx are characterized individually in terms of their amplitude, phase, delay, direction of departure (DOD), and direction of arrival (DOA), ray tracing (RT) allows a complete characterization of propagation [56].
In practice, using a RT program we have in output for the i-th ray:

$\vec{E}^i$ incident field on Rx antenna

a_i amplitude of the Rx signal (current or voltage)

θ_i phase of the Rx signal (current or voltage)

τ_i delay (absolute or relative)

ν_i Doppler frequency (if mobile terminal velocity is known)

$\vec{\Omega}_T$ Direction Of Departure (or departure angle(s) (θ_T, ϕ_T))

$\vec{\Omega}_R$ Direction Of Arrival (or arrival angle(s) (θ_R,ϕ_R))

By means of such information, and taking into account the radiation patterns and polarization properties of the Tx and Rx antennas, it is straightforward to get the total coherent power at the Rx (for a fixed transmitted power), or the path loss between Tx and Rx, i.e. the classical *narrowband characterization* of the channel.
Assuming perfect impedance matching at the receiver, the total received power can be expressed as

$$P_R = \frac{\lambda^2}{8\pi\eta} \cdot G_R \cdot \left| \sum_{i=1}^{N_r} \left(f_R\left(\theta_R^i, \phi_R^i\right) \cdot \left\{ \hat{p}_R\left(\theta_R^i, \phi_R^i\right) \bullet \vec{E}^i \right\} \right) \right|^2 \quad (4.1)$$

where N_r is the total number of rays, G_R the Rx antenna gain, f_R the Rx antenna radiation function, $\left(\theta_R^i, \phi_R^i\right)$ are the angles of arrival of the i-th ray, η is the intrinsic impedance of the medium, λ the wavelength and $\hat{p}_R$ the Rx antenna polarization vector. For example, assuming a 2-ray model (i.e. direct ray and ground reflection) and supposing perfect polarization matching between the incident field and the RX antenna, eq. (5.1) becomes [80]:

$$P_R = \frac{1}{2\eta} \cdot G_R \cdot \left| \vec{E}_1 f_R\left(\theta_1, \phi_1\right) + \vec{E}_2 f_R\left(\theta_2, \phi_2\right) \right|^2 \cdot \frac{\lambda^2}{4\pi}$$

If only the direct path exists and the polarization matching is still satisfied, recalling that $g_R\left(\theta, \phi\right) = G_R \cdot f_R^2\left(\theta, \phi\right)$, eq. (5.1) reduces to the well known free-space formula:

$$P_R = \frac{\left|\vec{E}\right|^2}{2\eta} \cdot \frac{\lambda^2}{4\pi} g_R\left(\theta_R, \phi_R\right) = \frac{\left|\vec{E}\right|^2}{2\eta} \cdot A_{eff}\left(\theta_R, \phi_R\right)$$

In many case of common practice, a narrowband characterization is not sufficient, because the time dispersion properties of the channel can heavily impact on system design, and so the channel impulse response (or the transfer function) of the channel is needed. This is the classical *wideband characterization* of the channel, which can be derived from a RT tool in a straightforward way.

For example, for a static channel we have:

$$h(\tau) = \sum_{i=1}^{N_r} a_i \, \delta\left(\tau - \tau_i\right) \implies p(\tau) = \frac{\sum_{i=1}^{N_r} a_i^2 \, \delta\left(\tau - \tau_i\right)}{\sum_{i=1}^{N_r} a_i^2} \quad \text{(power-delay profile) (4.2)}$$

And with a similar procedure, for a time-variant channel we can get:

$$p_D(\nu) = \frac{\sum_{i=1}^{N_r} a_i^2 \, \delta\left(\nu - \nu_i\right)}{\sum_{i=1}^{N_r} a_i^2} \quad \text{(power-Doppler profile) (4.3)}$$

These profiles can be averaged to get estimates of the corresponding statistical functions. However, usually some synthetic parameters, such as *deterministic versions of Delay Spread and Doppler Spread* are directly derived from the power-delay and power-Doppler profiles, thus getting:

$$DS = \sigma_\tau = \sqrt{\sum_{i=1}^{N_r} \left(\tau_i - \overline{\tau}\right)^2 \cdot p_i} \quad \text{(Delay spread)} \quad (4.4)$$

where

$$\overline{\tau} = \sum_{i=1}^{N_r} \tau_i \cdot p_i \qquad \text{and} \qquad p_i = \frac{a_i^2}{P_{TOT}} = \frac{a_i^2}{\sum_{k=1}^{N_r} a_k^2}$$

and, similarly:

$$W = \sigma_v = \sqrt{\sum_{i=1}^{N_r} \left(v_k - \overline{v}\right)^2 \cdot p_i} \quad \text{(Doppler spread)} \quad (4.5)$$

where

$$\overline{v} = \sum_{i=1}^{N_r} v_i \cdot p_i$$

Of course, other wideband synthetic parameters, such as *coherence bandwidth* and *coherence time*, can be easily obtained in a similar way.

With respect to classical wideband characterization in delay-doppler domains, other parameters can be introduced which refer to space instead of excess delay or doppler frequency. Thus a so called ***multidimensional characterization of the mobile radio channel*** can be achieved, in a statistical (through statistical/average functions) or deterministic way (through measured or simulated data).

For example, we can define a *power-delay-azimuth (of arrival) profile* [56]:

$$p_{\tau,\phi}\left(\tau,\phi\right) = \sum_{i=1}^{N} p_i \, \delta\left(\tau - \tau^i\right) \delta\left(\phi - \phi_R^i\right) \quad (4.6)$$

and the corresponding *azimuth spread*, which synthetically describes the angular dispersion on the horizontal plane:

$$AS = \sigma_\phi = \sqrt{\sum_{i=1}^{N} p_i \cdot \left(\phi_i - \overline{\phi}\right)^2} \quad (4.7)$$

A characterization of the angular dispersion on the vertical plane can be obtained likewise, through the elevation angles θ_R^i.

Nevertheless, since propagation is 3D, the azimuth spread defined in formula (4.7), and the corresponding elevation spread, do not provide a comprehensive characterization of the angular dispersion of the channel. Moreover, it can be shown that the values of azimuth spread obtained through (4.7) depend on the reference system used for the angles (i.e. on the direction where the azimuth is assumed to be zero). Usually, the reference axis should be chosen in the dominant path direction, but this is rather a common sense assumption than a precise rule, so different choices of the reference system may lead to conflicting results (for example, in comparisons between measurements and simulations…).

To get out of this trouble, in [56] a new parameter, called *Direction of Arrival Spread*, or *Angle Spread*, is introduced.

In fact, each direction of arrival can be represented by a unit vector

$$\hat{\Omega}_i = \hat{\Omega}_i(\theta_i, \phi_i) = \left[\cos(\phi_i)\sin(\theta_i), \sin(\phi_i)\sin(\theta_i), \cos(\theta_i)\right]^T \quad (4.8)$$

The initial point of $\hat{\Omega}$ is anchored at the reference location O, while the terminal point is located on a sphere of unit radius centred on O (Figure 4.1):
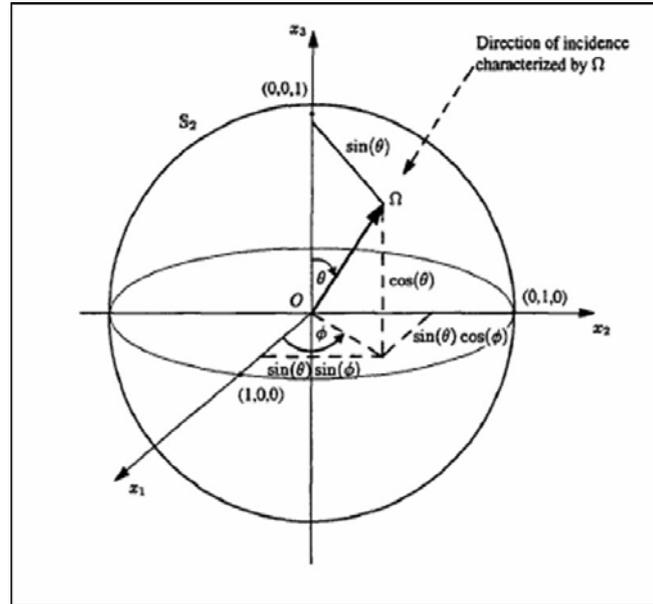
Figure 4.1 – Characterization of an incidence direction

The *Direction of Arrival Spread* is then defined as the second moment of the unit vector $\vec{\Omega}_i$:

$$DOAS = \sigma_{\hat{\Omega}} = \sqrt{\sum_{i=1}^{N}\left|\vec{\Omega}_i - \left\langle\vec{\Omega}\right\rangle\right|^2} = \sqrt{\left\langle\left|\vec{\Omega}_i\right|^2\right\rangle - \left|\left\langle\vec{\Omega}\right\rangle\right|^2} = \sqrt{1 - \left|\left\langle\vec{\Omega}\right\rangle\right|^2} \quad (4.9)$$

where the last equal results from $|\vec{\Omega}_i|=1$, and $\langle\vec{\Omega}\rangle$ is the *Mean Direction Of Arrival*:

$$\langle\vec{\Omega}\rangle = \frac{\sum_{i=1}^{N_r} a_i^2 \vec{\Omega}_i}{\sum_{k=1}^{N_r} a_k^2} \quad (4.10)$$

It is worth noticing that (4.9) does not depend on the choice of the reference system, but $\langle\vec{\Omega}\rangle$ and $\sigma_{\bar{\Omega}}$ are dimensionless quantities and so they are not angles (even if they are related to angles…). Nevertheless, in most of the literature σ_ϕ is used, which is an angle, (usually expressed in degrees). In order to allow direct comparison with the literature, the following definition of Angle Spread (3D), expressed in degrees, has been proposed [56], which is DOAS multiplied by $180/\pi$:

$$AS' = \frac{180}{\pi}\sigma_{\bar{\Omega}} = \frac{180}{\pi}\sqrt{1-\left|\langle\vec{\Omega}\rangle\right|^2} \quad (4.11)$$

According to the previous formula, the maximum value of 3D Angle Spread corresponds to $\langle\vec{\Omega}\rangle=0$, i.e. $AS' = 180/\pi \approx 57.3^{\mathrm{O}}$.

Sometimes, a "2D version" of the formula (4.11) can be useful (i.e. when horizontal propagation is prevalent):

$$AS'' = \frac{180}{\pi}\sigma_{\bar{\Omega}_{2D}} = \frac{180}{\pi}\sqrt{1-\left|\langle\vec{\Omega}_{2D}\rangle\right|^2} \quad (4.12)$$

when $\vec{\Omega}_{i\_2D}$ is a unit vector obtained projecting $\vec{\Omega}_i$ on the azimuthal plane.

The last formula provides a definition of *Azimuth Spread* which is independent from the reference system, w.r.t. the traditional definition (σ_ϕ).

In brief, all has been said in the text above about characterization of the radio channel can be summarized in the following way:

- Radio propagation characterization in terms of coverage, path-loss, path-gain or received power is usually called ***narrowband characterization***

- Radio propagation characterization in terms of power-delay profile, delay spread, power-Doppler profile, Doppler spread, Coherence bandwidth or

Coherence time, frequency response, etc. is usually called ***wideband characterization***

- Radio propagation characterization in terms of all of the previous parameters and also in terms of spatial parameters (angle of arrival/emission, power-angle profiles, angle spread, etc.) is called ***multidimensional characterization***

- In short: *multidimensional characterization is the characterization of multipath propagation with respect to all domain dimensions: amplitude, time, frequency, Doppler frequency, space*

4.3 Application of Ray Tracing to MIMO channel characterization

In chapters 2 and 3, we have seen how the 3D Ray Tracing model described in [38] has been modified to include a diffuse scattering models based on the "Effective Roughness" (ER) approach [36,37] and to improve its speed and complex database handling capability. Diffuse scattering has been shown in chapter 2 to be of crucial importance to obtain a realistic representation of the multipath pattern, which is essential in MIMO modelling. The RT model has also been modified in order to allow a coherent computation of the field, which is necessary for MIMO channel characterization; in addition, the capability of reproducing accurate 3D descriptions of the radiation patterns and polarization properties of the antennas has been improved (see Appendix C for further details), which is of fundamental importance for the study of MIMO systems employing angle/polarization diversity techniques. Therefore, the electric field corresponding to each radio path (ray) is represented by a 3D complex vector $\mathbf{E}$, with associated propagation time delay τ, angles of departure (θ_T, ϕ_T) and angles of arrival (θ_R, ϕ_R).

Considering all the paths between the two radio terminals and the corresponding received field vectors, propagation delays and angles of arrival/departure, a multidimensional characterization of the radio channel (delay/angle distributions, generalized spread function etc.) can be obtained in a straightforward way. Besides, an antenna-dependent MIMO channel matrix

formulation can be derived from the RT output through the simple post-processing method described below.

Assuming perfect impedance matching at both transmitter (Tx) and receiver (Rx) sides, the electric field radiated in the departure direction (θ_T, ϕ_T) of the generic ray by the i-th antenna of a transmitting array located in the origin of a local spherical coordinate system can be written as:

$$\vec{E}_T^i\left(r,\theta_T,\phi_T\right) = I_T^i \cdot \sqrt{\frac{Z_T^i \cdot \eta \cdot G_T^i\left(\theta_T,\phi_T\right)}{16\pi}} \cdot \frac{e^{-j\beta r}}{r} \cdot \hat{p}_T^i\left(\theta_T,\phi_T\right) = \vec{E}_{T0}^i\left(I_T^i\right) \cdot \frac{e^{-j\beta r}}{r} \quad (4.13)$$

where Z_T is the impedance of the antenna, I_T is the current phasor feeding the antenna, G_T the antenna gain function, η is the intrinsic impedance of the medium, $\beta = 2\pi/\lambda$ is the wave number and $\hat{p}_T$ is the antenna polarization vector (the apex "i" refers to the i-th element of the transmitting array). The initial phase of the field can be included in $\hat{p}_T$ without loss of generality.

The radiated field at 1 m distance from the i-th Tx element $\vec{E}_{T0}^i\left(I_T^i\right)$ is then multiplied in the RT algorithm by the proper divergence factor and reflection/diffraction/scattering coefficients to account for propagation losses and phase shift along the ray path, and the field $\vec{E}_R^{i,j,k}$ of the k-th ray transmitted by the i-th element of the transmitting array and received by the j-th element of the receiving array can be obtained:

$$\vec{E}_R^{i,j,k}\left(I_T^i\right) = \left[\prod_{\ell=\min\{1,N_{EV}^k\}}^{N_{EV}^k} \underline{\underline{\mathbf{D}}}_\ell\right] \cdot \vec{E}_{T0}^i\left(I_T^i\right) \cdot e^{-j\beta s_\ell} \cdot \Gamma_k\left(s_\ell, \ell = 0,1,2,...,N_{EV}^k\right) \quad (4.14)$$

where N_{EV}^k is the number of "bounces" experienced by the k-th ray, s_ℓ is the length of the ℓ-th segment composing the k-th path, Γ_k is the divergence factor, $e^{-j\beta s_\ell}$ is the phase factor, and $\underline{\underline{\mathbf{D}}}_\ell$ is an appropriate dyadic to decompose the field into orthogonal components at the ℓ-th interaction point.

Then, the current phasor induced in the j-th element of the receiving array by the k-th ray coming from the i-th element of the transmitting array can be computed as [78]:

$$I_R^{i,j,k}\left(I_T^i\right) = -j\lambda \cdot \sqrt{\frac{G_R^j\left(\theta_R,\phi_R\right)}{\pi\eta \cdot \Re e\left(Z_R^j\right)}} \cdot \hat{p}_R^j\left(\theta_R,\phi_R\right) \cdot \vec{E}_R^{i,j,k}\left(I_T^i\right) \quad (4.15)$$

where the subscript "R" refers to the Rx antenna and the apex "j" refers to the j-th element of the receiving array. (θ_R, ϕ_R) are the arrival angles of the considered ray in the Rx-based local coordinate system.

Notice that I_T^i appears in (4.15) simply as a multiplying factor. The total output current at the j-th receiving antenna due to the N_r contribution coming from the i-th transmitting antenna can therefore be computed:

$$I_R^{i,j} = \sum_{k=1}^{N_r} I_R^{i,j,k} = \sum_{k=1}^{N_r} \xi^{i,j,k} \cdot I_T^i = h_{ij} \cdot I_T^i \quad (4.16)$$

A deterministic estimate of the MIMO channel matrix $\mathbf{H} = [h_{ij}]$ is thus obtained. On the base of the channel matrix $\mathbf{H}$, theoretical channel capacity estimates have been derived in a reference scenario representative of a number of typical urban environments.
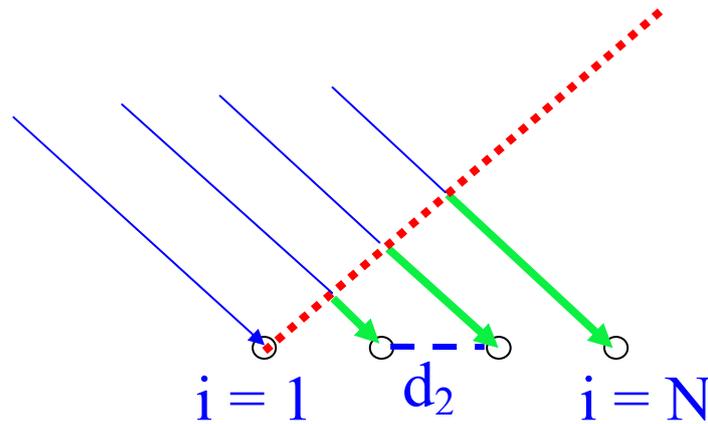
Figure 4.2 – The narrowband assumption: the generic wave impinges on all array elements, producing the same signal except for a phase difference depending on the angle of arrival

The multipath pattern is the same for all array elements, only the phase of each ray is different

4.4 Measurement Setup and Data Processing

The measurement results utilized in this work were gathered in the city center of Helsinki, Finland. Two scenarios have been considered. The first one corresponds to a typical BS antenna installations in small macrocellular radio

network configuration (i.e., BS_1), while the second is of microcell type (BS_2). The mobile station traveled along measurement routes (see Figure 4.3) that correspond to the small cell scenario (routes GH and EF), and to the microcell scenario (route NO), respectively. The BS_1 was placed at height of about 3 m above the rooftop of a parking house as shown in Figure 4.4 pointing to the East; BS_2 (route NO) was pointed towards the West and placed below the rooftop at a height of about 13 m. The transmitter antenna used at the base station was a modified GSM1800 base station antenna. The 6-dB beamwidth of the transmitter antenna is 120° in horizontal and 40° in vertical plane. The gain was 10 dBi. The radiation patterns on both E and H planes are shown in Figure 4.5. The transmitter power was 40 dBm. The code length was 255 chips for small cell scenario and 127 chips for the microcell scenario. The receiver side was a spherical antenna array with 32 dual-polarized patch antennas (see Figure 4.6) with element maximum gain of 8 dBi and the height of the array w.r.t. the ground was 1.65 m. In the transmitter of the sounder, a cyclic pseudo-noise sequence (m-sequence) modulates the carrier at 2.154 GHz. The chip frequency of the m-sequence was 30 MHz in all measurements leading to a delay resolution of about 33 ns. In the receiver, the demodulated signal is divided into I- and Q-branches. The signal samples from each branch of the RF switch are then stored for off-line processing to compute the temporal and spatial information.

At the base station (BS), the signal was transmitted using a single fixed vertically polarized antenna. At the mobile station (MS), the signal was received separately from the θ- and ϕ-polarized feeds of each of the 32 elements of the spherical array using a fast 64-channel RF switch. The measurement is very fast and enables the acquisition of large amounts of data along continuous measurement routes. The spherical array was placed on a trolley and approximately five snapshots of the received signal were sampled and stored per each wavelength the mobile moved. We measured the impulse responses separately for θ- and ϕ-polarized components of the incident field at the mobile station spherical antenna. The impulse responses of the spherical array were processed offline to estimate the multipath channel parameters. The delays, directions-of-arrival, amplitudes, and phases of both θ- and ϕ-polarized components of the incoming waves at each measurement snapshot were estimated through sequential delay-domain and angular-domain processing. The delay taps were identified by detecting the local maxima of the impulse response averaged over the array elements. Corresponding to each delay tap, there may exist one multipath

component or several components separated by their DOAs. Up to four multipath components per delay tap were estimated using the beamforming scheme with pre-computed array weights (2° beam spacing in azimuth and elevation), as described in [2]. At most four beams with powers exceeding -6 dB from the highest beam were accepted. The amplitudes and phases of the θ- and φ-polarized components of the incident waves were obtained by pointing θ- and φ-polarized beams in these directions.
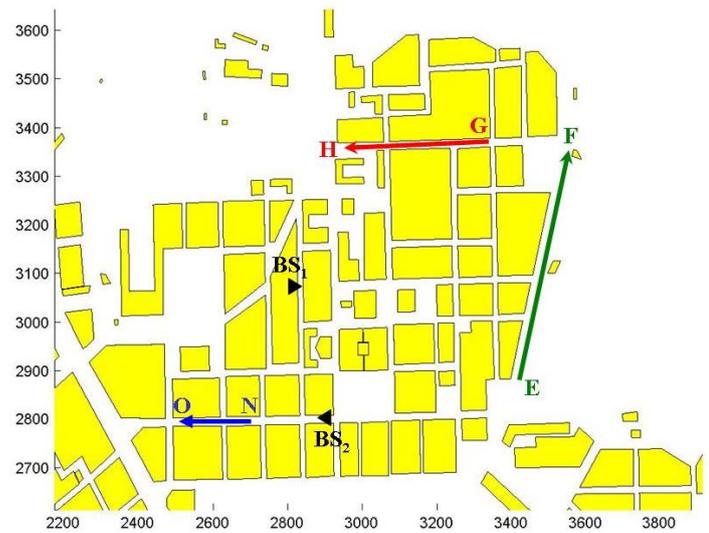
Figure 4.3 - Helsinki urban map and measurement routes

Figure 4.4 - Base station (BS$_1$) antenna was located at the rooftop of parking house.
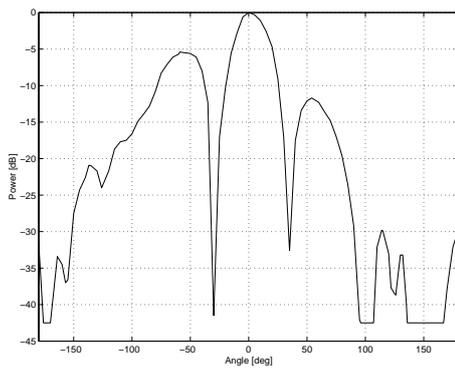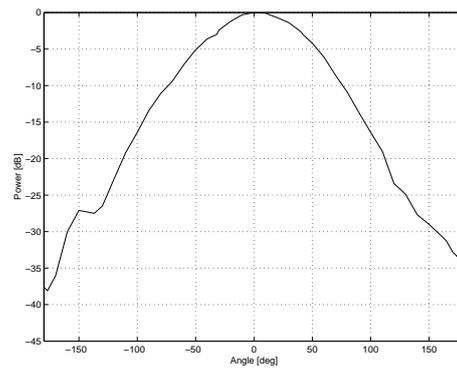
a) E-plane   b) H-plane

Figure 4.5 – 2D radiation patterns of the modified base station antenna ($f = 2.154$ GHz).

Figure 4.6 - Receiver spherical antenna array.

4.5 The prediction model

The adopted propagation prediction tool is based on an Image Ray Tracing technique [38]. A full 3D approach is adopted in order to obtain a reliable description of diffuse scattering from far buildings, which could not be achieved with a 2D or 2D and-a-half approach. The implemented Ray Tracing Algorithm consists of two main steps: the creation of the *visibility tree* and the *backtracking procedure*. Once the rays are tracked, each path is associated its field strength, depending on the undergone interactions with the propagation environment. In particular reflection and diffraction are treated according the GO and the UTD approach respectively, whereas diffuse scattering is simulated according to the Effective Roughness approach [36,37,42], transmission is neglected at this stage of the work.

The following values of electrical permittivity and conductivity for building walls have been used here: ε_r=5, σ=1x10^{-2} S/m, which are recognized as the most appropriate in European cities. In the present work, the value of the scattering parameter S, used according to the effective roughness approach [37], must be input to the ray tracing solver. The value S=0.4, which has been proved to well reproduce the scattering behaviour of typical urban buildings [36, 37], has been used for all building walls.

4.6 Results

Measurement and simulations results achieved for the considered receiving routes are shown in the following sub-paragraphs 4.6.1 to 4.6.3. It is worth noticing that according to the scattering model embedded into the RT simulator [36, 37], scattered rays are not requested to comply with strict geometrical constraints such as the diffracted and reflected contributions (which must obviously satisfy reflection and Keller's laws, respectively). Therefore, a large amount of rays, adequate enough for reliable prediction, can be achieved with a low number of maximum allowed "bounces" for each ray (N_{ev}). In particular, the results shown in the following have been obtained with $N_{ev}=3$.

4.6.1 Route EF
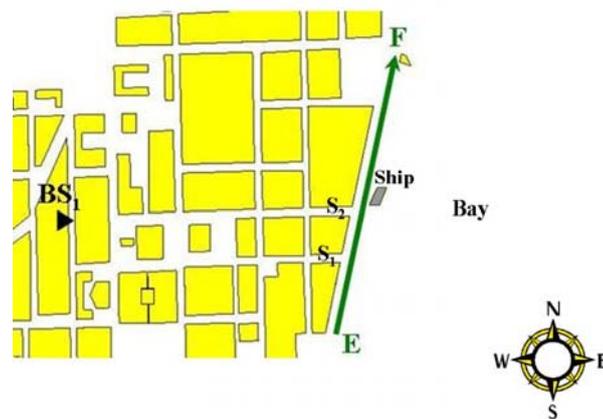
Figure 4.7 - Route EF

A close-up of the urban area around route EF is reported in Figure 4.7. Figure 4.8 shows the measurement – simulation comparison in terms of path gain (PG). Path gain is defined as the inverse of the path loss, including a proper scale factor due to the numerical post processing procedure of the data measured with the spherical array antenna set-up. It is evident that a small central section of the route (corresponding to the intersection with the street in front of the BS) is nearly Line-of-Sight (LOS). The measured path gain peak however is not perfectly reproduced by the simulation because the LOS path between Tx and Rx is slightly obstructed by an irregular road bump. Also, PG in the vicinity of the street intersection is underestimated by the simulation. It can be shown that diffraction on the vertical edges of the street intersection cannot account for the

relatively high measured path gain values beyond the LOS boundary, which are probably due to different phenomena, not considered by the RT-tool, e.g. transmission through walls, local scattering from cars, trees etc.
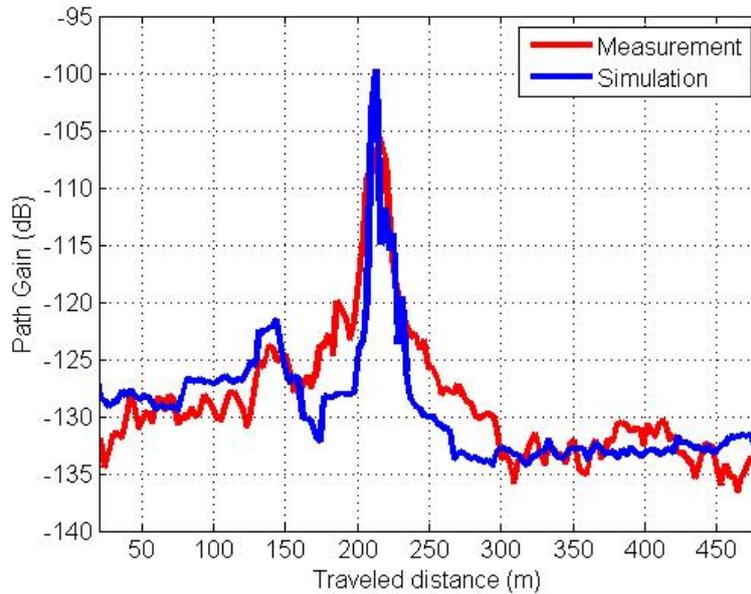
Figure 4.8 - Route EF, Path Gain comparison
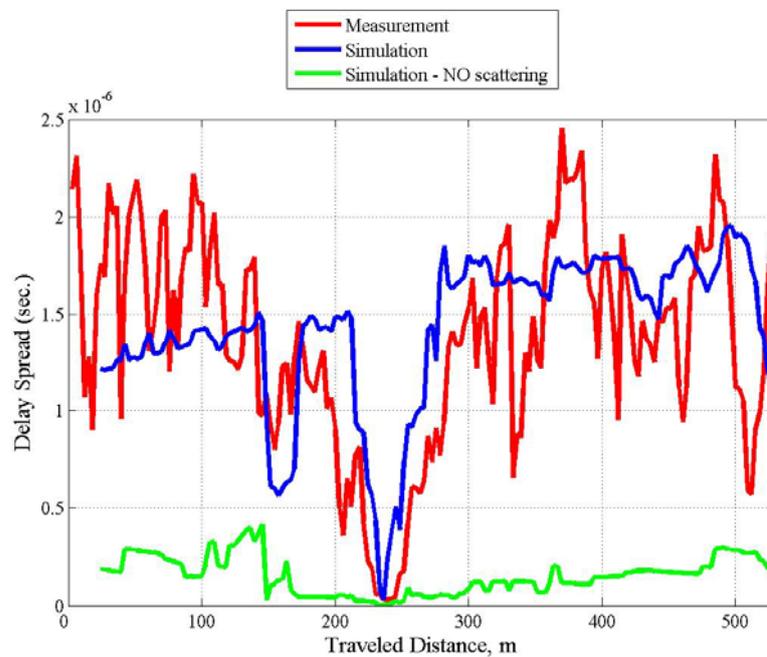
Figure 4.9 - Route EF, Delay Spread comparison

Although the Path Gain agreement is generally fairly good, investigations in terms of Delay Spread (DS) are needed to highlight the role of diffuse scattering (Figure 4.9).

A slight underestimation can be observed especially at the beginning of the route, but overall the DS comparison is rather satisfactory. It is evident (see the green line reporting the DS simulated without diffuse scattering) that the measured DS is quite well reproduced by the model *because of* diffuse scattering from far objects. Many buildings around the water basin on the right side of the route (Figure 4.7) are in fact responsible for long–delayed diffuse scattered echoes at the Rx. Reflection and diffraction alone are not efficient in this respect due to the small angular spreading involved with them.

The 3D approach also allows interesting comparisons in terms of multidimensional power-delay and power-DoA (Direction of Arrival) plots (Figures 4.10-4.13). It is evident that the agreement is good despite the different graphical aspect of the plots. Part of this difference is probably due to the finite bandwidth of the measurements system, which probably determined a sort of multipath fading also in wideband parameters.
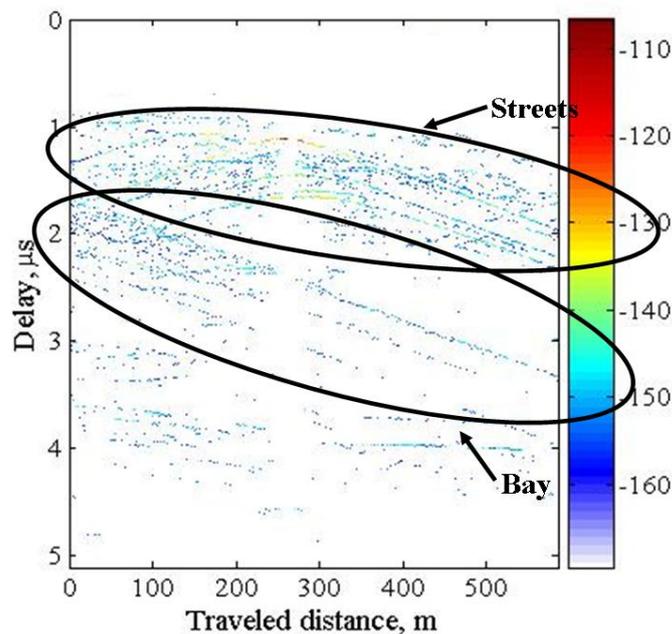
Figure 4.10 - Route EF, measured power – delay profile
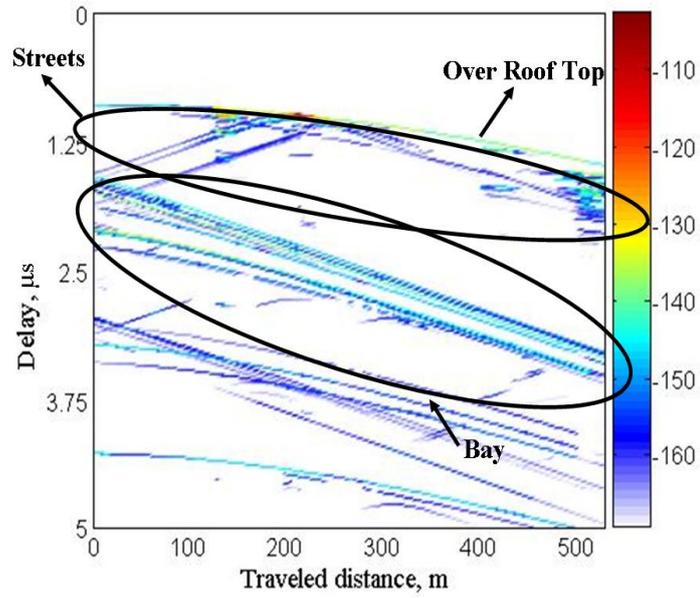
Figure 4.11 - Route EF, simulated power – delay profile
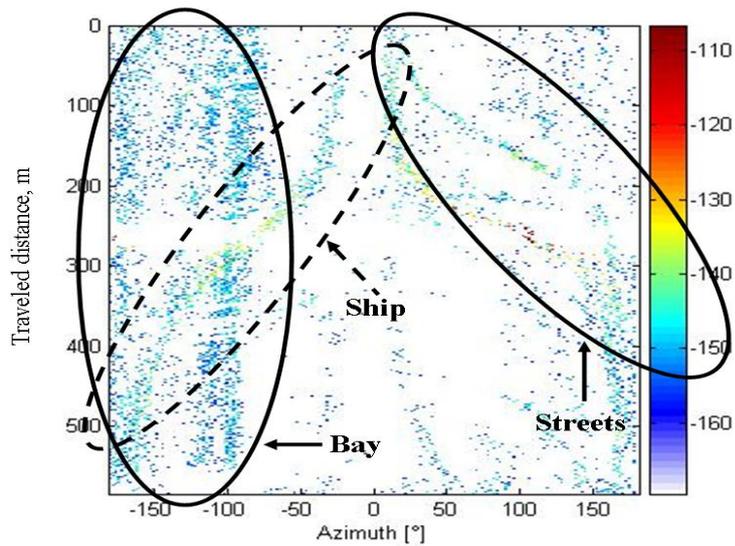
Figure 4.12 - Route EF, measured power – DoA profile
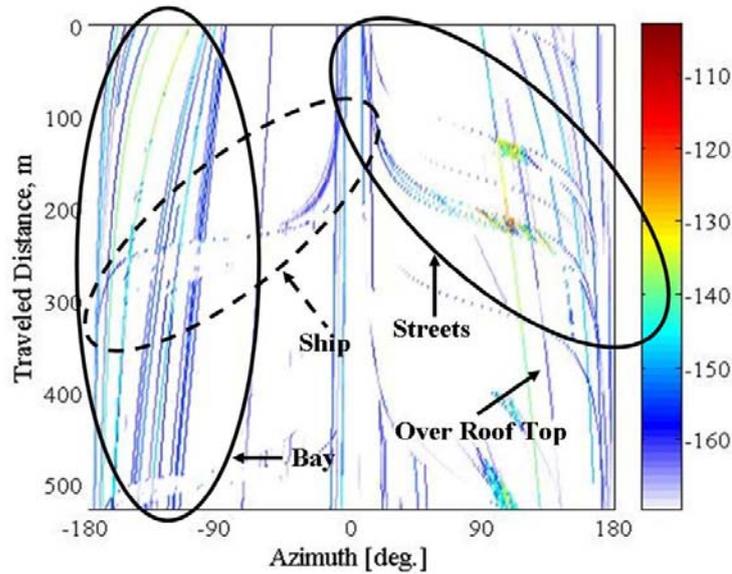
Figure 4.13 - Route EF, simulated power – DoA profile

According to the measurements, the received contributions are clustered into different groups, which are well reproduced by RT simulation. Moreover, ray tracing can be used to investigate the main properties of each cluster. In particular, the fastest contributions are due to propagation along street canyons (S_1 and S_2 in Figure 4.7); after some reflections and/or diffusions on the lateral walls of the street canyons, the signal can reach all the receiver locations only after a diffraction at street corners. These contributions appear to be slightly undervalued by RT, and this may contribute to the underestimation in the PG values shown in Figure 4.8.

The open, wide bay extending to the right of the route (Figure 4.7) allows the reception of many rays in spite of their long propagation delays (Figure 4.10 and 4.11). These contributions are mainly originated by scattering on the walls of the tall, prominent buildings located on the southern side of the bay.

In particular, according to the RT simulation, rays scattered from the "southern buildings" carry the most significant power contributions to the first receiver locations of the route; this is not in good agreement with measurement and this could explain the underestimation of DS in Figure 4.9.

The main rays belonging to the described clusters of rays are shown in Figure 4.14.
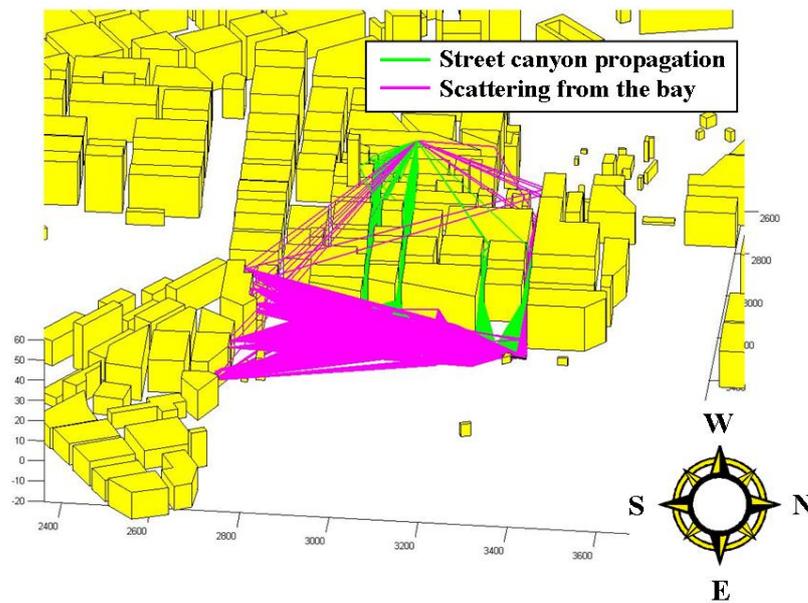
Figure 4.14 – Route EF: Clustering of received rays

Simulation results in Figure 4.12 and 4.13 clearly show the contribution due to over roof top (ORT) propagation, i.e. the ray propagating in the vertical plane and reaching the receivers after multiple diffractions on building tops. The lack of similar contributions in measured values can be easily explained if we consider that "vertical plane" propagation along the Over-Roof-Top (ORT) Tx-Rx line is an idealization, even though widely used and often inevitable. In practice, several ORT paths may exist between the terminals, exploiting the actual shapes of the roofs and the presence of objects like chimneypots, roof terraces, small shelters, etc. (which are always neglected in the urban databases).

In order to highlight the strong impact of the environment on propagation (especially on the wideband properties of the radio channel), some contributions in Figure 4.12, probably produced by a ship anchored in the harbour when measurements were performed, are worth noticing. Actually, the RT simulation has contributed to strengthen this hypothesis, since similar contributions show up in Figure 4.13 only after adding a new "virtual" obstacle representing the ship (Figure 4.7) to the original database.

4.6.2 Route GH

Likewise in route EF in the typical street canyon topology of route GH diffuse scattering is very important. From Figure 4.15 it is evident that the transmitter can illuminate almost all the buildings on the northern side of the street, and a considerable amount of the incident power is then scattered down directly to the receivers along the street. This is confirmed by the result reported in Figure 4.16, where also the prediction without diffuse scattering is shown.
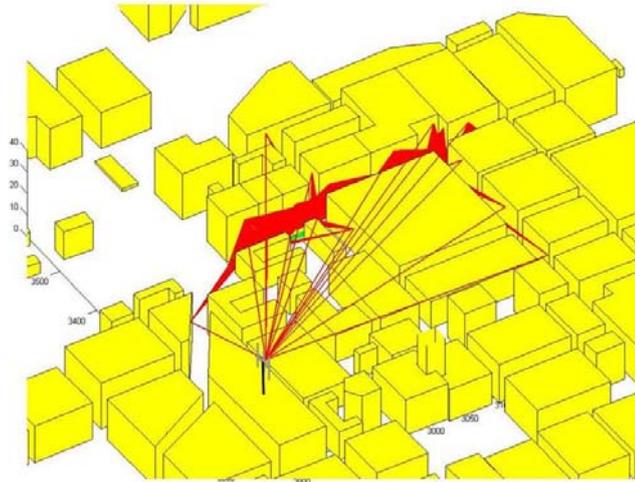
Figure 4.15 - Route GH, scattered rays from transmitter to receivers
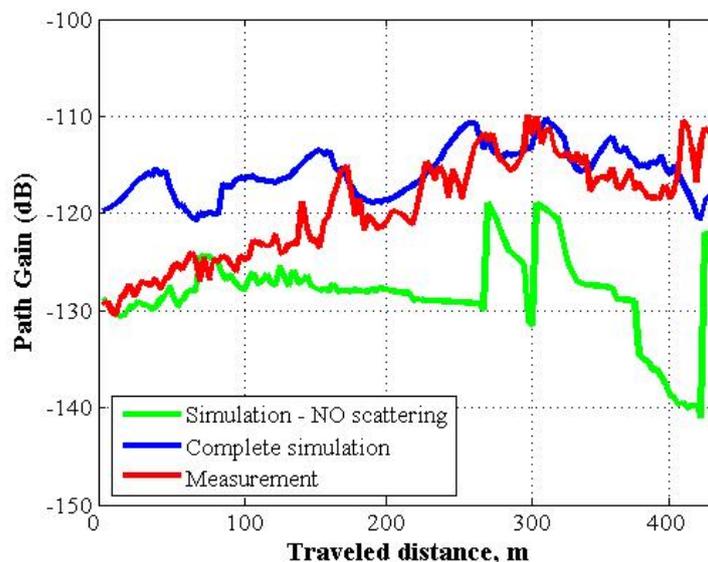
Figure 4.16 - Route GH, PG with and without scattering vs. measurement

DS comparison is shown in Figure 4.17.
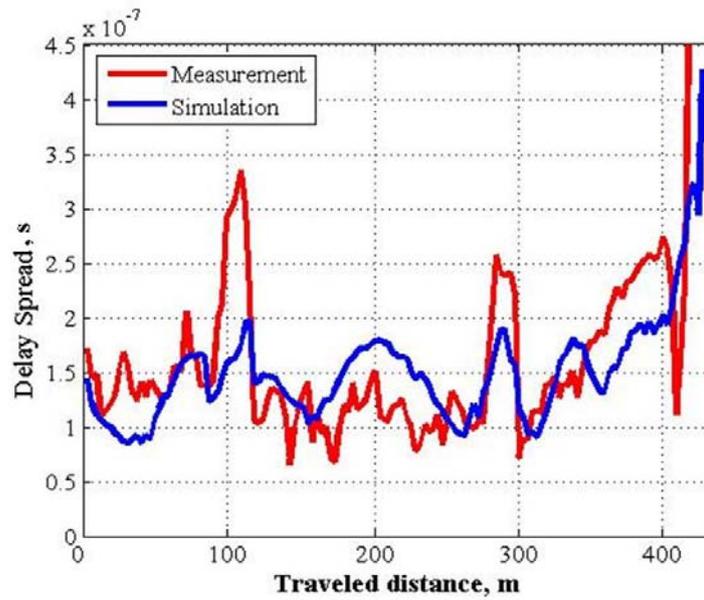
Figure 4.17 - Route GH, DS comparison

Power-delay and power-DoA profiles are shown in Figures 4.18 to 4.21. The comparison is fairly good: thanks to the 3D approach with diffuse scattering, RT is capable to reproduce the clusters of the received contributions
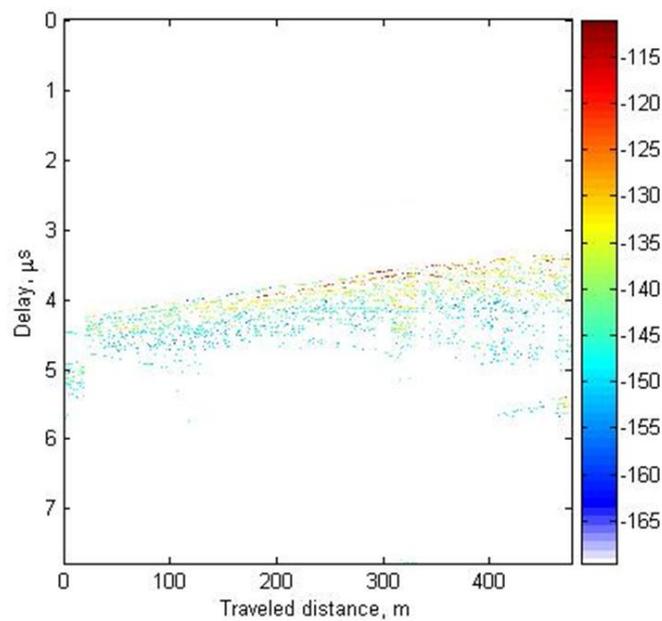
Figure 4.18 - Route GH, measured power – delay profile
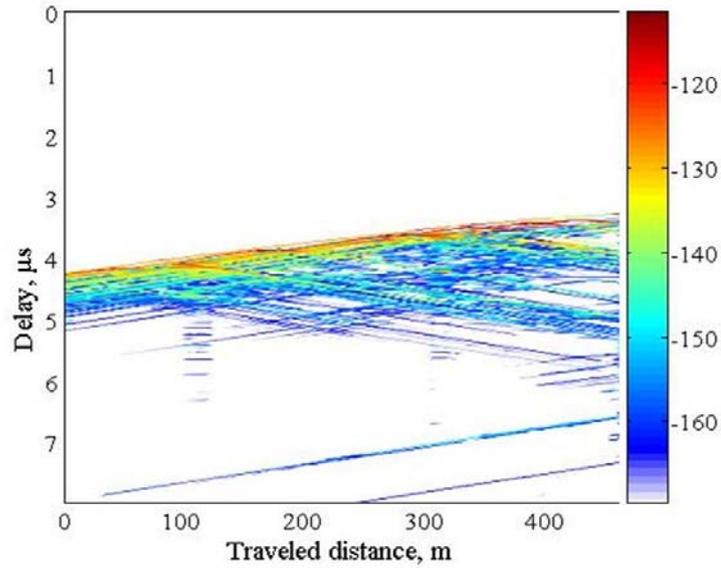
Figure 4.19 - Route GH, simulated power – delay profile
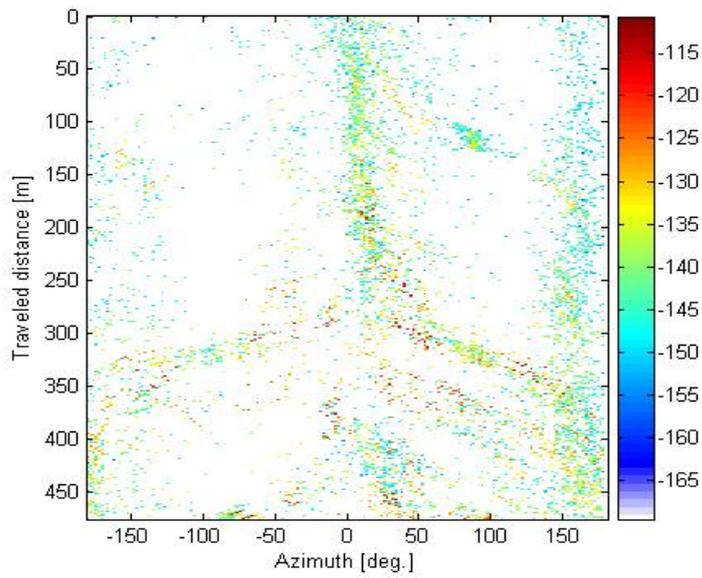
Figure 4.20 - Route GH, measured power – DoA profile
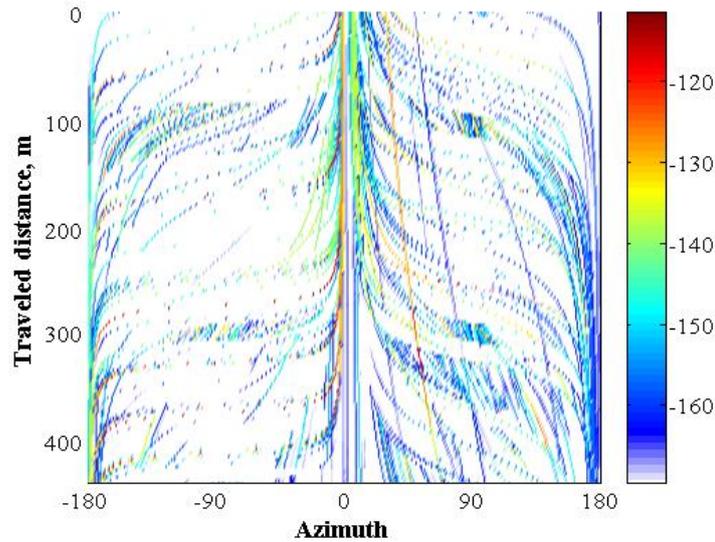
Figure 4.21 - Route GH, simulated power – DoA profile

4.6.3 Route NO

This is a very simple LOS street canyon case. Therefore, this should be an easy topology to simulate with RT. Unfortunately, this assumption is not fully supported by the results. PG comparison is shown in Figure 4.22: the agreement is fine but generally worse than in the previous EF and GH cases.
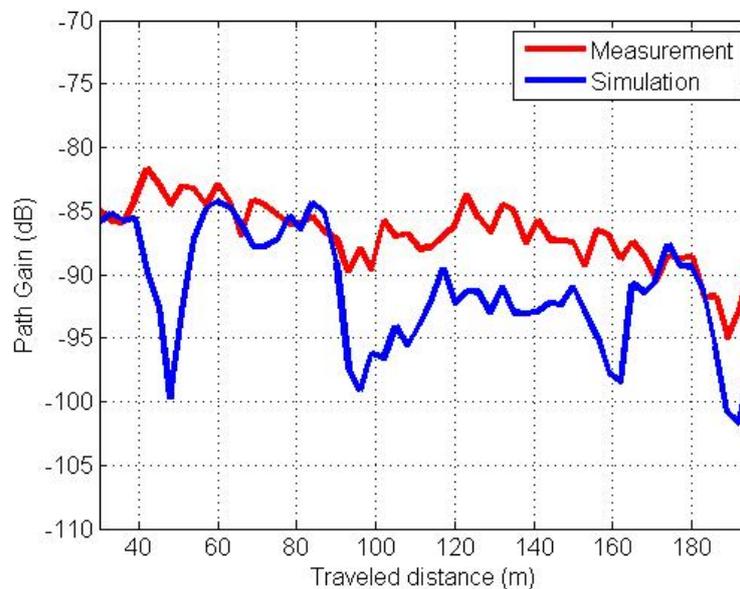
Figure 4.22 - Route NO, PG comparison

In LOS condition, the received power (i.e. PG) mainly depends on few received rays: the direct ray, the ray reflected by the ground and the rays reflected on the lateral walls of the buildings forming the street canyon. Since these rays carry

comparable power, their interference must be carefully evaluated in order to achieve a good prediction. Unfortunately, errors of just some tens of centimeter in the position of walls and corners, which are quite usual in the available databases, can have a heavy impact on the correct evaluation of interference by means of the RT tool. For this reason, although the considered full-vectorial ray tracing model is capable to reproduce interference fading, prediction is not always reliable.

Power-delay profiles are drawn in Figures 4.23 and 4.24. Back-scattering lines arising from the LOS path are present in both plots. However, simulations reproduce few, widely-spaced lines, whereas a greater number of closer lines is present in measurements. This line rate in measurements suggests that these contributions could be related to periodic building structures (pillars, windows, etc.), which of course cannot be taken into account in simulations since such structures are not present in the input database.
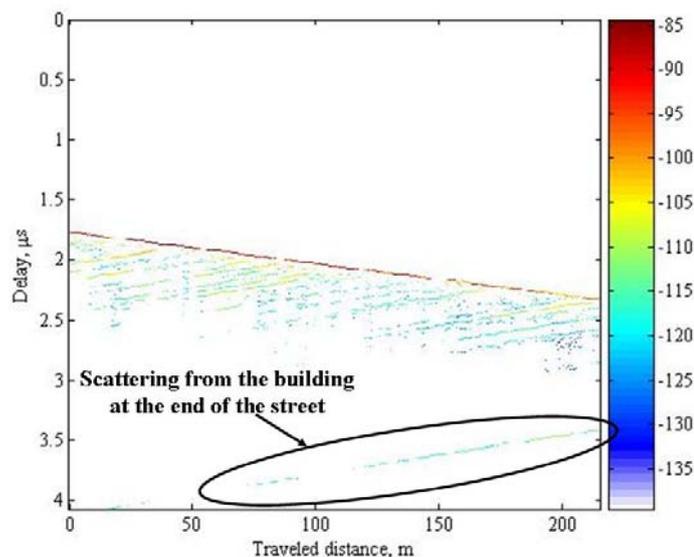
Figure 4.23 - Route NO, measured power – delay profile
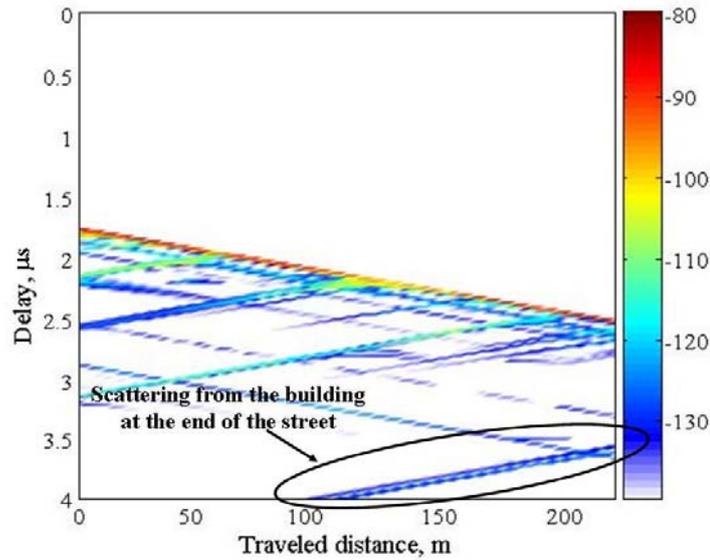
Figure 4.24 - Route NO, simulated power – delay profile

Both measurements and simulation show a major high-delay contribution received in correspondence of the right half section graph. The delay values and the slope of the lines indicate that the receiver is moving towards the secondary source, and analyzing this contribution by means of the RT tool, we found that it correspond to diffuse scattering from the far building located in the oblique road in front of the left end of route NO (Figure 4.3).

4.7 Conclusions

In this chapter, an extensive, multidimensional analysis of multipath propagation in urban micro- and macro-cellular environment has been carried out. PG, DoA, DS results, measured with a sophisticated spherical array antenna receiver and simulated with an advanced RT tool have been analyzed and compared. In agreement with previous studies [36-38], diffuse scattering, often referred to as the "dense multipath component" not following reflection of diffraction rules, has been confirmed to be an important propagation mechanism in most cases, not only in wideband assessment (Figures 4.9, 4.11, 4.13, and 4.24), but also in some narrowband cases (Figure 4.16).

Power-delay-distance and power-DoA-distance plots have shown that rays are clustered into different groups. Analyzing the RT results, back-tracking the ray trajectories and interactions, the main properties of each cluster have been identified, useful information about the major propagation mechanisms have

been obtained and the groups of buildings interacting with clustered rays have been singled out.

A satisfactory agreement between measurement and simulation has been achieved with a low number of interactions (N_{ev}) in almost all the considered cases.

The adopted advanced RT tool may therefore be used to model the dynamic evolution of channel properties in delays and angle of arrivals / departure. These aspects, still lacking in system simulation channel models such as [67, 98], will be more and more important in future system design and deployment.

Chapter 5

MIMO Capacity Prediction through Ray Tracing Simulation

5.1 Introduction

In the previous chapters it has been shown that RT performance can be sensibly improved by extending RT capabilities to diffuse scattering prediction through the simple "Effective Roughness" (ER) model, and the accuracy of multidimensional predictions vs. measurements with respect to conventional RT has been improved while reducing CPU time. In this chapter, the advanced 3D RT program described in [38] is applied to MIMO channel characterization in a "Manhattan-like" propagation scenario, which can be regarded as representative of a number of meaningful environments. The capability of RT to properly reproduce MIMO-related propagation parameters such as capacity, angle spread, and spatial correlation in the different environments (with different propagation mechanisms) is analyzed in the following text.

Then the RT output is post-processed and the theoretical MIMO capacity is evaluated through simple capacity estimation formulas in the various cases.

5.2 Ray Tracing Simulation of the MIMO Channel

A proper image Ray Tracing (RT) tool [38] has been considered for a suitable MIMO channel characterization. A full 3D approach has been adopted in order to

obtain a reliable description of multipath components coming from prominent buildings in dense urban areas, which could not be achieved with 2D approaches. A coherent computation of the field is provided, which is necessary for MIMO channel characterization. Therefore, the electric field corresponding to each radio path (ray) is represented by a complex vector $\vec{E}$, whose amplitude and phase depend on the travelled distance and the interactions (reflections, diffractions, etc.) experienced by the propagating wave. Moreover, a diffused scattering model based on the "Effective Roughness" model [36, 37] has been embedded into RT simulator, in order to account for scattering contributions which have been shown to play an important role in reproducing realistic multipath characteristics [16, 17].

5.3 The Simulation Scenario and the Antennas

In this paragraph, the considered simulation scenario is briefly described, and then the obtained results in terms of MIMO performance parameters, and of more general synthetic propagation parameters are presented. The scenario is an ideal, "Manhattan-like" map (Figure 5.1), with buildings size 100x30 m, heights variable between 20 m and 140 m. The width of the streets is 20 m.
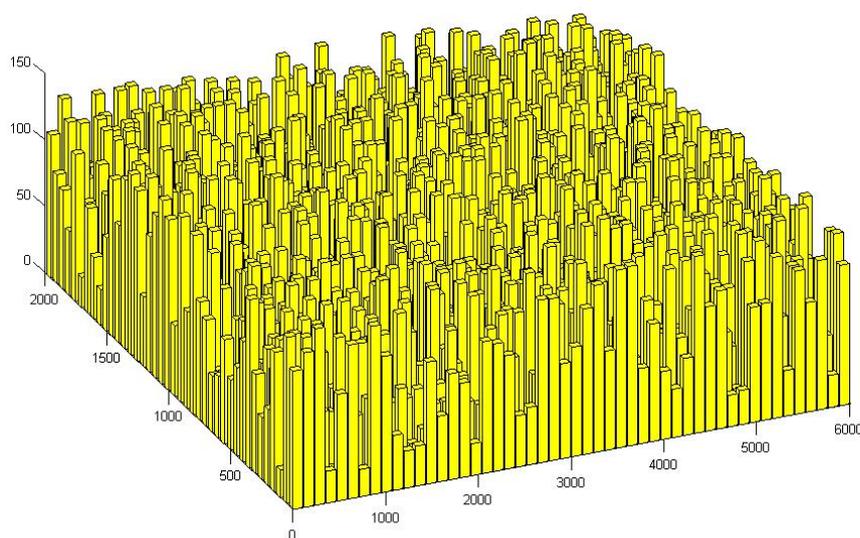
Figure 5.1 – Example of Manhattan-like scenario (3D view)

The simulations refer to a 8x8 dual-polarized MIMO system, consisting of a 16-element transmit linear (horizontal) array (Figure 5.2), and a 16-element receive planar array (Figure 5.3), both made up of 8 element pairs with alternating polarizations. Besides, some results referring to a system made up of 2x2 dual-polarized sub-arrays are also shown in the paragraph. The carrier frequency is 2.11 GHz, and transmit power is 23 dBm per element. The bandwidth of the system is 32 KHz, which can be reasonably supposed as narrow, so frequency selective effects are negligible.

The chosen scenario and the antenna arrays configuration are similar to those described in [17], which refers to a measurement campaign performed in Manhattan.

Figure 5.2 – Illustration of the structure of the TX array (from [17])
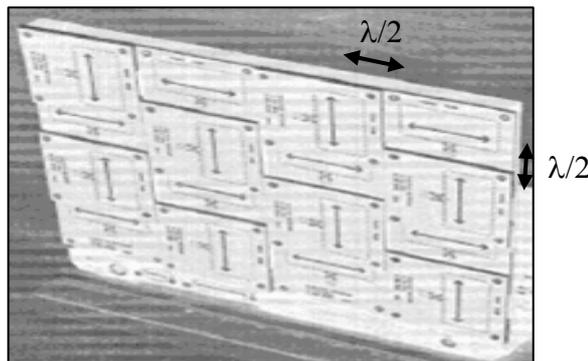
Figure 5.3 – Illustration of the structure of the RX array (from [17])

The base array is placed at a height of 100 m at the intersection of two perpendicular streets (Figure 5.7), while the height of the mobile array is 1.5 m. Different Rx positions have been considered, with both Line-of-Sight (LOS) and NLOS condition, in order to reproduce the macro-cellular scenario of [17] (Figure 5.7), made up of the two perpendicular streets facing the base array (LOS), and of nearly 10 neighbouring streets (NLOS).

5.4 Results

For each position of the Rx array (Figure 5.7), the ray-tracing method has been applied considering only one pair of elements of the Tx and the Rx arrays. Subsequently, the phase differences between rays impinging on different array elements are obtained by a simple post-processing method, and then the channel matrix is computed applying equations (4.15) and (4.16).

In order to obtain several statistical realizations of the channel matrix, in each street the RX has been moved along a route in order to reproduce phase variations on the rays and then short-term variations of the MIMO channels. Besides, different realizations of building heights have been considered, in order to emulate long-term variations of the channel. In particular, the building heights are assumed as random variables having a Gaussian p.d.f. with a mean value of 70 m and a std deviation of 20 m. Several map realizations have been considered, and the results have been averaged over all the map realizations, in order to obtain a MIMO channel characterization which can be regarded as representative of a number of typical environments, thus removing the site-specificity which is an intrinsic peculiarity of ray models.

For each realization of the channel matrix, the channel capacity is obtained by the equation (1.33) assuming a SNR of 10 dB. The SNR is regarded as a constant for each realization of $\mathbf{H}$ as if the transmitter array was power controlled to maintain the target value of 10 dB, as assumed in [17]. The system performance in different locations and for different map realizations can be represented in terms of Complementary Cumulative Distribution Functions (CCDF) of channel capacity. In Figure 5.4 a comparison between capacity CCDF obtained through RT simulations is shown, for the 2x2 dual-polarized system assuming ρ = 10 dB. The dotted line refers to a traditional RT simulation, in which only reflections, transmissions and diffractions on smooth walls are considered. The continuous line is obtained using the advanced 3D RT program described in [38], which has been enhanced by the ER scattering models introduced in [36,37,42]. Due to the incoherent nature of such models, which only allow to estimate the intensity of the scattered field, the phases of the field components carried by rays which undergo scattering interactions are modeled as random variables with a uniform p.d.f. in the range $[0,2\pi]$ (but the phase differences between rays impinging on different array elements are preserved, according to the "narrowband array" assumption). In this way, several realization

of **H** can be obtained for each Rx location, and the mean capacity in each location can be obtained averaging capacity values referring to different realizations of the channel matrix.
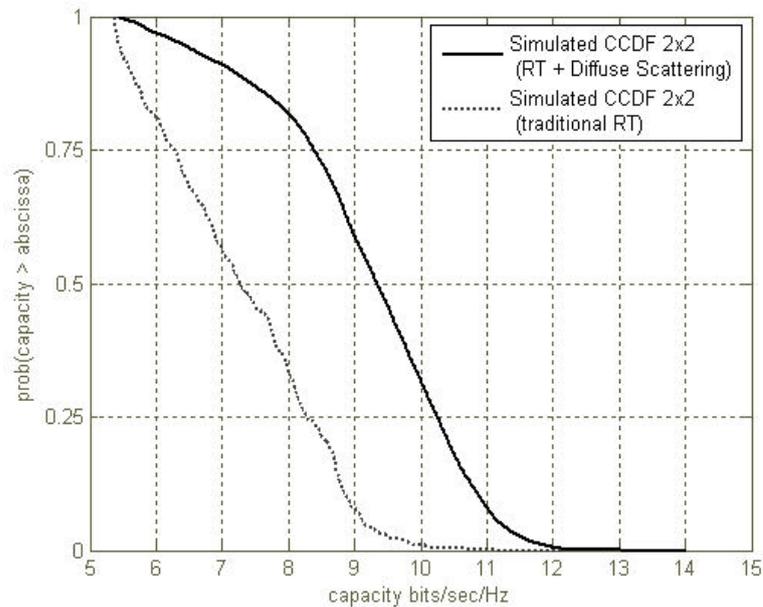
Figure 5.4 - Predicted Capacity CCDF of 2x2 system (ρ =10 dB) – RT with ER scattering model vs. traditional RT

Following this approach, the estimated capacities strongly increase w.r.t. capacities obtained through a traditional RT simulation, as shown in Figure 5.4.

This trend is still more evident in Figure 5.5, where an analogous comparison is shown for the 8x8 dual polarized system. In this case, the estimated ergodic capacity increases up to three times the ergodic capacity computed using a traditional RT, if diffuse scattering is carefully modeled. Moreover, the CCDF is more spread when diffuse scattering is considered, since the capacity can vary from very small values to values quite close to the optimal i.i.d. capacity.
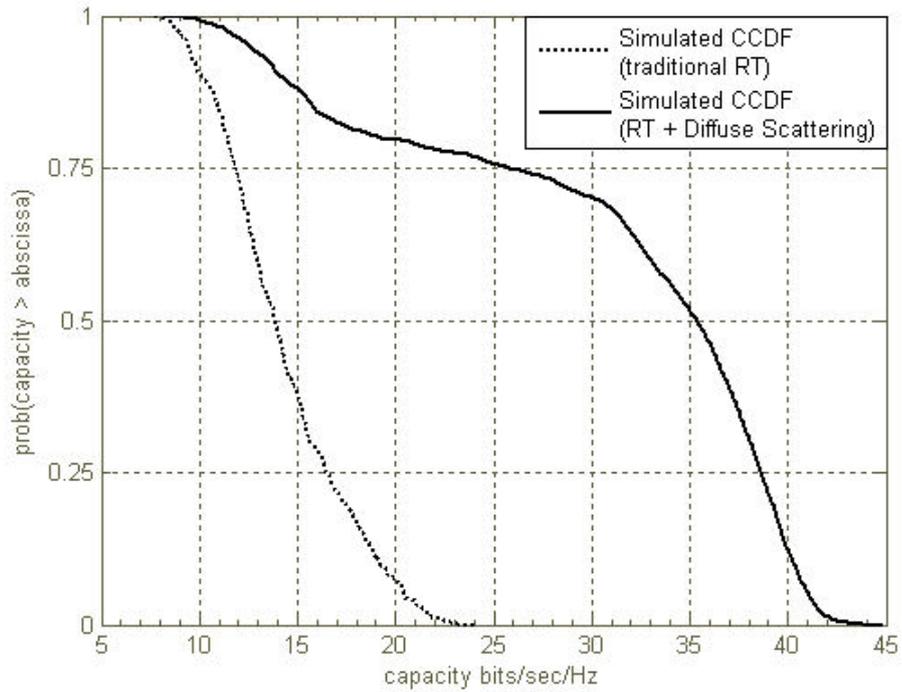
Figure 5.5 – Predicted Capacity CCDF of 8x8 system (ρ =10 dB) - RT + scattering model vs. traditional RT
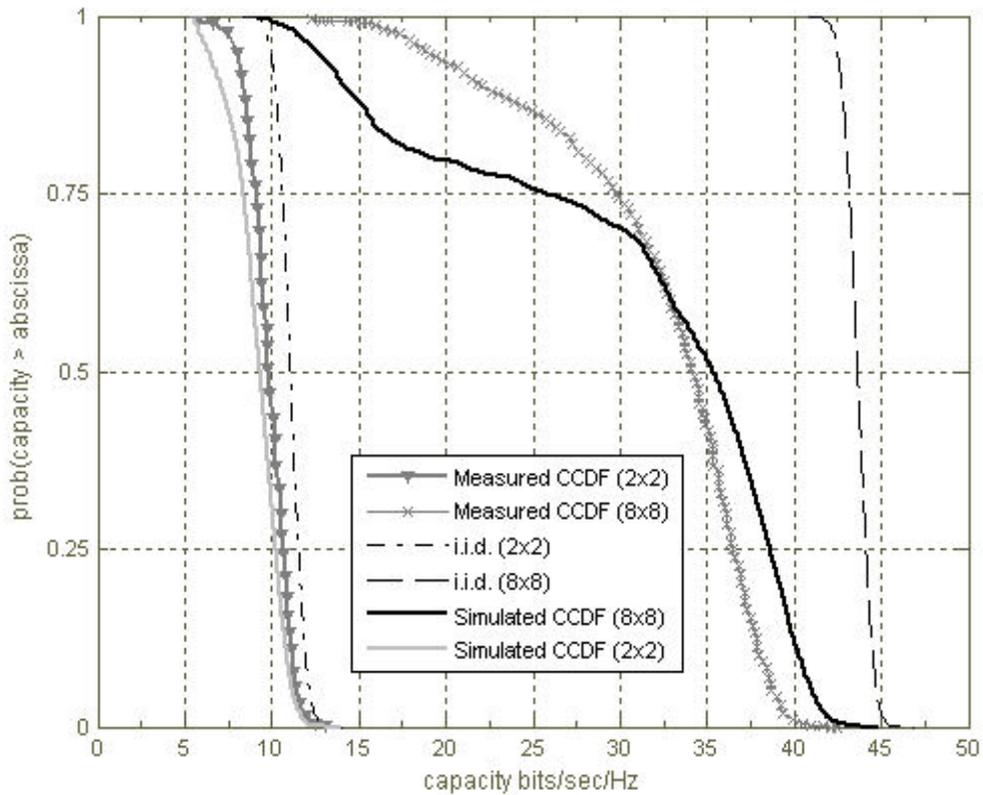
Figure 5.6 – CCDF of measured (from [17]) and predicted capacities (ρ =10 dB)

In Figure 5.6 a comparison between the CCDF of measured capacity values

[17] and the CCDF obtained from RT simulations (including the ER scattering model) is shown, for the 2x2 and the 8x8 systems, at SNR of 10 dB. The dashed lines are the reference theoretical CCDFs of the complex Gaussian i.i.d. (full scattering) channel, for the same array size and SNR. The agreement between measurements and simulations is good, regarding both mean capacity and spreading of capacity values.

Figures 5.7 and 5.8 give an overview of the measured (from [17]) and predicted mean capacities (at 10 dB SNR) of the 8x8 system, respectively, for each Rx location, by representing the capacity as a color scale point. The predicted capacity values are quite similar to those measured in [17]; as expected, the worst capacity values are obtained in the streets with LOS condition, due to the presence of a strong dominant term which enhances correlation.
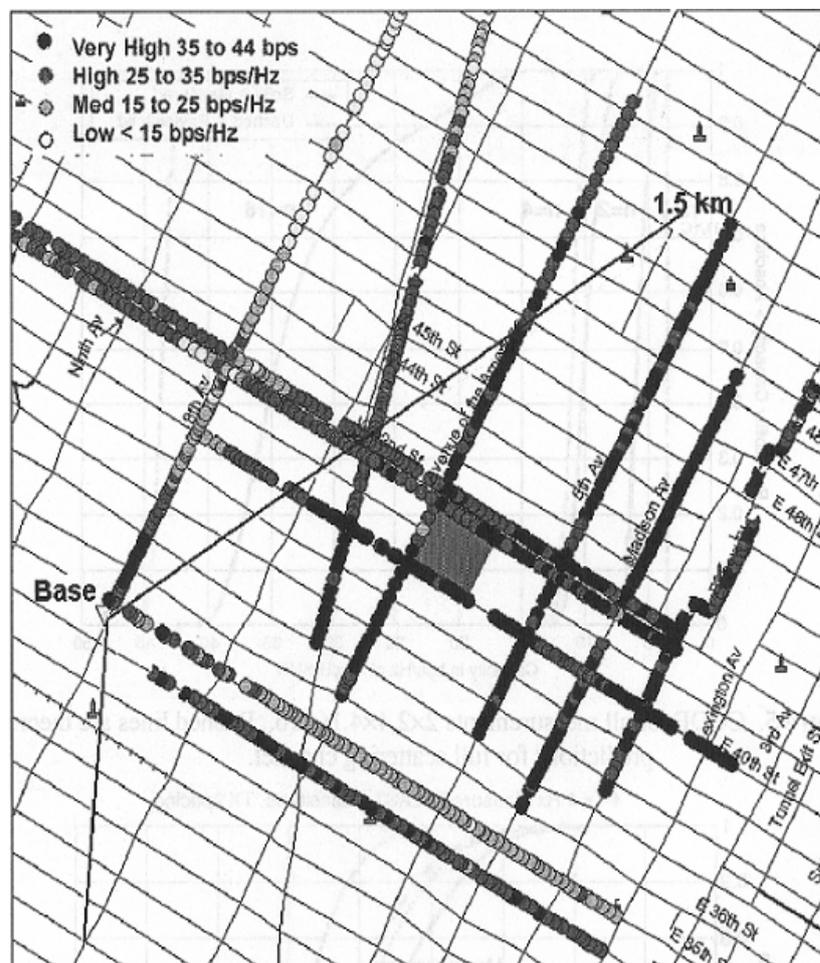
Figure 5.7 (from [17]) – Measured Mean Capacity of the 8x8 dual-polarized system in different RX locations (ρ=10 dB)
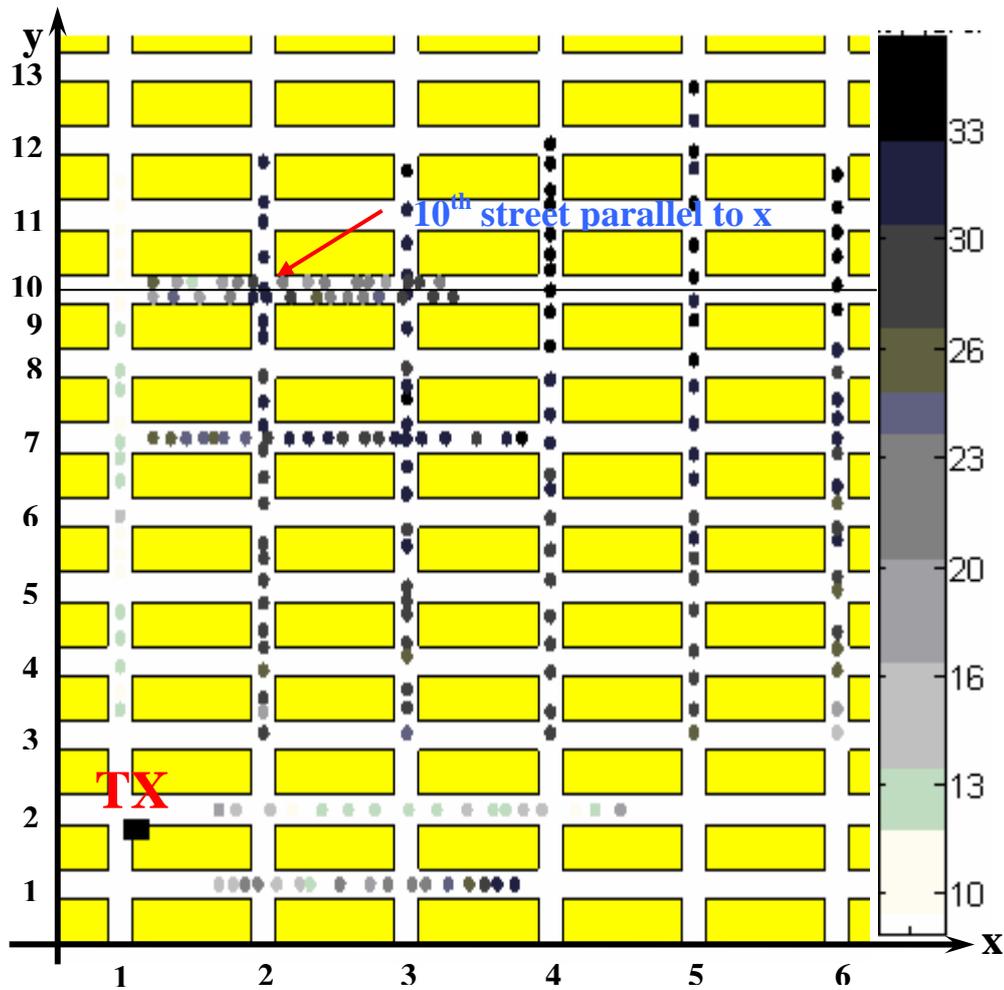
Figure 5.8 – Simulated Mean Capacity of the 8x8 dual-polarized system in different RX locations (ρ=10 dB)

In Figure 5.9 the predicted values of capacity in different Rx locations along the 10th street parallel to x axis (see Figure 5.8) are plotted, for the 8x8 system at SNR of 10 dB. Moving the receiving array along this street, which represent a strongly NLOS scenario, good capacity results are achieved in all the considered Rx locations, since capacity is almost always over 30 b/s/Hz and sometimes exceeds 40 b/s/Hz.
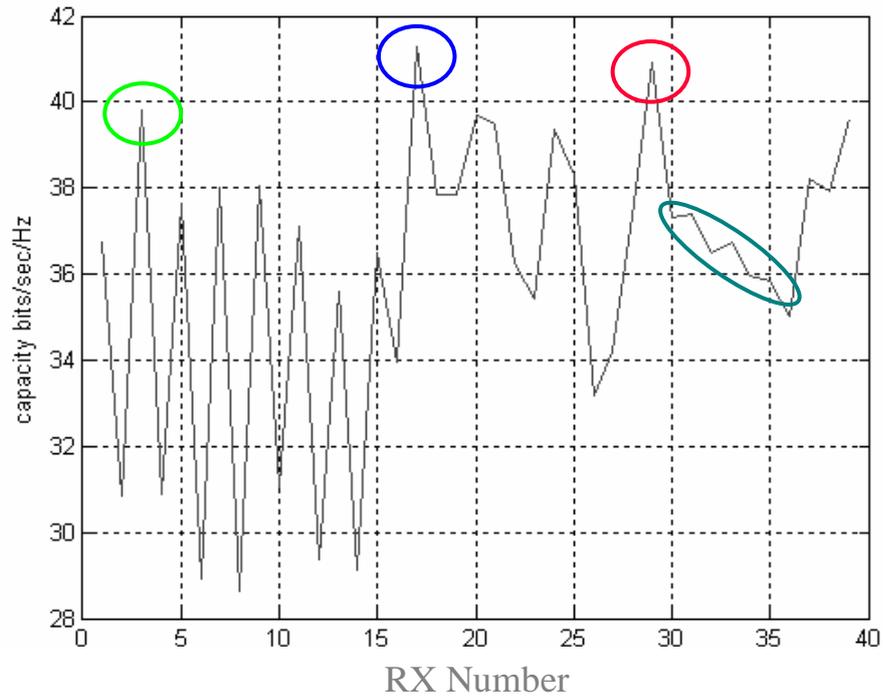
Figure 5.9 – Capacity values of 8x8 system (ρ =10 dB) in different RX locations along the 10th street parallel to the x axis

In Figure 5.10 the predicted values of rms azimuth spread in the same Rx locations of Figure 5.9 are shown: it is evident how Rx angle spread is related to channel capacity.
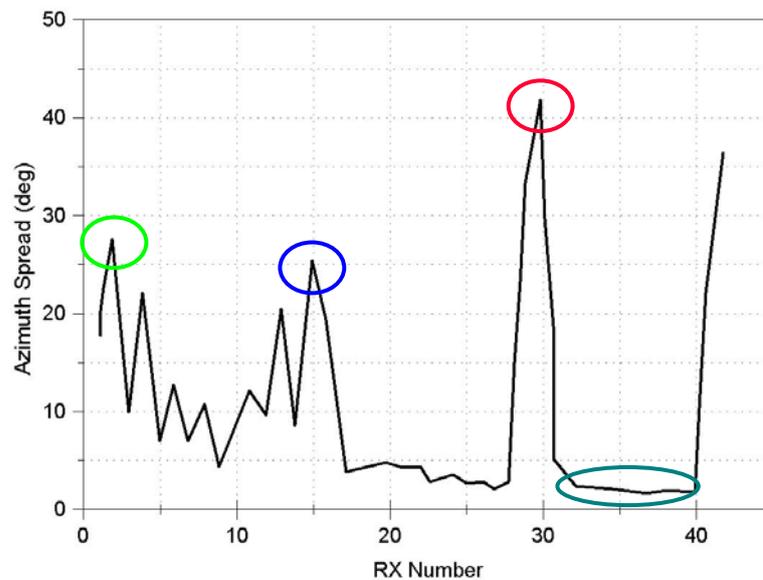
Figure 5.10 – RMS Azimuth Spread in different Rx locations along the 10th street parallel to the x axis

5.5 Conclusions

In conclusions, the results obtained with the adopted RT tool follow the same trends observed in experimental investigations, as shown through comparison between simulated and measured [17] absolute values of capacity.

Besides, it has been shown that modelling the diffuse scattering phenomena is necessary to reproduce the actual degree of multipath richness of a given environment and to get a good MIMO capacity prediction, whereas traditional RT methods tends to underestimate it.

Finally, in the considered scenarios and antenna configurations the correlation between predicted capacity and angular spread is confirmed by the results.

Further comparison between simulated and measured values in typical environments are being carried out and will be presented in future work.

Bibliography

[1]   P. A. Bello, "*Characterization of randomly time-variant linear channels*", IEEE Transactions on Communication Systems, Vol. CS-11, pp. 360-393, December 1963.

[2]   I. E. Telatar, "*Capacity of multiantenna gaussian channels*", Eur. Trans. Tel., vol. 10, no. 6, pp. 585-595, Nov./Dec. 1999.

[3]   G. J. Foschini, M. J. Gans, "*On limits of wireless communications in a fading environment when using multiple antennas*", Wireless Pers. Commun., vol. 6, pp. 311-335, Mar. 1998.

[4]   D. Gesbert, M. Shafi, D. Shiu, P. J. Smith, A. Naguib, "*From Theory to Practice: An Overview of MIMO Space-Time Coded Wireless Systems*", IEEE J. Select. Areas Commun., vol. 21, no. 3, April 2003.

[5]   Goldsmith, S.A. Jafar, N. Jindal, and S. Vishwanath, "*Capacity Limits of MIMO Channels*", IEEE J. Select. Areas Commun., vol. 21, no. 5, pp. 684-702, June 2003.

[6]   T. Marzetta, B. Hochwald, "*Capacity of a Mobile Multiple-Antenna Communication Link in Rayleigh Flat Fading*", IEEE Transactions on Information Theory, vol. 45 No 1, pp. 139-157, January 1999.

[7]   A. J. Paulraj, D. A. Gore, R. U. Nabar, H. Bölcskei, "*An Overview of MIMO Communications – A Key to Gigabit Wireless*", Proceedings of the IEEE, vol. 92, no. 2, February 2004.

[8]   A. J. Paulraj, R.U. Nabar and D. A. Gore, "*Introduction to Space-Time Wireless Communications*", Cambridge Univ. Press, 2003.

[9]   A. B. Gershman, N. D. Sidiroupolus (Editors), "*Space-Time Processing for MIMO communications*", Wiley & Sons, 2005.

[10]   B. Vucetic, J. Yuan, "*Space-Time Coding*", Wiley & Sons, 2003.

[11]   M. Jankiraman, "*Space-Time Codes and MIMO Systems*", Artech House, 2004.

[12]   V. K. N. Lau, Y. K. R. Kwok, "*Channel-Adaptive Technologies and Cross-Layer Designs for Wireless Systems with Multiple Antennas – Theory and Applications*", Wiley & Sons, 2006.

[13]   A. Goldsmith, *Wireless Communications*, Cambridge University Press, 2005.

[14]   T. S. Rappaport, "*Wireless Communications: Principles and Practice*", Prentice Hall, 1996.

[15]   Svantesson, T., Wallace, J., "*On signal strength and multipath richness in multi-input multi-output systems Communications*", IEEE International Conference ICC '03., Volume 4, pp. 2683 – 2687, 11-15 May 2003.

[16]   M. A. Jensen, J. W. Wallace, "*A review of Antennas and Propagation for MIMO Wireless Communications*", IEEE Trans. Antennas an Propagation, vol. 52, no. 11, November 2004.

[17]   D. Chizhik, J. Ling, P. Wolniansky, R.A. Valenzuela, N. Costa and K. Huber, "*Multiple-input-multiple-output measurements and modelling in Manhattan*", IEEE J. Select. Areas Commun., vol. 23, pp. 321-331, April 2003.

[18]   Da-Shan Shiu, G.J. Foschini, M.J. Gans, J.M. Kahn,. "*Fading correlation and its effect on the capacity of multielement antenna systems*", IEEE Trans. Communications, Vol. 48, No. 3, pp. 502 – 513, March 2000.

[19]   Dmitry Chizhik, Gerard J. Foschini, Michael J. Gans and Reinaldo A. Valenzuela, "*Keyholes, Correlations, and Capacities of Multielement Transmit and Receive Antennas*", IEEE Trans. Communications, Vol. 1, NO. 2, April 2002.

[20]   J. Salz, J. H. Winters, "*Effect of fading correlation on adaptive arrays in digital mobile radio*", IEEE Transactions on Vehicular Technology, , Vol. 43 No. 4, pp. 1049-1057, November 1994.

[21]   R. G. Vaughan, J. Bach Andersen, "*Antenna diversity in mobile communications*", IEEE Transactions on Vehicular Technology, Vol. 36 No 4, pp 149-172, November 1987.

[22]   R. G. Vaughan, "*Polarization diversity in mobile communications*", IEEE Transactions on Vehicular Technology, Vol. 39 No 3, pp 177-186, , August 1990.

[23]   J. Laurila, K. Kalliola, M. Toeltsch, K. Hugl, P. Vainikainen, and E. Bonek, "*Wideband 3-D Characterization of Mobile Radio Channels in Urban Environment*", IEEE Transactions on Antennas and Propagation, vol. 50, no. 2, pp. 233-243, February 2002.

[24]   K. Kalliola, H. Laitinen, P. Vainikainen, M. Toeltsch, J. Laurila, E. Bonek, "*3-D double-directional radio channel characterization for urban macrocellular applications*", IEEE Transactions on Antennas and Propagation, Vol. 51, No. 11, Pages: 3122 - 3133, November 2003.

[25]   P. Degauque (Editor), E. Van Lil, V. Degli-Esposti, P. Vainikainen, F. Cardoso, W. A. Th. Kotterman, L. M. Correia, "*Propagation modelling and channel characterization*", chapter 4 of the book: "Mobile Broadband Multimedia Networks – Techniques, Models and Tools for 4G", COST Action 273, Final Report, Edited by L. M. Correia, Academic Press, 2006.

[26]   L. M. Correia (Editor), "*Mobile Broadband Multimedia Networks – Techniques, Models and Tools for 4G*", COST Action 273, Final Report, Academic Press, 2006.

[27]   L. M. Correia (Editor), "*Wireless Flexible Personalised Communications*", COST Action 259, Final Report, John Wiley & Sons Canada, 2001.

[28]   E. Damosso (Editor), *"Digital mobile radio towards future generation systems"*, European COST action 231, Final Report, European Commission, Brussels, 1999.

[29]   T. Kürner, D. J. Cichon and W. Wiesbeck, "*Concepts and results for 3D digital terrain-based wave propagation models: an overview*", IEEE Journal on Selected Areas in Communications, Vol. 11, No. 7, pp.1002-1012, September 1993.

[30]   M. C. Lawton and J. P. McGeehan, "*The application of a deterministic ray launching algorithm for the prediction of radio channel characteristics in small-cell environment*s", IEEE Trans. Veh. Technol., vol. 43, pp.955-969, Nov. 1994.

[31]   G. Liang and H. L. Bertoni, "*A new approach to 3D ray tracing for propagation prediction in cities*", IEEE Trans. Ant. Propagat., vol. 46, no. 6, pp.853-863, June 1998.

[32]   Hsueh-Jyh Li, Cheng-Chung Chen, Ta-Yung Liu, Han-Chang Lin*, "Applicability of ray-tracing technique for the prediction of outdoor channel characteristics"*, IEEE Transactions on Vehicular Technology, Volume: 49, Issue: 6 , Pages: 2336 – 2349, Nov. 2000.

[33]   M. O. Al-Nuaimi and M. S. Ding, "*Prediction models and measurements of microwave signals scattered from buildings*", IEEE Trans. Ant. Propagat., vol. 42, no. 8, pp.1126-1137, August 1994.

[34]   C. Kloch, J. Bach Andersen, "*Radiosity - an approach to determine the effect of rough surface scattering in mobile scenarios*", IEEE AP-S International Symposium, pp 890-893, Montreal, July 1997.

[35]   D. Didascalou, M. Dottling, N. Geng, W. Wiesbeck*, "An approach to include stochastic rough surface scattering into deterministic ray-optical wave propagation modeling"*, IEEE Transactions on Antennas and Propagation, Volume: 51 , Issue: 7 , Pages: 1508 – 1515, July 2003.

[36] V. Degli-Esposti, H. L. Bertoni, "*Evaluation of the role of diffuse scattering in urban microcellular propagation*", IEEE-VTC'99 - fall, Amsterdam, The Netherlands, September 19-22, 1999.

[37] V. Degli-Esposti, "*A diffuse scattering model for urban propagation prediction*", IEEE Transactions on Antennas and Propagation, Vol. 49, No. 7, pp. 1111-1113, July 2001.

[38] V. Degli Esposti, D. Guiducci, A. de'Marsi, P. Azzi, F. Fuschini, "*An advanced field prediction model including diffuse scattering*", IEEE Transactions on Antennas and Propagation, Vol. 52, No. 7, Pages: 1717 - 1728, July 2004.

[39] F. Fuschini, H. El-Sallabi, V. Degli-Esposti, L. Vuokko, D. Guiducci, P. Vainikainen, "*Multidimensional analysis and simulation of multipath propagation in urban environment*", IEEE Transactions on Antennas and Propagation, submitted for publication.

[40] V. Degli Esposti, F. Fuschini, E. M. Vitucci, D. Graziani, "*Measurement and modelling of scattering from building walls*", COST 273 document TD(05) 065, Bologna, Italy, Jan. 19-21, 2005.

[41] V. Degli Esposti, F. Fuschini, E. M. Vitucci, D. Graziani, "*Measurement and modelling of scattering from building walls*", 14th IST Mobile & Wireless Communications Summit, Dresden (Germany), June 19-23 2005.

[42] V. Degli-Esposti, F. Fuschini, E. M. Vitucci, G. Falciasecca, "*Modelling of scattering from buildings*", IEEE Transactions on Antennas and Propagation, vol. 55 No 1, pp. 143-153, January 2007.

[43] P. Beckmann, A. Spizzichino, "*The Scattering of Electromagnetic Waves from Rough Surfaces*", Pergamon Press, 1963.

[44] F. G. Bass, I. M. Fucks, "*Wave Scattering from Statistically Rough Surfaces*", Pergamon Press, 1979.

[45]   H. Budiarto, K. Horiata, K. Haneda and J. Takada "*Experimental study of non-specular wave scattering from building surface roughness for mobile propagation modelling*", IEICE Transactions on Communications, Vol. E87-B, No. 4, Pages: 958 - 966, April 2004.

[46]   H. Budiarto, K. Horihata, K. Haneda, J. Takada, "*Polarimetric measurement of non-specular wave scattering from building surface roughness*", IEEE Antennas and Wireless Propagation Letters, Vol. 2, pp. 242-245, 2003.

[47]   P. Pongsilamanee, H. L. Bertoni, "*Specular and non-specular scattering from building facades*", IEEE Transactions on Antennas and Propagation, Vol. 52, No. 7, Pages:1879 - 1889, July 2004.

[48]   G. Valenzuela, "*Depolarization of EM waves by slightly rough surfaces*", IEEE Transactions on Antennas and Propagation, Vol. 15, pp. 552-557, 1967.

[49]   D. Didascalou, J. Maurer, W. Wiesbeck, "*A novel stochastic rough-surface scattering representation for ray-optical wave propagation model*". In IEEE *Proc. Vehicul. Technol. Conf. 2001,* vol. 3, pages 1785-1788, 2001.

[50]   W. S. Ament, "*Toward a theory of reflection by a rough surface*". *Proc. IRE,* 41(1):142-146, Jan. 1953.

[51]   E. N. Bramley, S. M. Cherry, "*Investigation of microwave scattering by tall buildings*", Proc. IEEE, 42(8):1126-1137, Aug. 1994.

[52]   O. Landron, M. J. Fuerstein, T. S. Rappaport, "*A comparison of theoretical and empirical reflection coefficients for typical exterior wall surfaces in a mobile radio environment*", IEEE Trans. Ant. Prop., Vol. 44 No 3, pp. 341-351, March 1996.

[53]   K. Rizk, J. F. Wagen, J. Li, F. Gardiol, "*Lamppost and panel scattering compared to building reflection and diffraction*", COST 259 TD(97)033, Turin, Italy, May 1997.

[54]   E. Glangetas, B. Foulonneau, J.-C. Bic, *An experimental investigation of the bistatic specular scattering from rough dielectric surfaces in the 60 GHz band*", COST 259 TD(99)038, Vienna, Austria, 20-23 April 1999.

[55]   D. Guiducci, *Modelli avanzati a raggi per la previsione di campo in ambiente urbano*", PhD Thesis, 2003.

[56]   C. Cheon, G, Liang and H. L. Bertoni, "*Simulating radio channel statistics for different building environments*", IEEE J. Select. Areas Commun., vol. 19, no. 11, November 2001.

[57]   Blaunstein, N.. Toeltsch, M.. Laurila, J. Bonek, E., Katz, D.. Vainikainen, P. Tsouri, N., Kalliola, K.. Laitinen, H., "*Signal Power Distribution in the Azimuth, Elevation and Time Delay Domains in Urban Environments for Various Elevations of Base Station Antenna*", IEEE Transactions on Antennas and Propagation Volume 54, N. 10, Page(s):2902 – 2916, Oct. 2006

[58]   N. Czink, X. Yin, H. Özcelik, M. Herdin, E. Bonek, B.H. Fleury, "*Cluster characteristics in a MIMO indoor propagation environment*", IEEE Transactions on Wireless Communications, in press.

[59]   V. Degli Esposti, F. Fuschini, M. Amorini, "*Database simplification for field prediction in urban environment*", IEEE AP-S / URSI International Symposium, Monterrey (CA), USA, June 20-26, 2004.

[60]   Marina Barbiroli, Vittorio Degli Esposti, Franco Fuschini, Enrico M. Vitucci, "*Speed-up techniques for ray tracing field prediction models*" (Invited Paper), XXVIIIth URSI General Assembly, Delhi, October 23-29, 2005.

[61]   V. Degli Esposti, G. Falciasecca, F. Fuschini, E. M. Vitucci, "*Speed-up techniques for ray tracing field prediction models*", IEEE Transactions on Antennas and Propagation, to be submitted.

[62]   P. Almers, A. Burr, N. Czink, M. Debbah, V. Degli-Esposti, B. Fleury, H. Hofstetter, P. Kyösti, B.K. Lau, D. Laurenson, G. Matz, A. Molisch, A. Moustakas, C. Oestges, H. Özcelik, R. Thomä and P. Zetterberg, "*MIMO*

channel characterization and modeling", Network of Excellence in Wireless Communications (NEWCOM), Dept. II, Report 2, July 2005.

[63] E. M. Vitucci, V. Degli Esposti, F. Fuschini, "*MIMO channel characterization through ray tracing simulation*", 1st European Conference on Antennas and Propagation (EuCAP 2006), Nice, France, 6 - 10 November 2006.

[64] A. Muller, "*Monte-Carlo multipath simulation of ray tracing channel models*", in Proc. 1994 IEEE Global Telecomm. Conf., vol. 3, pp. 1446-1450, San Francisco, CA, Nov. 11 – Dec. 2, 1994.

[65] A. L. Swindlehurst, G. German, J. Wallace, M. Jensen, "*Experimental measurements of capacity for MIMO indoor wireless channels*", in IEEE Third Workshop Signal Process. Adv. Wireless Commun. 2001 (SPAWC '01), pp. 30-33, Taiwan, March 2001.

[66] Almers, Peter. Bonek, Ernst. Burr, Alister. Czink, Nicolai. Debbah, Merouane. Degli-Esposti, Vittorio. Hofstetter, Helmut. Kyösti, Pekka. Laurenson, David. Matz, Gerald. Molisch, Andreas F. Oestges, Claude. Özcelik, Häseyin, "*Survey of channel and radio propagation models for wireless MIMO systems*", EURASIP Journal on Wireless Communications and Networking, Special Issue on Space-Time Channel Modelling for Wireless Communications, Article ID 19070, Volume 2007.

[67] Kai Yu and Bjorn Ottersten, "*Models for MIMO Propagation Channels, A Review*", Department of Signals, Sensors and System, Royal Institute of Technology, 2002-07-08.

[68] H. Ozcelik, "*Indoor MIMO Channel Models*", Technical University of Wien (TUW), PhD Thesis, 2004.

[69] M. Herdin, "*Non-stationary Indoor MIMO Radio Channels*", Technical University of Wien (TUW), PhD Thesis, 2004.

[70]   W. Weichselberger, "*Spatial Structure of Multiple Antenna Radio Channels – A Signal Processing Viewpoint*", Technical University of Wien (TUW), PhD Thesis, 2003.

[71]   V. Rizzoli, "*Lezioni di Campi Elettromagnetici - Propagazione libera e antenne*", Ed. Progetto Leonardo, Bologna, 1998.

[72] Sophocles J. Orfanidis, "*Electromagnetic waves and antennas,* free book, available for download at http://www.ece.rutgers.edu/~orfanidi/ewa .

[73] Vittorio Rizzoli, Diego Masotti, "*Lezioni di sistemi d' antenna*", voll. 1 e 2, Ed. Progetto Leonardo - Esculapio, 2006.

[74]   Constantine A. Balanis, "*Antenna Theory - Analysis and Design*"*,* 3rd Edition, John Wiley & Sons, 2005.

[75]   Warren L. Stutzman, Gary A. Thiele, "*Antenna Theory And Design*"*,* 2nd Edition, Jonh Wiley & Sons, 1997.

[76]   J. D. Kraus, "*Antennas*"*,* 2nd edition, McGraw-Hill, 1988.

[77]   Robert E. Collin, "*Antennas and Radiowave Propagation*", McGraw-Hill, 1985.

[78]   G. Conciauro, "*Introduzione alle onde elettromagnetiche*"*,* Mc-Graw-Hill Italia, 1999.

[79]   E. Knott, J. F. Shaeffer, M. T. Tuley, "*Radar Cross Section*", Artech House, 1993.

[80]   H. L. Bertoni, "*Radio Propagation for Modern Wireless Systems*", Prentice Hall, 2000.

[81]   C. A. Balanis, "*Advanced Engineering Electromagnetics*", Wiley & Sons, 1989.

[82]   J. D. Parsons, *"The Mobile Radio Propagation Channel"*, 2nd Edition, Wiley & Sons, 2000.

[83]   R. Vaughan, J. Bach Andersen, *"Channels, Propagation ad Antennas for Mobile Communications"*, IEE electromagnetic waves series, no. 50, 2003.

[84]   W. C. Jakes Jr. (Editor), *"Microwave Mobile Communications"*, John Wiley & Sons, New York, NY, 1994. Reissued by IEEE, 1994.

[85]   R. G. Kouyoumjian, P. H. Pathak, *"A Uniform Geometrical Theory of diffraction for an edge in a perfectly conducting surface"*, Proceedings of the IEEE, 62(11):1448-1461, Nov. 1974.

[86]   J. Bach Andersen, *"UTD multiple-edge transition zone diffraction"*, IEEE Transactions on Antennas and Propagationm Vol. 45 No 7, pp. 1093-1097, July 1997.

[87]   R. J. Luebbers, *"Finite Conductivity Uniform GTD versus Knife Edge Diffraction in Prediction of Propagation Path Loss"*, IEEE Transactions on Antennas and Propagation, vol. 32 No 1, pp. 70-76, January 1984.

[88]   D. Har, H. Xia, H, L. Bertoni, *"Path Loss Prediction for Microcells"*, IEEE Trans. Vehicular Tech., vol. 48, no. 5, September 1999.

[89]   Walfisch, H. L.Bertoni, *"A Theoretical Model of UHF Propagation in Urban Environments"*, IEEE Trans. Ant. Propagat., vol 36, no. 12, December 1988.

[90]   S. R. Saunders, F. R. Bonar, *"Explicit Multiple Building Diffraction Attenuation Function for Mobile Radio Wave Propagation"*, Electronics Letters, Vol. 27, No 14, July 1991.

[91]   J. Deygout, *"Multiple Knife-Edge Diffraction of Microwaves"*, IEEE Trans. On Antennas and Propagation, Vol. AP-14, No. 4, pp 480-489, July 1966.

[92] S. R. Saunders, F. R. Bonar, "*Prediction of Mobile Radio Wave Propagation Over Buildings of Irregular Heights and Spacings*", IEEE Trans. Ant. Propagat., vol 42, no. 2, February 1994.

[93] M. F. Catedra, J. Perez, F. Saez de Adana, O. Gutierrez, "*Efficient Ray-Tracing Techniques for three-dimensional analyses of Propagation in Mobile Communication: Application to Picocell and Microcell Scenarios*", IEEE Antennas and Propagation Magazine, 40(2):15-28, April 1998.

[94] F. A. Agelet, A. Formella, J. M. H. Rabanos, F. I. deVicente, F. P. Fontan, "*Efficient Ray-Tracing acceleration techniques for radio propagation modeling*", IEEE Transactions on Vehicular Technology, Vol. 49 No 6, pp. 2089-2104, November 2000.

[95] G. Woelfle, B. E. Gschwendtner, F. M. Landstorfer, "*Intelligent Ray Tracing – A new approach for field strength prediction in microcells*", In IEEE Proc. Vehicul. Technol. Conf., vol. 2, pages 790-794, 1997.

[96] R. Hoppe, G. Woelfle, and P. Wertz, "*Advanced ray-optical wave propagation modelling for urban and indoor scenarios*", European Transactions on Telecommunications (ETT), 14(1), pp. 61–69, January 2003.

[97] L. R. Maciel, H. L. Bertoni, "*Unified Approach to Prediction of Propagation Over Buildings for All Ranges of Base Station Antenna Height*", IEEE Vehicular Trans, vol. 42, no. 1, February 1993.

[98] 3GPP TR 25.996, "*3rd Generation Partnership Project; technical specification group radio access network; spatial channel model for MIMO simulations (release 6)*", V6.1.0.

[99] A. Papoulis, "*Probability, Random Variables, and Stochastic Processes*", 3rd Edition, McGraw-Hill, Inc., New York, 1991.

[100] C. Ray Wylie, L. C. Barret, "*Advanced Engineering Mathematics*", McGraw-Hill, Inc., 1995.

[101] M. Abramovitz, I. A. Stegun (Editors), "*Handbook of mathematical functions*", Dover Publications, Inc., New York, NY, 1972.

[102] R. Horn, C. Johnson, "*Matrix Analysis*", Cambridge University Press, 1985.

[103] T. Cover, J. Thomas, "*Elements of Information Theory*", New York, Wiley & Sons, 1992.

[104] R. Gallager, *"Information Theory and Reliable Communication"*, Wiley & Sons, Inc., 1968.

[105] J. G. Proakis, "*Digital Communications*", 4th Edition, McGraw-Hill, New York, 2001.